

IMAGING THE VOLTAGE OF NEURONS DISTRIBUTED ACROSS ENTIRE
BRAINS OF LARVAL ZEBRAFISH

by

Zeguan Wang

B.Sc., University of Science and Technology of China (2018)
S.M., Massachusetts Institute of Technology (2020)

Submitted to the Program in Media Arts and Sciences, School of Architecture and
Planning, in partial fulfillment of the requirements for the degree of

Doctor of Philosophy

at the
Massachusetts Institute of Technology
May 2024

© 2024 Zeguan Wang. All rights reserved

*The author hereby grants to MIT a nonexclusive, worldwide, irrevocable, royalty-free
license to exercise any and all rights under copyright, including to reproduce, preserve,
distribute and publicly display copies of the thesis, or release the thesis under an open-
access license.*

Authored by: Zeguan Wang
Program in Media Arts and Sciences
May 17, 2024

Certified by: Edward S. Boyden
Y. Eva Tan Professor in Neurotechnology at MIT

Accepted by: Joseph Paradiso
Academic Head, Program in Media Arts and Sciences

IMAGING THE VOLTAGE OF NEURONS DISTRIBUTED ACROSS ENTIRE
BRAINS OF LARVAL ZEBRAFISH

by

Zeguan Wang

Submitted to the Program in Media Arts and Sciences, School of Architecture and Planning, on May 17, 2024 in partial fulfillment of the requirements for the degree of

Doctor of Philosophy

Abstract:

Neurons interact in networks distributed throughout the brain. Although much effort has focused on whole-brain calcium imaging, recent advances in genetically encoded voltage indicators (GEVIs) raise the possibility of imaging voltage of neurons distributed across brains. However, due to the high imaging speed and signal-to-noise ratio requirements of GEVIs, microscopy hardware to date has only been able to image the voltage of neurons within subregions of the brain, even for small animals like the larval zebrafish. To address this challenge, this thesis presents a high-speed remote scanning light-sheet microscope capable of imaging GEVI-expressing neurons distributed throughout entire brains of larval zebrafish at a volumetric rate of 200.8 Hz. The microscope combines remote refocusing and an ultrafast dual-camera system to significantly enhance the scanning and acquisition speed of light-sheet microscopy. Using this microscope, we measured voltage of $\sim 1/3$ of the neurons of the larval zebrafish brain, distributed throughout. We observed that neurons firing at different times during a sequence were located at different brain locations, for sequences elicited by a visual stimulus, which mapped onto locations throughout the optic tectum, as well as during stimulus-independent bursts, which mapped onto locations in the cerebellum and medulla. Whole-brain voltage imaging may open up frontiers in the fundamental operation of neural systems.

Thesis advisor:

Edward S. Boyden

Y. Eva Tan Professor in Neurotechnology at MIT

IMAGING THE VOLTAGE OF NEURONS DISTRIBUTED ACROSS ENTIRE
BRAINS OF LARVAL ZEBRAFISH

by

Zeguan Wang

This thesis has been reviewed and approved by the following committee members.

Edward S. Boyden

Y. Eva Tan Professor in Neurotechnology
Massachusetts Institute of Technology

Peter So

Professor of Mechanical Engineering and Biological Engineering
Massachusetts Institute of Technology

Florian Engert

Professor of Molecular and Cellular Biology
Harvard University

Table of Contents

Acknowledgments	8
List of Figures.....	10
Chapter 1 Introduction.....	12
1.1 Whole-brain voltage recording: a long-sought goal in systems neuroscience	12
1.2 Imaging neural voltage using genetically encoded voltage indicators (GEVIs).....	13
1.3 Populational imaging of neural voltage in live animal brains	14
1.4 Challenges to achieve whole-brain voltage imaging	16
Chapter 2 Conceptualization, design, and implementation of remote scanning light-sheet microscopy for whole-brain voltage imaging	21
2.1 Introduction.....	21
2.2 Enhancing the scanning speed of light-sheet microscopy	25
2.3 Enhancing the image acquisition rate of light-sheet microscopy	33
2.4 Implementation and control of the microscope	37
2.5 Characterization of the microscope's resolution.....	43
Chapter 3 Development of genetically encoded voltage indicator (GEVI) transgenic zebrafish lines	48
3.1 Testing different GEVIs in cultured neurons and larval zebrafish brains	48
3.2 Construction of transgenic GEVI zebrafish lines	50
Chapter 4 Imaging the voltage of neurons distributed throughout entire larval zebrafish brains.....	57

4.1 Imaging the spontaneous voltage activity in the larval zebrafish brain.....	57
4.2 Imaging the voltage activity in the larval zebrafish brain during visual stimulation	65
4.3 Image processing and neuron segmentation	67
4.4 Analysis of the neural activity.....	75
Chapter 5 Discussion and future work	88
5.1 Conclusion and discussions	88
5.2 Future work.....	91
Chapter 6 Other works and attempts	95
6.1 Miniaturized extended field-of-view light-field microscopy for 3-D imaging of freely behaving mouse brains	95
6.2 Enhancing the FRET efficiency of fluorescent activity indicators using spatial clustering.....	97
References	101

Acknowledgments

First and foremost, I would like to thank my advisor Professor Ed Boyden for his unreserved support and guidance throughout my entire PhD journey. Ed is not only a pioneering leader and thinker in science but also a dedicated and insightful advisor and mentor. Among the numerous things he taught me, I have learned to think like a real scientist, to focus on truly important questions, to minimize project risks through strategical planning, and to develop creative solutions by thinking bravely and broadly. I feel deeply grateful for Ed’s encouragement to think “big” as a PhD student when I first joined the group. This guidance inspired me to pursue the challenging yet rewarding path of whole-brain voltage imaging and finally to cross a key threshold towards this long-sought goal.

I would like to express my sincere gratitude to Jie Zhang, who has been collaborating closely with me on conceptualization, designing, and implementation of the whole-brain voltage imaging project. His contributions and expertise have been indispensable in bringing this project to fruition.

I am particularly grateful to my thesis committee members, Professor Peter So and Professor Florian Engert for their kind and insightful advice and valuable feedback on my thesis project. I would also like to thank Professor Matt Wilson for co-supervising this project and providing constructive suggestions on improving this project.

I extend my gratitude to Panos Symvoulidis for contributing many creative ideas to this project and for his assistance in processing and analyzing the raw images we acquired. Additionally, I would like to express my appreciation to Wei Guo, Caroline Zhang, Davy Deng, Yong Qian, Ruihan Zhang, Burcu Guner-Ataman, Adam Amsterdam, Demian Park, Seungjae Han, Minho Eom, and Young-Gyu Yoon for their contributions and generous support throughout this project.

Throughout my PhD journey, I was fortunate to work with and learn from past and present members of the Boyden lab, whether directly or indirectly. Specifically, I wish to express my gratitude to Corban Swain, Deblina Sarkar, Tay Shin, Nava Shmoel David,

Changyang Linghu, Konstantinos Kagias, Yixi Liu, Yangning Lu, Michael Skuhersky, Aimei Yang, Kiryl Piatkevich, Ho-Jun Suk, Peilun Dai, Guang Xu, Doug Weston, Lisa Lieberson, Macey Lavoie, Fira Zainal, and Ally Bassile-McCarthy for their kind help on my research and daily life in the lab.

I would like to thank the Alana Fellowship, which has generously supported me during my PhD.

I am sincerely grateful to Young-Gyu Yoon and Nikita Pak for their mentorship and help when I first joined this lab.

I would like to thank Professor Quan Wen and Dr. Kai Wang, my undergraduate research advisors, for their mentorship and guidance.

I would like to express my deepest gratitude to my parents, Qingpeng Li and Chunhe Wang, for their unconditional love and boundless support. Without their understanding and belief in me, this achievement would not have been possible.

Finally, my heartfelt appreciation goes to my beloved wife, Shuo Guo, for her endless love, steadfast support, and unwavering encouragement. Her companionship and faith in me have been the pillars of strength and serenity that enabled me to fulfill this endeavor.

List of Figures

Figure 1-1. Illustration of the volume rate and spatial resolution of different techniques assuming they are applied to imaging the whole larval zebrafish brain	17
Figure 2-1. Remote-scanning light-sheet microscopy optimized for voltage imaging of neurons distributed across the entire larval zebrafish brain.	26
Figure 2-2. Calibration and adjustment of the remote piezo scanner's movement.	29
Figure 2-3. Illustration of the synchronization of focal plane scanning (orange curve) and flashed light-sheet illumination (green lines).....	31
Figure 2-4. Simulation of system imaging quality across a 900- μm diameter, 200- μm height cylindrical field-of-view.	33
Figure 2-5. Overview of the ultrafast camera system.	35
Figure 2-6. Customized high-speed camera system.	36
Figure 2-7. The light path for light-sheet illumination and measurement of the light sheet profile.	41
Figure 2-8. Characterization of system point spread functions (PSFs) over the entire imaging field-of-view.....	45
Figure 3-1. Comparison of Positron2-Kv and Voltron2-Kv indicators in zebrafish using transient gene expression.	50
Figure 3-2. Confocal microscopy images of a transgenic Positron2-Kv _{JF525} fish brain at 5 days post fertilization (dpf).	53
Figure 3-3. Illustration of a mounted larval zebrafish for light-sheet imaging.	55
Figure 4-1. Whole-brain voltage imaging at cellular resolutions.	59
Figure 4-2. Quantifying the eye shadowed regions and the blurred regions as percentages of the imaged whole brain.....	61
Figure 4-3. Example pulse-like artifacts on the temporal traces of regions-of-interest (ROIs) affected by the stripe artifacts cast by small moving objects in light-sheet imaging.....	63
Figure 4-4. Imaging the spontaneous voltage activity of neurons distributed across an entire brain.	64
Figure 4-5. Imaging the activity of neurons distributed throughout entire zebrafish brains during visual stimulation.....	66

Figure 4-6. Temporal traces and spatial distributions of all ROI clusters grouped using UMAP and DBSCAN for identification and removal of the ROIs contaminated by stripe artifacts.....	73
Figure 4-7. 2D UMAP visualizations of ROIs before and after the removal of artifact-contaminated ROIs.....	74
Figure 4-8. The activity of neurons distributed throughout entire zebrafish brains during visual stimulation.	76
Figure 4-9. Photoswitching effects in VolPy-extracted temporal traces, and raw temporal traces, of neurons in Group 1 (i.e., neurons that have increased activity in response to the onset of the light stimulus) and neurons not in Group 1.	79
Figure 4-10. Neurons firing at different times in stimulus-evoked sequences.	80
Figure 4-11. Spatial mapping of neurons firing at different times in stimulus-evoked sequences.....	82
Figure 4-12. Different times of burst sequence activity across the zebrafish brain.....	83
Figure 4-13. Spatial mapping of the timing of burst sequence activity across the zebrafish brain.....	85
Figure 5-1. Comparison of this work and existing <i>in vivo</i> imaging techniques in terms of number of neurons and recording speed onto a 2D space (number of imaged neurons vs. sampling rate).	89
Figure 6-1. MiniXLFM for <i>in vivo</i> neural activity imaging in unrestrained, freely behaving mice.	97
Figure 6-2. Improving the sensitivity and SNR of FRET-based GEVIs through clustering.	100

Chapter 1

Introduction

1.1 Whole-brain voltage recording: a long-sought goal in systems neuroscience

Neuronal membrane voltage activity, characterized by rapid fluctuations in the transmembrane potential at millisecond speeds and amplitude changes of tens of millivolts, is fundamental to the generation of animal behaviors and intelligence. First, neurons use voltage activity to encode and process information, such as the sensory input from visual¹, olfactory², auditory³, and somatosensory⁴ stimulus. In addition, neurons communicate through voltage activity propagation along neuronal processes (also referred to as neurites), such as dendrites and axons, plus chemical neurotransmitter diffusion on synapses. Furthermore, the brain uses voltage activity to control muscle contraction and motion behaviors of animals. Comprehensive understanding of the brain requires recording of the voltage activity of neurons in live brains.

Neurons interact in circuits distributed throughout entire animal brains. A simple behavior can involve neurons in many brain regions. For example, imagine a larval zebrafish makes a sudden “J” turn⁵ to escape from a predator appearing in its visual field. At a simplest scenario, the visual stimulus, or the predator image in this case, must first activate the fish’s photoreceptor cells on its retina, which convert light into membrane

voltage signals and send the information to the optic tectum at the midbrain through relays of other cells. Then this information is processed and sent to the hindbrain and spinal cord to initiate fast and intense movement of its body and tail. In reality, more brain regions might be involved. Investigating the mechanisms of neural circuits for such a behavior will need simultaneously monitoring the activity of neurons distributed across the entire brain.

Recording the voltage activity of all the neurons in entire live animal brains holds unprecedented promises to advance neuroscience research. The whole-brain cellular neural voltage dynamics will allow neuroscientists to investigate the brain and neural basis of animal behaviors at the single spike (action potential) and subthreshold potential level without the risk of missing any neurons that are involved in the neural operations. Such datasets can help neuroscientists to study neural coding, map functional connectivity, infer neural circuit causality, and build computational models of whole brains. Importantly, with pan-neuronal coverage, single-cell resolution, and much superior temporal resolution, whole-brain voltage recording will provide datasets that have never been obtained before, opening new frontiers for new discoveries. As a result of all these promising potentials, whole-brain voltage recording has long been a major technical goal in neuroscience. However, due to a few technical gaps, before this work no one had achieved whole-brain voltage recording, even in small animals such as larval zebrafish.

1.2 Imaging neural voltage using genetically encoded voltage indicators (GEVIs)

Electronic probes have long been used as standard tools to record neuron membrane voltage in neuroscience. Cellular voltage dynamics has been successfully acquired using single or multiple-unit electrodes, micro-electrode arrays, patch clamps, and soft mesh electrodes⁶. But these techniques require insertion or implanting of electronics into the sample, which constraints their scalability *in vivo*. It is not feasible to simultaneously probe

every individual neuron in a live animal brain using these electronic devices, while maintaining the brain's natural state.

The recent advances in genetically encoded voltage indicators (GEVIs) raise the possibility of non-invasively monitoring the voltage of large populations of neurons⁷. Genetically encoded voltage indicators (GEVIs) are transmembrane proteins that can sense the membrane voltage and change their fluorescence properties, such as intensity and lifetime. These fluorescence changes are imaged using microscopes as indications of the membrane voltage. GEVIs can be genetically targeted in specific types of neurons or expressed pan-neuronally. Some GEVIs⁸ require additional chemical dye molecules (e.g., Janelia Fluor Dyes⁹) that covalently bind on the indicators, which is referred to as “chemigenetic indicators”. Chemigenetic GEVIs possess the good properties of chemical dyes: bright and photostable. Examples of chemigenetic GEVIs include Voltron2 and Positron2¹⁰. Voltron2 and Positron2 contain a voltage-sensitive opsin-based quencher motif and a HaloTag motif that binds to a chemical dye molecule. The two motifs form a Förster resonance energy transfer (FRET) pair so that the voltage changes detected by the dim opsin quencher can be transferred to and reported by the bright dye fluorophore. Voltron2 and Positrons can decrease and increase their intensity by approximately 20% in response to an action potential, respectively. In addition to chemigenetic GEVIs, there are voltage sensing domain-based indicators such as ASAP3¹¹, single opsin indicators such as QuasAr6¹² and Archon1¹³, and opsin-FRET protein indicators such as Ace-mNeon2 and pAce¹⁴. Coupled with optical microscopy techniques, GEVIs have enabled *in vivo* imaging of the cellular neural voltage in worms (*C. elegans*)¹⁵, fruit flies (*Drosophila*)⁸, larval zebrafish (*Danio rerio*)⁸, and mice^{8,11,14,16,17}. Although existing microscopy hardware can only allow imaging within subregions of the brain, the voltage activity of populational neurons has already shed light on some basic mechanisms of the brain.

1.3 Populational imaging of neural voltage in live animal brains

Coupled with GEVIs, high-speed microscopy techniques, including many new setups that were specifically designed for voltage imaging, have been used to image the voltage activity of many neurons in live animal brains. In larval zebrafish, conventional light-sheet microscopy can image dozens of neurons within a $100\mu\text{m} \times 70\mu\text{m}$ region on a single plane at 300 Hz and allow correlation between their voltage activity with the fish's fictive behaviors⁸. By employing a thin stripe-shaped camera field-of-view (C-FOV, defined as the number of row and column pixels captured in one frame), more than 10 neurons at a single plane of the larval zebrafish spinal cord were imaged at 1000 Hz¹⁸. Such experiments have helped identify a new subpopulation of tonic-spiking ventral V3 neurons in larval zebrafish. Recently, by utilizing a retroreflector for light-efficient remote refocusing and an advanced camera for fast image acquisition, more than 100 neurons from 8 planes of the larval zebrafish spinal cord were imaged at 500 Hz¹⁹.

In mouse brains, populations of neurons located in the cerebral cortex, hippocampus, and striatum have been imaged at several hundred hertz to over one kilohertz, using widefield, confocal, and two-photon microscopy methods^{8,11,14,16,17,20–25}. Using widefield imaging, the voltage activity of dozens of neurons within a $\sim 250\mu\text{m} \times 900\mu\text{m}$ two-dimensional (2D) region in the mouse cerebral cortex and hippocampus was recorded at 400 Hz to 600 Hz, while the animals were behaving^{8,14}. By developing a multiplane confocal microscope, neurons within four $150\mu\text{m} \times 150\mu\text{m}$ planes at different depths in live mouse brains can be simultaneously imaged at 916 Hz²². New high-speed two-photon microscopes have also been invented and applied for *in vivo* voltage imaging in mice, which allows for imaging a $50\mu\text{m} \times 250\mu\text{m}$ 2D region at 1000 Hz²⁰ or a $400\mu\text{m} \times 400\mu\text{m}$ 2D region at 1000 Hz²¹ in a more recent work. One difficulty for *in vivo* voltage imaging in mouse brains comes from the brain's highly scattering nature. Light scattering diminishes signal-to-noise ratios and limits imaging penetration depth. As a result, imaging deep brain regions (e.g., hippocampus) will require implanted optics or removing part of the brain, making optically accessing all the regions in an intact live mouse brain implausible.

To summarize, despite that much progress has been made in populational imaging of neural voltage in live animal brains, existing microscopy hardware can only image up to hundreds of neurons residing in a small region of the brain. The imaged neurons only account for a tiny fraction (~0.1% for larval zebrafish, ~0.0001% for mice) of all the neurons in the nervous system. Optically imaging the neural voltage of the entire mouse brain is fundamentally difficult due to tissue scattering. In contrast, the transparency and the small size of the larval zebrafish brain raise the possibility to image the neural voltage in entire animal brains. However, achieving this goal requires new microscopy hardware with much improved overall imaging capabilities, including speed, field-of-view, resolution, and signal-to-noise ratio.

1.4 Challenges to achieve whole-brain voltage imaging

Whole-brain voltage imaging faces challenges from multiple aspects. First, voltage imaging suffers from intrinsically low signal-to-noise ratios, due to its required high imaging rates and membrane localization of GEVIs. Voltage imaging usually requires several hundred hertz temporal sampling rates to resolve action potential spikes, allowing for only millisecond scale exposure time for each time point (each imaging frame). During such a short period, GEVIs can only emit a limited number of photons. Besides, GEVIs are located on neuron membranes, which are two-dimensional surfaces that already accommodate dense endogenous membrane proteins. Excessive expression of GEVIs on neuron membrane can also alter the physiological properties of the membrane²⁶. As a result, the number of GEVI molecules each neuron can host is limited, which further constrains the number of emission photons for detection. Consequently, the shot noise in voltage imaging can easily overwhelm real activity signals.

Second, scaling up the field-of-view of voltage imaging to the entire brain, even for small animals like larval zebrafish, poses additional technical challenges. To image GEVI-expressing neurons distributed across entire brains, a new microscope that simultaneously meets all the technical requirements is needed. To be specific, the new microscope must achieve temporal resolution comparable with millisecond-scale action potential timing, while having a three-dimensional field-of-view (3D-FOV, defined as the 3D volume that a microscope can cover) sufficient to cover the whole larval zebrafish brain, together with high enough spatial resolution to resolve single cells, and high enough signal fidelity to detect individual action potentials. These requirements, when combined, are beyond the capabilities of existing microscopes. To better illustrate the spatiotemporal resolution gap, here existing volumetric imaging methods are plotted in a 2-D coordinate system based on their volume rate (x-axis) and spatial resolution (y-axis) when image the whole larval zebrafish brain (**Fig. 1-1**). Although many techniques are developed for volumetric neural imaging, their overall spatiotemporal resolutions are still far away from what are required (**Fig. 1-1 “goal” region**) for achieving whole-brain voltage imaging in larval zebrafish.

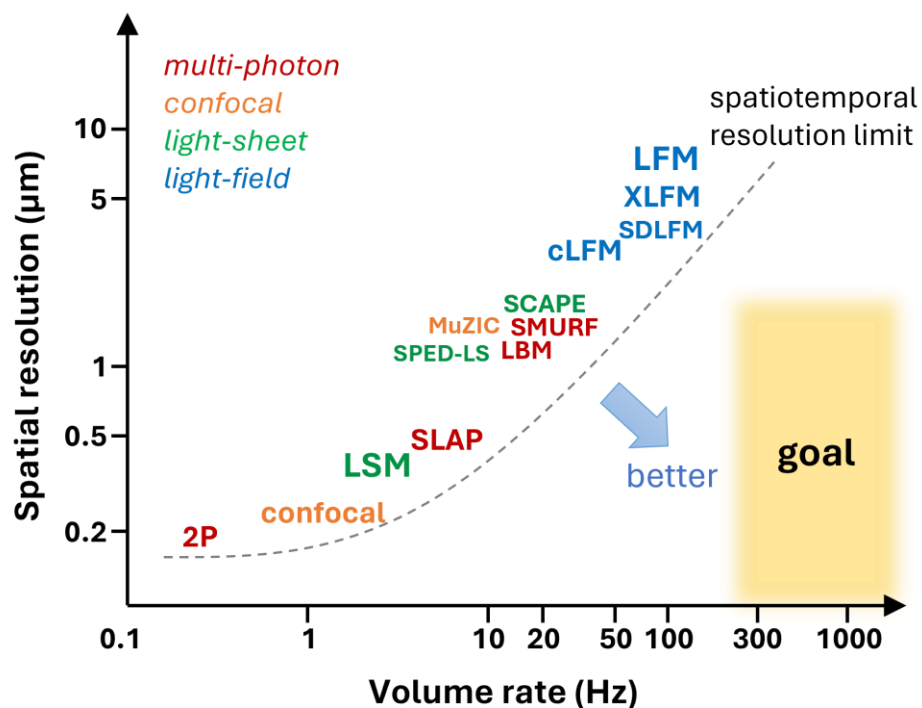


Figure 1-1. Illustration of the volume rate and spatial resolution of different techniques assuming they are applied to imaging the whole larval zebrafish brain. The “goal” region indicates a rough estimate of the spatiotemporal resolution required for whole-brain voltage imaging in larval zebrafish. Techniques are classified into different categories marked in different colors. 2P: two-photon microscopy; confocal: spinning disk confocal microscopy; LSM: conventional light-sheet microscopy²⁷; SLAP: scanned line angular projection microscopy²⁸; SPED-LS: spherical-aberration-assisted extended depth-of-field light sheet microscopy²⁹; LBM: light-beads microscopy³⁰; MuZIC: multi-Z imaging with confocal detection²²; SMURF: spatiotemporal multiplexed ultrafast resonance frame-scanning²¹; SCAPE: swept, confocally aligned planar excitation³¹; cLFM: confocal light-field microscopy³²; SDLFM: sparse decomposition light-field microscopy³³; XLFM: extended field-of-view light-field microscopy³⁴; LFM: light-field microscopy³⁵;

Moreover, imaging across a volume can further exacerbate the low signal-to-noise ratio (SNR) problem by reducing the exposure time of each neuron for each time point. This is because modern microscopes usually image a 3-dimensional (3D) volume by sequentially illuminating and scanning different parts of the volume (e.g., point by point scanning in two-photon microscopy, line by line or plane by plane scanning in light-sheet microscopy), each neuron within a brain volume is only excited for a fraction of the whole period of each time point. This is in contrast with single-plane voltage imaging, where each neuron can be continuously excited and imaged. Although scanless volumetric imaging methods such as light-field microscopy^{33–36} exist, in these methods fluorescent signals from different parts of the volume are usually mixed in the raw images, which increases the background shot noise for each neuron.

Third, photobleaching and phototoxicity, although not hard constraints that prevent the achievement of whole-brain voltage imaging, can be problematic in many practical experiments. In order to enhance the image brightness and suppress the shot noise in voltage imaging, usually high-intensity excitation is applied to the sample, which ranges from 10 mW/mm² to 12 W/mm²¹⁷. This is more than one order of magnitude higher than the typical light intensity used for calcium imaging²⁷. Under such high-intensity illumination, GEVIs can quickly bleach, precluding hours-long recording to study slowly varying properties of neural circuits. The high power can also cause phototoxicity and

accumulate heat to damage the brain tissue. Alleviating these problems will need brighter and more photostable GEVIs and more light-efficient imaging hardware.

Chapter 2

Conceptualization, design, and implementation of remote scanning light-sheet microscopy for whole-brain voltage imaging

2.1 Introduction

Genetically encoded voltage indicators (GEVIs) offer the promise of imaging neural voltage from many neurons in parallel. Yet, simultaneously meeting all the technical requirements for imaging GEVI-expressing neurons distributed across entire brains is challenging. The microscope must achieve temporal resolution comparable with millisecond-scale action potential timing, while having a three-dimensional field-of-view (3D-FOV, defined as the 3D volume that a microscope can cover) sufficient to cover the whole larval zebrafish brain, together with high enough spatial resolution to resolve single cells, and high enough signal fidelity to detect individual action potentials. Optimizing for one goal often degrades the microscope's performance in another. We here ask whether a microscope can be designed to cross the threshold of imaging voltage of neurons distributed across an entire zebrafish brain by satisfying all these criteria simultaneously.

Light-field microscopy (LFM) is a fast volumetric imaging technique, as it captures 3D information of a sample by taking a single 2D camera snapshot^{32,33,35–37}. Different LFM configurations have been developed and applied to imaging the neuronal calcium activity

in worms^{35,38}, fruit flies^{33,39}, larval zebrafish^{32,33,35,37}, and mice^{32,40–42}. In these works, the calcium activity of 3D distributed neurons was monitored at a rate up to the maximum camera frame rate (e.g., 100 Hz), offering high temporal resolution. Specifically, by taking advantage of the spatiotemporal sparsity of calcium activity, LFM has allowed simultaneous imaging of the entire larval zebrafish brain at near single-cell resolution³³. Recently, with the advancement in GEVI development, LFM has been used for volumetric voltage imaging, where a single neuron in an acute mouse brain slice⁴³ and sparse neurons in fruit fly brains⁴⁴ were captured at 100 Hz and 500 Hz, respectively.

Despite its high imaging speed, LFM possesses inherent limitations in spatial resolution and signal-to-noise ratios, especially in densely labeled samples³³. LFM recovers 3D information by acquiring both the locational and angular information of light rays from the sample. Existing LFM configurations use microlens arrays to sample either the image plane or the Fourier pupil plane, trading locational information for angular information. The principles of LFM cause a fundamental trade-off between the technique's resolution and axial field-of-view. To image a 200- μm thick larval zebrafish brain, it is difficult to achieve a spatial resolution beyond $\sim 3 \mu\text{m}$ without scanning the brain in multiple snapshots. Given a $\sim 6.6 \mu\text{m}$ average neuron soma diameter²⁷ in larval zebrafish, the 3- μm resolution might be sufficient to separate neighboring neuron nuclei, e.g., in the case of whole-brain calcium imaging using nuclear-targeted calcium indicators³³. However, GEVIs specifically label cell membranes, rendering “ring” shaped neurons where only their boundaries are visible. Separating closely packed neurons with GEVI labeling will require a resolution that allows resolving the “ring” structures of neurons. This resolution requirement exceeds the capabilities of single-snapshot LFM. In addition to the resolution, another limitation that LFM faces when imaging densely labeled samples is decreased signal-to-noise ratios. Dense labeling reduces the signal-to-noise ratios of LFM in two ways. First, in LFM, signals in a 3D volume are mixed and recorded on a 2D raw image. Reconstructing the 3D information requires demixing the signals in the raw image. Dense labeling increases the amount of signals that are mixed on raw light-field images, therefore complicating the signal demixing process and deteriorating the reconstruction accuracy. Second, in LFM, fluorescence from all different planes of the sample is mixed and acquired together, resulting in a significant increased background for the signals of interest (e.g.,

fluorescence changes of a neuron). The bright background causes increased shot noise, which cannot be removed by reconstruction. Specifically, when imaging densely labeled zebrafish brain that contains ~35 layers of neurons, the shot noise of a neuron can be ~6× higher for LFM than using optical sectioning techniques such as confocal microscopy and light-sheet microscopy.

Although these limitations hinder LFM's potential for imaging the voltage activity of densely labeled neurons in thick volumes (e.g., the entire larval zebrafish brain), LFM holds unique promise to image neural voltage in thin brain regions and in sparsely labeled brain volumes. LFM has been used for *in vivo* voltage imaging of sparse neurons in adult fruit flies at 500 Hz⁴⁴.

Light-sheet microscopy (LSM) is a promising technique for volumetric fluorescent imaging, as it specifically excites and efficiently images fluorophores in a two-dimensional (2D) focal plane, thus offering high throughput, good optical sectioning capability and low phototoxicity, while maintaining good spatial resolution (i.e., down to 0.3 μm, lateral)^{45–48}. Using conventional LSM, whole-brain, cellular-resolution calcium imaging has been achieved in larval zebrafish at a volumetric imaging rate of 0.8–3 Hz^{27,49}. However, it is difficult to improve the speed of conventional LSM to a volume rate that can be used for voltage imaging, while maintaining the 3D-FOV required to image a whole larval zebrafish brain (~900×370×200 μm³) at cellular resolution^{45,47,48}. This difficulty arises from two factors: (1) it is challenging to enhance the scanning speed of the image plane, and (2) cameras exhibit limited frame rates at the necessary camera field of view (C-FOV, defined as the number of row and column pixels captured in one frame)^{45,48}. Regarding the first constraint: in conventional LSM, a 3D sample is scanned plane by plane through physical translation of the detection objective. But such strategies are difficult to adapt for scanning thick biological samples (e.g., >200 μm) at high volume rates (e.g., >100Hz). This is due to the scanning range and speed limitations of scanners designed for moving objective lenses. The fastest commercial objective scanner (PI P-726) can run at 560 Hz, but it can only scan across a 100-μm range⁵⁰. Other objective scanners can scan across a longer range (up to several mm), but not at a frequency >100 Hz⁵¹. Regarding the second constraint: the speed of LSM is limited by the camera's acquisition rate. The volume rate of LSM can be calculated as the camera frame rate divided by the number of 2D image planes of the

volume. Current state-of-the-art cameras (e.g., Hamamatsu ORCA Flash, Andor Zyla) have full-speed pixel rates of $\sim 0.5 \times 10^9$ pixels per second. When imaging a large 3D-FOV, e.g., the whole larval zebrafish brain, such cameras can provide a frame rate up to 400 Hz (assuming a 512×1280 -pixel C-FOV), which translates to a maximum volume rate of only 10-15 Hz.

Many strategies have been proposed to enhance the scanning speed of LSM⁵²⁻⁶². One is remote refocusing^{52,53}, which rapidly shifts the system's focal plane at a remote site using a tunable lens⁵⁴, translational tertiary objective lens⁶³, or translational mirror^{55,56}. However, the additional aberration from tunable lenses limits the system's numerical aperture (NA) and two-dimensional field-of-view (2D-FOV, defined as the area a microscope can image in a single two-dimensional focal plane). The numerical aperture of reported tunable lens-based LSM systems is limited to 0.3 NA for a 600- μm diameter circular ($\Phi 600 \mu\text{m}^2$) 2D-FOV⁵⁴. On the other hand, spherical aberration from refocusing can be eliminated using a translational tertiary objective lens⁶³ or a translational mirror^{52,53} at a remote site. However, scanning the tertiary objective lens has the same scanning range and speed limitations as encountered in conventional LSM; regarding the remote mirror strategy, previous studies used commercial mirrors that are several grams in weight and actuators that are designed for heavier loads (such as objective lenses), and thus achieved <100-Hz scanning rates and <100- μm scanning range^{55,56}. In addition, reported lateral 2D-FOVs in remote mirror-based LSM configurations were $<\Phi 200 \mu\text{m}^2$, perhaps due to high magnification ratios and system aberrations^{55,56}.

Besides remote refocusing, a recently developed technique, termed SCAPE^{31,64} or oblique plane microscopy (OPM)⁵⁷⁻⁶², can also relieve the scan rate bottleneck of LSM. SCAPE and OPM laterally sweep an oblique-aligned focal plane using remote galvo or polygon mirror scanners, allowing volume scan rates up to the maximum scan rates of these mirror scanners. SCAPE 2.0³¹ can scan a $197 \times 293 \times 78 \mu\text{m}^3$ volume at a high rate of 321 volumes per second (VPS), or a $345 \times 278 \times 155 \mu\text{m}^3$ volume at 100 VPS. But, the oblique alignment between the secondary and the tertiary objectives has limited the effective NA to 0.35, which means far ($\sim 10\times$) less light collection than, say, a 1.0 NA lens. This makes whole-brain voltage imaging challenging, given that voltage imaging is far lower in signal-to-noise ratios (SNR) than calcium imaging (indeed, as will be seen in this paper, a $10\times$

reduction in light collection for the currently proposed microscope would bring SNR for many neurons below acceptable levels). To increase effective NA, several new OPM configurations were proposed recently, where water chambers⁵⁷ and customized objectives^{58,59} were used to reduce the misalignment angle between the light cones of the secondary and the tertiary objectives. These strategies have enhanced effective NAs up to the NAs of the detection objectives (e.g., NA = 1). While these OPMs possess high NA and the potential to scan volumes at high speeds, the light refraction on the secondary objective's oblique image plane and the oblique tertiary objectives causes extra aberrations that reduce the diffraction limited 2D-FOV. Recently, a specifically designed, glass-tipped tertiary objective lens⁵⁸ enabled an $800 \times 420 \mu\text{m}^2$ 2D-FOV at NA=0.97 in OPM. However, this glass-tipped objective lens still causes aberrations at the edges of large 2D-FOV's (e.g., $>500 \mu\text{m}$), as only the center $\Phi 450 \mu\text{m}^2$ of its 2D-FOV is optimized for diffraction limited resolution⁶⁵. In practice, diffraction limited resolution might not be required to resolve single neurons, give the neuron somas (e.g., $\sim 6 \mu\text{m}$ in zebrafish) are typically more than ten times larger than the diffractive limited point spread function formed by a high-NA objective lens (e.g., NA =1).

2.2 Enhancing the scanning speed of light-sheet microscopy

We optimized the translational mirror-based remote refocusing strategy^{52,53,55,56} to enhance the volume scan rate of light-sheet microscopy (Fig. 2-1). Different from previous work, we customized a lightweight silver-coated mirror that is only 0.01 g in weight, and scanned it using a piezo bender actuator that has a large travel distance (270 μm), high resonant frequency (930 Hz), and sub-millisecond response time. The lightweight mirror and fast piezo actuator allowed us to scan a 200- μm axial (z-axis) range at the sample at up to 300-Hz.

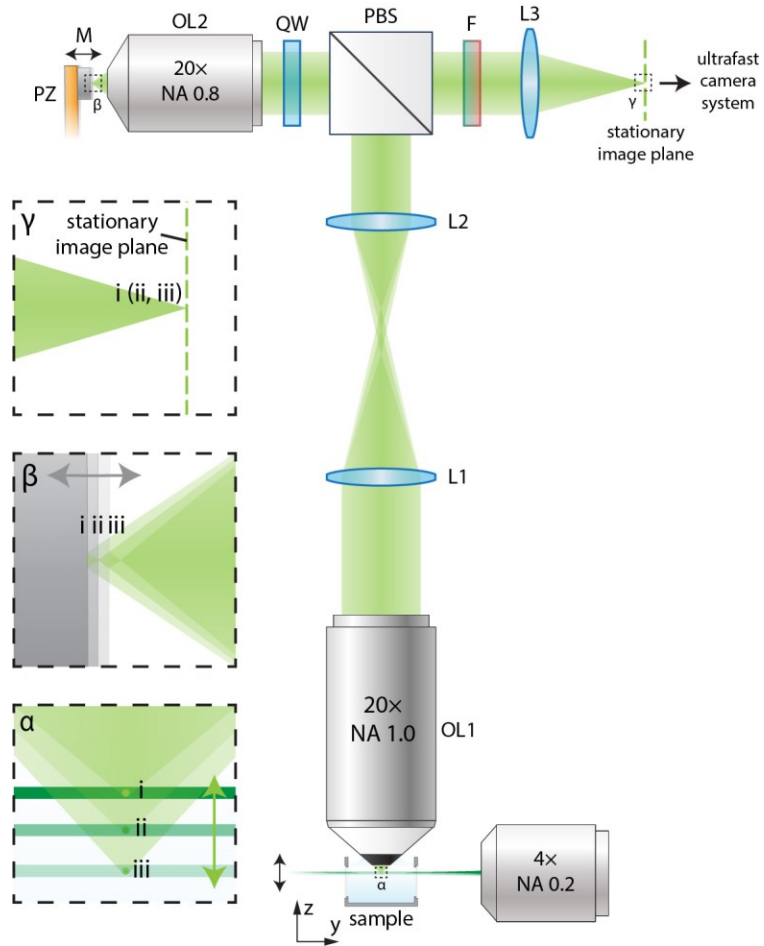


Figure 2-1. Remote-scanning light-sheet microscopy optimized for voltage imaging of neurons distributed across the entire larval zebrafish brain. Overview and operational principles of our whole-brain, voltage imaging-optimized, remote scanning light-sheet microscope design. At the bottom, a sample (an infinitely small fluorescent bead, for purposes of explanation in this figure) in a water chamber is illuminated from one side by a rapidly scanning light sheet from an excitation objective lens. The fluorescence excited by the light sheet is collected orthogonally through a 20 \times high numerical aperture (NA = 1.0) water-immersion objective lens (OL1). The fluorescent light passes through a 4f imaging system composed of two tube lenses (L1 and L2) before entering a polarized beam splitter (PBS). The PBS deflects fluorescence of particular polarization into a quarter wave plate (QW) and a remote objective lens (OL2, air, 20 \times , NA = 0.8). The remote objective then focuses the fluorescence into real images. These images are reflected by a mirror (M) that is translated by a piezo (PZ), and re-imaged by the remote objective. After transmitting through the quarter wave plate again, the fluorescence rotates polarization by 90 degrees. The fluorescence then passes through the polarized beam splitter and an emission filter (F), before being refracted by a tube lens (L3) into real images. The remote piezo actuator (PZ) moves the mirror in synchrony with the light sheet, ensuring images of different z planes (a, i, ii, iii) are captured at the stationary image plane. The final images are recorded by an ultrafast camera system.

at the sample remain in focus at the stationary focal plane of L3. These stationary, focused images are directed to an ultrafast camera system for recording. The green dashed line at L3's focal plane indicates a stationary image plane of the microscope. To better illustrate this imaging process, small views at the sample (dashed box α), the remote mirror (dashed box β), and the focused images at the focal plane of tube lens L3 (dashed box γ) are enlarged and shown along the left side of panel a. We show this imaging process at three different time points (i, ii, iii). The enlarged view of dashed box α shows that, at the three time points (i, ii, iii), the light sheet (green horizontal lines, different shades indicate different time points) excites an infinitely small fluorescent bead (green dots) at three different z locations, and the emitted fluorescence (green cones, only the part entering OL1 is drawn) is collected by OL1. Enlarged view of dashed box β shows that, at different time points (i, ii, iii), the remote mirror (gray, different shades indicate different time points) translates and reflects the fluorescence light (green cones) back to OL2. The mirror's translational motion is synchronized with the light sheet scanning. Enlarged view of the dashed box γ shows that the fluorescence light (green cones, overlapped here) at different time points (i, ii, iii) is focused on the same image plane (dashed green line).

To achieve high-frequency scanning of the remote mirror, we used an open-loop controlled piezo bender actuator. To address the hysteresis of the piezo, we rapidly measured the mirror's motion using a customized microscope and adjusted the piezo's control signals via LabVIEW software (**Fig. 2-2**). The mirror's motion was captured at a rate of 70000 Hz by a line camera through a 20 \times microscope (**Fig. 2-2a**). For precise measurement of the mirror's shifts, we 3D printed a tiny imaging target with fine grid patterns using two-photon polymerization and attached it to the side of the mirror. While the mirror's movement was being monitored, we adjusted the piezo's control signals, especially the amplitudes and phases of its high-order sinusoidal components, to counteract the hysteresis. By doing this, we could calibrate the mirror's movement and match it to the desired waveform. The adjustments were made until the discrepancy between the observed and the intended waveforms was less than 0.1% of the total scanning span.

For improved uniformity in camera frame intervals, we used non-sinusoidal scanning. Specifically, we added sinusoidal waves with odd-integer multiple frequencies (e.g., 602.4 Hz, 1004 Hz) to the volume scan rate (200.8 Hz). This allowed us to design a remote mirror scanning curve resembling a triangle wave up to its 3rd order Fourier transform (**Fig. 2-2c-e**). This waveform, in comparison to a basic sinusoidal one, facilitates

more even axial scanning of the sample. Our tests indicated that the piezo scanner exhibited high displacement consistency when driven by periodic voltage waveforms (with a max deviation of less than 0.5% over a minute) in an open-loop control. This ensured long-term stable scanning of the fish brain. For whole-brain imaging, we drove the piezo to scan across a 113 μm range (170 μm at the sample) at 200.8 Hz.

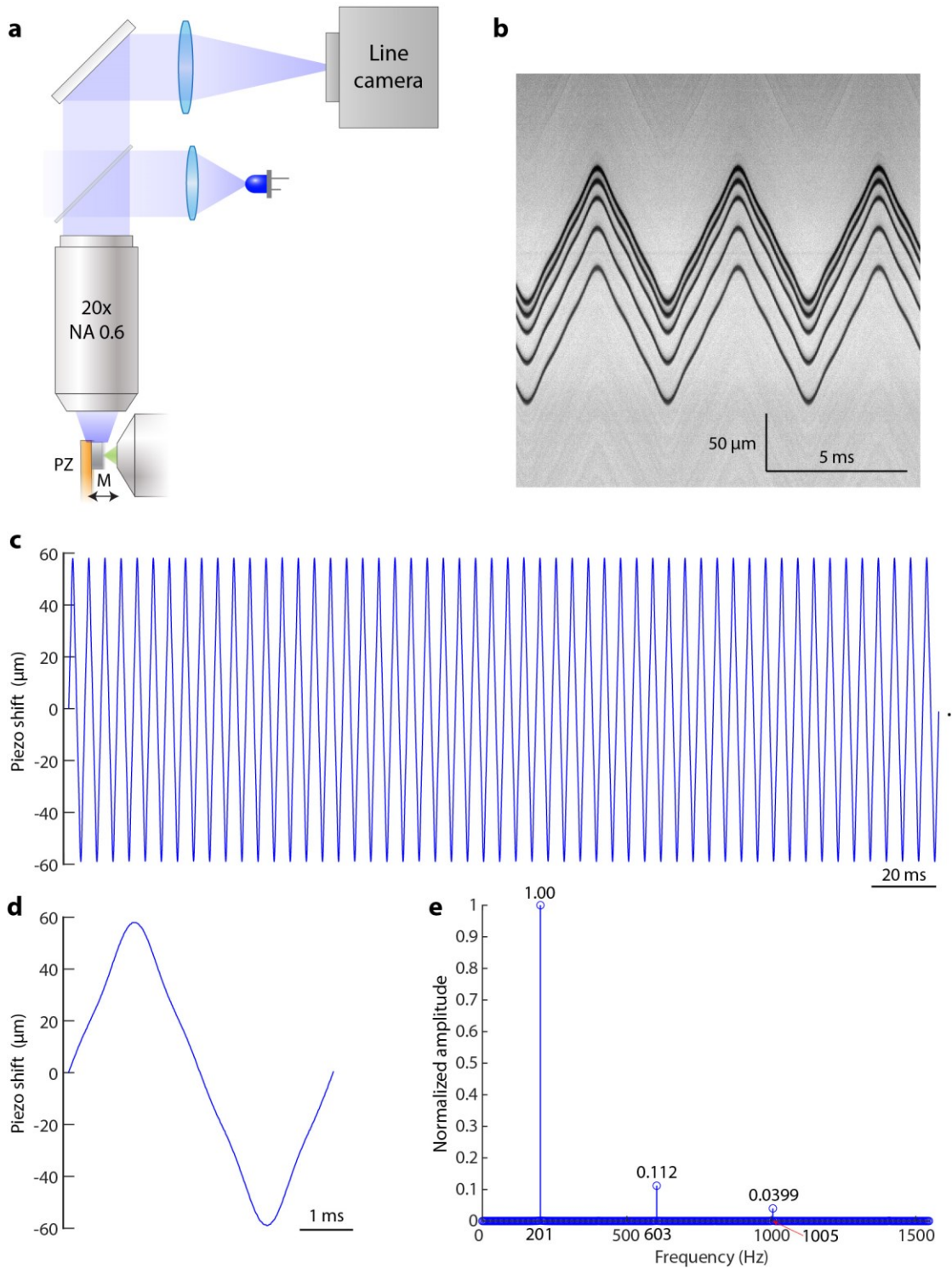


Figure 2-2. Calibration and adjustment of the remote piezo scanner's movement. **(a)** A schematic representation of the $20\times$ widefield microscope used for measuring the piezo's movement. The imaging target was imaged at 70000 Hz using a line camera. A blue LED was used for illumination. **(b)** Raw line camera images showed the piezo bender's

displacement curve over time, post-calibration. Each column represents a single camera frame. These frames were stitched side-by-side from left to right according to their temporal order. **(c)** The displacement curve over time of the piezo scanner derived from line camera videos. **(d)** An enlarged view of a scan cycle of the displacement curve shown in **(c)**. **(e)** Normalized amplitudes of the fast Fourier transform applied to the displacement curve in **(c)**. The three significant frequency components align with the first three Fourier components of a triangle waveform, which have $1\times$, $3\times$, and $5\times$ frequencies and normalized amplitudes of 1.00, 0.111, and 0.0400, respectively.

Scanning the remote mirror corresponds to scanning the microscope’s focal plane. For consistent in-focus imaging, the light sheet must remain overlapped with the scanning focal plane beneath the detection objective lens. To align the light sheet with the focal plane, we introduced a 40- μs light-sheet pulse with a specific time delay relative to each scan cycle while the remote mirror and the galvanometer were in operation. The short excitation pulses temporally “sampled” a stationary image plane on the camera. By adjusting the control signals of the galvanometer at the exact moments of the light sheet pulse, we ensured the “sampled” plane was in-focus. Repeating this process with various time delays allowed the light sheet to coincide with the focal plane throughout the whole scanning process.

Within a full scan cycle of 4980 μs , which comprising both upward and downward scans, the 30 planes of the zebrafish brain were imaged in an interleaved sequence (**Fig. 2-3**). To mitigate the blur induced by continuous axial scanning during exposure, the light sheet was pulsed for short durations ranging from 40 μs to 72 μs during an exposure of each image plane. The timings of the laser pulses were calibrated to ensure uniform sampling along the axial axis. To perform this calibration, we built a microscope at the water chamber’s contralateral side to the excitation objective and imaged the axial locations of the pulsed light sheet during volumetric scanning. The exposure of individual camera frames was synchronized with the light-sheet pulses. To ensure the exposure time comprehensively encompassed the excitation period, the camera exposure time was set to be 10 μs longer than the light sheet pulse’s duration and the relative timing of the exposure to the light sheet pulse was carefully adjusted. During a 40- μs light pulsing period, the microscope’s focal plane (and the light sheet) traveled axially across approximately 2.7

μm , about half of the thickness of the light sheet (measured to be $5.3 \pm 1.4 \mu\text{m}$, full width at half maximum, mean \pm standard deviation, across $400 \mu\text{m}$ in y-axis).

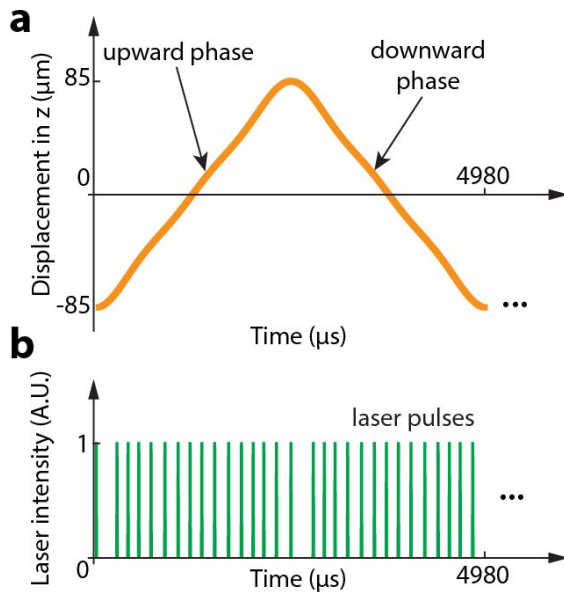


Figure 2-3. Illustration of the synchronization of focal plane scanning (orange curve) and flashed light-sheet illumination (green lines).

(a) The axial (z) displacement of the microscope's focal plane during a scan cycle (4.98 ms) is depicted as the orange curve. The scan cycle has an upward phase when the microscope's focal plane travels upwards in z, and a downward phase when the focal plane travels downwards in z.

(b) The green lines represent 40- μs light-sheet pulses for the excitation of individual axial planes of the sample. Different z planes of the sample were imaged in an interleaved manner. The timing of the light-sheet pulses was calibrated to ensure the imaged z planes were evenly spaced along the z-axis. Camera frames were recorded in synchrony with these pulses, with an exposure time 10-20 μs longer than the pulse time.

Although remote refocusing theoretically does not introduce aberration, with so many high NA optical elements in the detection path, accumulated aberrations from each optical element could reduce the effective 2D-FOV by decreasing the spatial resolution at the 2D-FOV edges, particularly along the rostral-caudal (x) axis of the zebrafish brain, which spans $\sim 900 \mu\text{m}$. To obtain a sufficient 3D-FOV with low aberration for whole-brain

cellular-resolution imaging, we used Zemax to simulate the aberrations in a $\Phi 900 \times 200 \mu\text{m}^3$ 3D-FOV of a series of configurations with various parameters and optical elements (**Fig. 2-4**). Due to the unavailability of Zemax models for the detection and the remote objective lenses, in this simulation, we only evaluated the aberrations from all the remaining optical elements in the detection path, including three tube lenses, a polarized beam splitter, and a relay lens pair. The relay lens pair was used to reduce the system magnification ratio to $\sim 6.16\times$ so that the whole zebrafish brain could fit into the C-FOV on the image sensor ($2.30 \times 5.76 \text{ mm}^2$, 512×1280 pixels). The relay pair was also used to relay the split half images onto the two cameras in the distributed planar imaging system, as described in the “**2.3 Enhancing the image acquisition rate of light-sheet microscopy**” section. According to our simulation results, we found that proper choice of tube lenses in the detection path is important to reduce system aberrations. We identified an optimal microscope configuration that achieved a diffraction-limited $900 \times 200 \mu\text{m}^3$ 3D-FOV at a high NA of 1.0, with the wavefront error at the 3D-FOV edge to be 0.15λ root mean square (at 550 nm). Although the detection and the remote objective lenses were not considered in our simulation, the identified configuration can still efficiently reduce the aberrations in our real system. This is because the aberration in an imaging system is the summation of the aberration contributed by each optical element in the system⁶⁶. In our Zemax simulation, the detection objective lens OL1 and the remote objective lens OL2 were modeled as paraxial surfaces with the same focal lengths. Although this simplification neglected the spherical aberrations from refocusing (i.e., imaging at z planes other than their focal plane), such spherical aberrations from the two objectives canceled out in our remote refocusing microscope because of magnification-refractive index matching⁵².

Because commercial tube lenses cannot fully satisfy our parameter requirements (e.g., focal plane and aperture), we borrowed the idea from previous OPM work^{58,67} and customized several tube lenses with desired parameters by assembling multiple commercially available lenses. According to our tests, these engineering efforts yielded a $\Phi 900 \times 200 \mu\text{m}^3$ three-dimensional volume with spatial resolutions that are only limited by the lateral effective pixel size (0.73 μm) and the z sampling step size (5.86 μm) (**Fig. 2-8**).

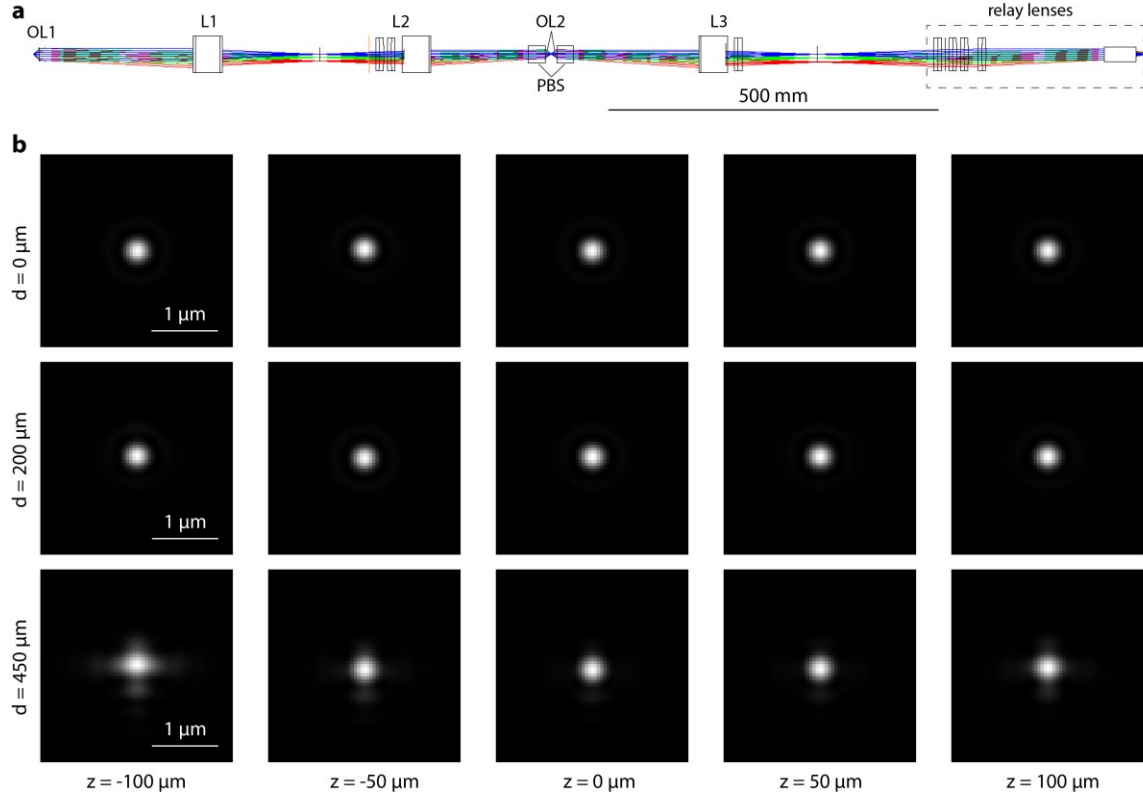


Figure 2-4. Simulation of system imaging quality across a 900- μm diameter, 200- μm height cylindrical field-of-view. (a) Layout of the imaging light path in Zemax simulation. OL1, L1, L2, OL2, PBS, L3 indicate the same parts as in Figure 2-1. **(b)** 2-dimensional (x-y) point-spread functions (PSF) at various axial positions ($z = -100 \mu\text{m}, -50 \mu\text{m}, 0 \mu\text{m}, 50 \mu\text{m}, 100 \mu\text{m}$) and different distances from the field-of-view's lateral center ($d = 0 \mu\text{m}, 200 \mu\text{m}, 450 \mu\text{m}$). The simulation was conducted with a 1.0 system NA and 550 nm wavelength.

2.3 Enhancing the image acquisition rate of light-sheet microscopy

Having established an optical design, we next turned to the camera. The spatial resolution and the volume scan rate of the LSM are determined, in part, by the camera's frame rate and C-FOV. The C-FOV should have a sufficient number of pixels (e.g., 512×1280) to sample the 2D-FOV of the entire zebrafish brain, with an effective pixel size smaller than

a neuron soma. The camera's frame rate determines the LSM's volume scan rate and z-plane step size. For instance, with a fixed camera frame rate of 6000 Hz, an LSM can scan at 300 VPS, capturing 20 z-planes per volume (200 μm thick), with a 10 μm z-sampling step size. Alternatively, at the same frame rate, the LSM can scan at 200 VPS, acquiring 30 z-planes per volume, with a 6.7 μm z-sampling step size. A higher camera frame rate results in a higher VPS, more z-planes per volume, and a smaller z-sampling step size. The scientific Complementary Metal–Oxide–Semiconductor (sCMOS) cameras commonly used by the scientific community (such as the Hamamatsu ORCA Flash and Andor Zyla) can only reach a frame rate of 400 Hz for a C-FOV of 512×1280 , which can only support the scan of 2 z-planes at 200 VPS. While other cameras, such as the Lambert HiCAM Fluo⁶⁸ and the Teledyne Kinetix⁶⁹ can reach a speed of 3000-4000 Hz, the HiCAM Fluo has lower than desired quantum efficiency (QE: 30 – 50%), which affects pixel sensitivity to detecting fluorescence photons; Kinetix pixels have low full well capacity (~ 200 e-), which is insufficient for our application, where the brightest pixels may generate up to 2000 electrons per frame at the illumination powers needed for acceptable SNR. Thus, we searched for a camera that could overcome these limits. Continued advancements in CMOS technology have resulted in the availability of commercial image sensors that meet the speed and noise specifications for our microscopy system. We used the Gpixel GSPRINT4502 image sensor that supports a high pixel rate of 4.37 GHz in 10-bit mode, with a full well capacity of 7.4k e-, a readout noise of ~ 7 e-, and a QE of 60% at 550 nm. This sensor enables us to capture a C-FOV of 512×1280 pixels at a speed of 3900 frames per second (FPS), effectively covering the entire brain of a larval zebrafish. To further boost imaging speed, we implemented the distributed planar imaging strategy⁷⁰, dividing a 2D-FOV into multiple smaller 2D-FOVs recorded separately using multiple image sensors (**Fig. 2-5**). Utilizing two GSPRINT4502 image sensors in a dual-camera system, we can improve the frame rate to 7300 Hz for a C-FOV of 512×1280 pixels. This enhancement enables the LSM to scan 30 image planes at a maximum volume rate of 243 VPS.

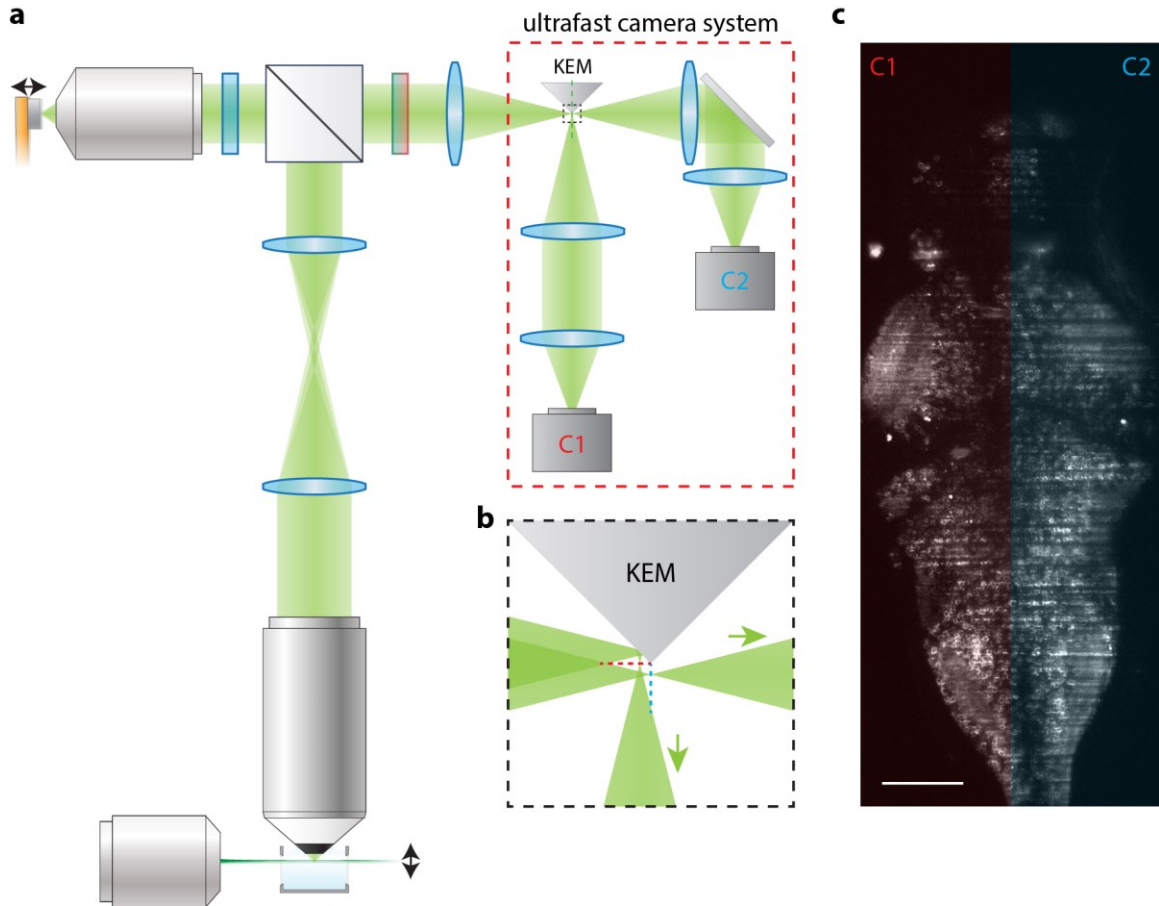


Figure 2-5. Overview of the ultrafast camera system. (a) Images from the high-speed light-sheet microscope are recorded by an ultrafast camera system (red dashed line box) consisting of an image splitter and two ultrafast cameras. Focused images from the microscope are divided by a knife-edge mirror (KEM) into two halves. These split images are then relayed through two identical lens pairs to the ultrafast cameras (C1 and C2) for recording. (b) Enlarged view of the areas in the black dashed box in (a). The KEM splits an image by deflecting only its upper half to a different light path. (c) Stitching raw images from cameras C1 and C2 produces a full section image of the zebrafish brain.

As commercially available cameras incorporating this newly available image sensor were lacking, we designed a custom camera system using this image sensor (**Fig. 2-6**). The custom camera uses the Gpixel GSPRINT4521/10/02 image sensors. The camera system's hardware employs a two-board stacked design, comprising the TOP and BOTTOM boards (**Fig. 2-6a**). The TOP board (**Fig. 2-6b**), an 18-layer printed circuits board (PCB), houses the image sensor chip and a Xilinx Spartan 6 FPGA (Opal-Kelly

XEM6010) used for camera control and acquisition trigger synchronization. The TOP board accommodates 144 pairs of LVDS lines for high-speed data output from the image sensor. These LVDS line trace lengths are carefully matched to minimize propagation delays during data transmission, operating at 1.2 Gbps/pair in double data rate (DDR) format. The data lines are connected to the BOTTOM board via two high-pin count FPGA mezzanine card (FMC) connectors.

The BOTTOM board (Numato Nereid K7) contains a Xilinx Kintex-7 FPGA, which buffers the high-speed data from the image sensor and transmits it to the host computer. Each LVDS' line data delays are measured relative to the data clock at power-up. This delay is then compensated at the FPGA side to ensure data integrity at receiving high-speed data stream at 1.2Gbps. The received data are buffered and re-arranged using the onboard RAM, before transmission to the host computer using a PCIe link. The PCIe communication firmware is modified based on open-source projects: RIFFA28 and Open-Ephys ONIX29. The host PC receives the data using an ANSI-C API from Open-Ephys ONIX⁷¹. The data is displayed, and storage is designed using the Bonsai⁷² reactive programming language.

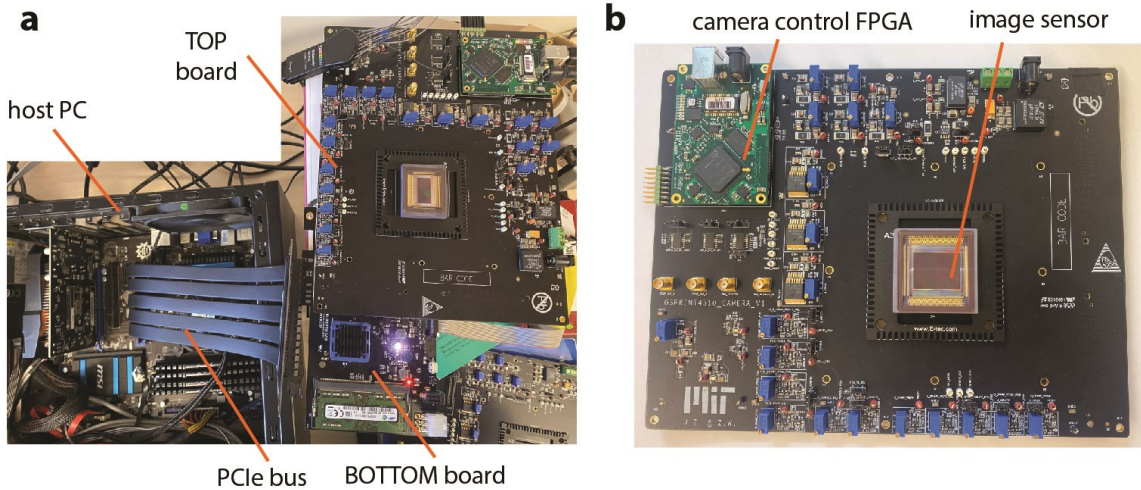


Figure 2-6. Customized high-speed camera system. (a) the camera system is a two board stack design. The TOP board **(b)** hosts the image sensor and uses an FPGA (Xilinx Spartan 6, Opal kelly XEM6010) to handle camera control and trigger synchronization. The BOTTOM board uses an FPGA (Xilinx Kintex-7) with external DDR RAM to buffer and transfer high-bandwidth data (2.6GBps) to the host computer through a PCIe bus.

The custom camera satisfied our design requirements of spatiotemporal resolution, achieving a spatial resolution of 512×1024 with 10-bit output at 3900 FPS and low noise ($< 7\text{e-}$). This capability allowed us to conduct prototype measurements for screening GEVI indicators, establish microscope control systems, and perform whole-brain volumetric imaging with 15 imaging layers at 200 VPS. However, the main drawback of our custom camera was its size, a consequence of utilizing a PCIe link that requires the PC to be in close proximity to the camera (Fig. 2-6). The large size posed challenges for its integration into a distributed planar imaging setup (Fig. 2-5a). While the camera's size could be reduced by adopting existing PCIe cable connectors, such as the Molex iPass connector system, this would necessitate additional time for design modifications.

Commercially available cameras using GSPRTING 4521/10/02 sensors became available near the end of our custom camera's development. We found that both our custom camera and the commercial camera (Ximea CB024MG-GP-X8G3) had the same readout noise performance at our microscope's speed specification. This was quantified using root-mean-square noise measurement in dark, which is calculated by taking the standard deviation of the pixel's values with no incoming light. We used both the custom-built camera and commercial cameras in our experiments. Using two cameras, the distributed planar imaging system achieved a spatial resolution of 512×1280 at 7300 FPS. This allows our LSM to scan 30 image planes at a maximum volume rate of 243 volumes per second (VPS).

2.4 Implementation and control of the microscope

In our high-speed light-sheet microscope, we employed a remote refocusing strategy to rapidly scan the focal plane at hundreds of hertz without physically moving the detection objective.

For the microscope's detection arm (**Fig. 2-1**), we used a high NA objective lens (OL1, $f=9\text{mm}$, $\text{NA}=1.0$, XLUMPLFLN20XW, Olympus) to efficiently gather emitted fluorescence. The fluorescent light passes a 4F system consisting of two tube lenses (L1, $f=200\text{mm}$, TTL200MP, Thorlabs; L2, $f=150\text{mm}$, TTL200-A + $2\times$ AC508-750-A, Thorlabs), and then is directed into a polarized beam splitter (PBS, PBS251, Thorlabs). The polarized light beam deflected by the PBS propagates through a quarter wave plate (QWP, AQWP10M-580, Thorlabs) and then a remote objective lens (OL2, $f=9\text{mm}$, $\text{NA}=0.8$, UPLXAPO20X, Olympus), forming a virtually spherical aberration-free 3D image of the sample. This image is then reflected by a lightweight mirror ($2\times 2\times 1 \text{ mm}^3$, Chroma) glued to a piezo bender actuator (PB4VB2S, Thorlabs). The reflected emitted light then revisits the quarter-wave plate (QWP) and the PBS. Adjusting the orientation of the QWP allows a 90-degree rotation of the emission light's polarization upon its second encounter with the PBS. Consequently, instead of being deflected back, the emission light passes through the PBS, subsequently enters a tertiary tube lens (L3, $f=176\text{mm}$, TTL200MP + AC508-1000-A, Thorlabs), and forms an in-focus image on its focal plane. A band-pass filter (FF01-571/72-25, Semrock) was positioned between the PBS and L3 as an emission filter.

To achieve the kilohertz frame rate essential for whole-brain voltage imaging, we split and captured the images using two ultrafast cameras (Ximea CB024MG-GP-X8G3, or in original prototype form, our customized camera, **Fig. 2-6**), effectively doubling the camera frame rate. The in-focus images produced by L3 were divided into two halves using a knife-edge mirror (KEM, MRAK25-P01, Thorlabs), with its edge aligned with the image's central longitudinal axis. The mirror deflected half of the image into an ultrafast CMOS camera though a two-component relay system ($f=211\text{mm}$, ACT508-1000-A + $3\times$ ACT508-750-A, Thorlabs; $f=50\text{mm}$, Thorlabs TL4X-SAP or Nikon CFI Plan Apo 4X). The other half was relayed by an identical system and then imaged by another ultrafast camera of the same specifications.

For fluorescence excitation (**Fig. 2-7**), we generated a light sheet using a Powell lens and scanned it over the sample using a galvanometer mirror scanner. In the excitation light path (**Fig. 2-7a**), a single-mode laser beam ($\lambda=515\text{nm}$, Cobolt 06-MLD, HÜBNER Photonics) is first coupled into a single-mode optical fiber (P1-460B-FC-1, Thorlabs) through an aspherical lens ($f=3.1\text{ mm}$, C330TMD-A, Thorlabs). The light cone output from the single-mode fiber is collimated using an achromatic doublet lens ($f=9\text{ mm}$, Edmund Optics) to form a $\sim 1.8\text{ mm}$ diameter (at $1/e^2$) beam. This collimated beam passes through a Powell lens (LOCP-6.0R05-1.4, Laserline) and then diverges along one axis. The laser light then goes through a 4F system ($f_1=50\text{ mm}$, $f_2=75\text{mm}$) before being redirected by a galvanometer mirror scanner (Saturn 5B, ScannerMAX) into a scan lens ($f=70\text{mm}$, CLS-SL, Thorlabs). The scan lens generates a light sheet at proximity to its focal plane. This light-sheet is then conjugated onto the sample through a reversed $4\times$ microscope system consisting of a 200-mm focal length tube lens (TTL200, Thorlabs) and a $4\times$ microscope's objective lens ($f=50\text{mm}$, NA=0.2, CFI Plan Apo 4X, Nikon). We adjusted the laser beam diameter using 3D printed circular apertures placed between the fiber collimating lens and the Powell lens to optimize the light sheet's thickness and profile. The light sheet illuminated at the sample has an approximate width of 1 mm, around 20% larger than the fish brain's length. Axial scanning of the light sheet was performed using the single-axis galvanometer mirror scanner, which can support a sinusoidal scan frequency exceeding 2000 Hz with our desired scan range. To mitigate any stimulation of the fish's visual system caused by the excitation laser, we placed a circular opaque optical mask ($\Phi 900\text{ }\mu\text{m}$, OD>5, PhotomaskPORTAL, **Fig. 2-7a**) at the scan lens's focal plane (also the focal plane of the tube lens of the $4\times$ microscope). The optical mask was made by applying a circular chromium coating with a diameter of $900\text{ }\mu\text{m}$ on one side of a square glass piece. This glass is 3 mm thick and measures 14 mm on each side.

We used a Powell lens to generate a real 2D light sheet for simultaneous excitation of all the fluorophores on the microscope's focal plane. This is different from the strategy in many previous works^{27,49,73} where a 2D image plane was illuminated by digitally scanning a Gaussian beam across the plane. We chose to use a real light sheet instead of a digital light sheet based on the consideration of excitation efficiency. Fluorophore's excitation efficiency drops as the excitation intensity increases, due to a decreased

percentage of ground state fluorophores. This fluorescence saturation effect cannot be neglected for voltage imaging, where a high excitation intensity is typically required to acquire sufficient emission photons. Compared to simultaneous excitation of a 2D plane using a real light sheet, the digital scanning strategy excites every fluorophore for only a fraction (typically <1%) of the total exposure time, thus requiring a fluorophore brightness much higher (by a factor equals to the ratio between the exposure time and the excitation time for the fluorophore) to gather the same number of photons. To quantify the fluorescence saturation effect of the GEVIs in our experiments, we measured the brightness of JF525 dye at various intensities of 520-nm excitation light at room temperature. We found the JF525 fluorescence intensity increases nonlinearly with the excitation intensity, following a relation: $I_{JF525} \sim 1 / (1 + 11/I_{520nm})$, where I_{JF525} is the normalized JF525 fluorescence intensity and I_{520nm} is the excitation intensity in W/mm^2 . In our voltage imaging experiments, fluorophores were excited by a real 2D light sheet at $\sim 8.6 W/mm^2$, yielding a $\sim 44\%$ maximum fluorophore emission rate. It is theoretically unfeasible to collect the same number of photons in our experiments using a digitally scanned light sheet.

We quantified the thickness of the light sheet by acquiring its cross-section images that are perpendicular to the illumination axis (y-axis). To do so, we replaced the sample with a right-angle mirror prism to reflect the light sheet upright into the detection objective lens. The cross-section images were then acquired on a camera placed at an intermediate image plane in the detection path. We translated the mirror prism along the illumination axis using a linear translation stage to sample the cross-section images at different y-axis locations. The cross-section images along a 400- μm y-axis range were shown in **Fig. 2-7b**. The light sheet's full-width-at-half-maximum (FWHM) was measured according to these images (**Fig. 2-7c**).

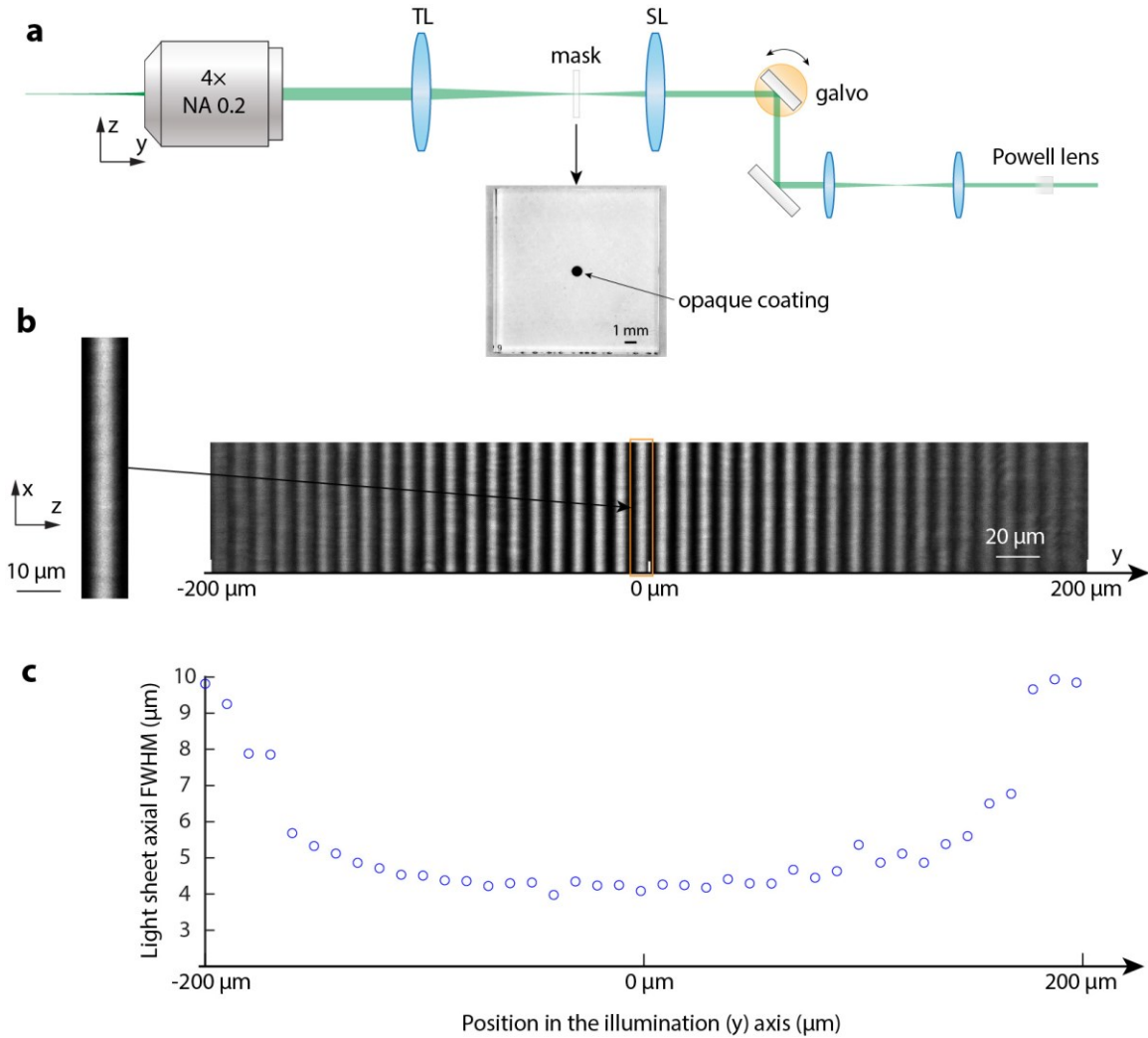


Figure 2-7. The light path for light-sheet illumination and measurement of the light sheet profile. (a) Schematic diagram of the light-sheet illumination arm. Collimated laser (from the right side) first passes through a Powell lens, a 4F system, then reflects on a galvo mirror scanner, passes through a scan lens (SL), a tube lens (TL), and finally illuminates on the sample from a 4x objective lens. An optical mask is placed at the sample's image plane to prevent direct light entering the fish's eye. **(b)** Cross-section images of the light-sheet along the illumination axis (y-axis). **(c)** Axial full-width-at-half-maximum (FWHM) of the light sheet at different locations on the illumination axis.

We devised a high-speed remote scanning light-sheet microscope to address the technical demands of whole-brain distributed voltage imaging in larval zebrafish (**Fig. 2-1**). This innovation caters to the needs of imaging a whole zebrafish brain volume ($\sim 900 \times 370 \times 200 \mu\text{m}^3$) at a volume rate of 200.8 Hz, and ensures 1.46-μm (effective pixel

size limited; effective pixel size: 0.73 μm , *effective pixel size =*

$$\frac{\text{camera pixel size}}{\text{system magnification ratio}} = \frac{4.5}{6.16} \mu\text{m}$$
) lateral and 11.7- μm (z sampling step size limited, z sampling step size: 5.86 μm) axial resolution across the whole 3D-FOV.

In our microscope (**Fig. 2-1**, **Fig. 2-7**), the sample is excited by a laterally illuminated light sheet (515 nm wavelength) that was generated using a Powell lens and scanned using a galvo mirror (not shown, as these are used in the conventional way). The emitted fluorescence from the sample was collected by a high-NA (water immersion, NA=1.0) detection objective lens. An upright, isotropically magnified image of the sample was generated at a remote location using a remote objective lens (air, NA=0.8). This image was then reflected by a lightweight mirror, essentially repurposing the remote objective as a virtual tertiary lens for reimaging. By swiftly actuating the lightweight mirror (~0.01 g) with a piezo bender scanner—akin to scanning the tertiary virtual lens—we achieved fast scanning of the focal plane across a 200- μm axial range at rates of up to 300 Hz. The magnification ratio between the remote image and the sample was designed to be 1.33 to match the ratio between refractive indices in the sample space (water) and in the remote image space (air). This magnification ratio-refractive index ratio match ($\text{Mag}_{\text{remote}} = n_{\text{sample}}/n_{\text{remote}}$) allows eliminating the spherical aberrations resulted from refocusing^{52,53}.

As the emitted fluorescence passes through a polarized beam splitter (PBS) twice in our setup, emitted fluorescence of a particular polarization (~50% assuming the emitted fluorescence is totally unpolarized) will be lost. One way to restore the unused fluorescence would be to add an identical secondary remote scanning module (i.e., a remote objective lens, a quarter wave plate, and a piezo-driven remote mirror) at the other port of the PBS and to drive the secondary piezo scanner in synchrony with the first piezo scanner.

To reduce aberrations and enhance the 3D-FOV in our microscope system, we simulated the aberrations of different optical designs (**Fig. 2-4**). We used our results to find an optimal configuration that minimized the aberrations contributed by the remaining optical elements in the detection light path, such as tube lenses, a polarized beam splitter (PBS), and relay lenses. We borrowed the concept from earlier OPM work⁵⁸ to construct tube lenses with desired parameters using commercially available lenses.

We chose a $6.16\times$ system magnification ratio to keep a balance between the camera frame and the spatial resolution: with this magnification ratio, the whole zebrafish brain can fit into a 512×1280 pixel C-FOV to allow the camera to run at high frame rates (in our case, up to 7300 FPS); on the other hand, the $0.73\text{-}\mu\text{m}$ effective pixel size corresponding to this magnification ratio is $\sim 1/9$ of the average neuron soma diameter ($6.62\text{ }\mu\text{m}^{27}$) in larval zebrafish, which is sufficiently small so that it will not be a bottleneck for resolving single cells. Increasing the system magnification ratio will increase the spatial resolution but will also increase the C-FOV and reduce the camera frame rate.

For high-speed, low-latency, coordinative control of various hardware components in our microscope, a real-time LabVIEW program was developed and implemented in a compactRIO system equipped with an FPGA (cRIO-9038, National Instruments). This program enables simultaneous analog and digital outputs through I/O modules (NI-9262, NI-9401, National Instruments). The output signals were updated every $4\text{ }\mu\text{s}$, one tenth of the exposure time for each frame, ensuring control precision. These output signals were repeated every $4980\text{ }\mu\text{s}$, corresponding to a volumetric scan rate of 200.8 Hz.

2.5 Characterization of the microscope's resolution

We empirically characterized the system resolution by imaging the 3D point-spread-functions (PSFs) of 200-nm diameter red fluorescent beads (emission wavelength = 605 nm) that were randomly distributed in 1% agarose. We did not find <500 nm diameter beads with 550-nm emission wavelength to mimic the emitted fluorescence of the Positron2₅₂₅-Kv indicator that we used (see below for details of voltage indicator choice, in “**3.1 Testing different GEVIs in cultured neurons and larval zebrafish brains**”). We chose to image red (605 nm emission) beads instead of green beads (515 nm emission) because longer emission wavelengths, which enlarge the PSF, avoid overestimation of the

microscope's resolution, and because green beads cannot be efficiently excited by our light sheet (515 nm wavelength). To accurately reflect the effective resolution affected by motion blur due to continuous translation of the focal plane during exposure, we imaged the PSF while the microscope continuously scanned across a 206- μm axial range at 200.8 Hz. Due to our microscope's low magnification ratio ($6.16\times$), the lateral effective pixel size ($0.73\ \mu\text{m}$) could not adequately sample PSFs in the x and y axes. To measure the full-widths-at-half-maximum (FWHMs) of the lateral PSF (x-y), we fitted the PSF using a 2D gaussian function (**Fig. 2-8a**). The x-y position and the shape of the gaussian function were iteratively updated until the correlation was maximized between the measured lateral PSF and the 2D gaussian function image that was down-sampled to the same $0.73\text{-}\mu\text{m}$ effective pixel size (**Fig. 2-8a**). Then lateral FWHMs of the PSF were measured as the FWHMs of the fitted gaussian function. To measure the axial (z) FWHM of the PSF, we used a one-dimensional dual-gaussian function to fit the axial line profile that contained the brightest pixel of the 3D PSF. Then, the FWHM was measured on the fitted profile (**Fig. 2-8**). According to our measurements, a lateral FWHM of $\sim 1\ \mu\text{m}$ and an axial FWHM of $\sim 3.5\ \mu\text{m}$ of the PSF were maintained across the full measured 3D-FOV of $\Phi 900 \times 200\ \mu\text{m}^3$ (**Fig. 2-8b-f**). These values are larger than the theoretical FWHMs ($0.37\ \mu\text{m}$ lateral and $1.21\ \mu\text{m}$ axial). This difference comes from the motion blur of continuous scanning and the lateral effective pixel size: (1) when imaging the PSF, the microscope's focal plane continuously translated across $\sim 3\ \mu\text{m}$ during the exposure of each frame, so that each measured pixel was blurred as an average of the intensity of the real PSF across a $\sim 3\text{-}\mu\text{m}$ axial range, significantly increasing the 3D size of the measured PSF. (2) The lateral effective pixel size ($0.73\ \mu\text{m}$) in the images is larger than the real PSF's lateral (xy) size. Therefore, each pixel in the images acted as an averaging window applied to the real PSF, which smoothed the intensity peak of the real PSF and lowered the half maximum threshold to measure FWHMs, increasing the FWHM values. Nevertheless, considering the $0.73\text{-}\mu\text{m}$ lateral and $5\text{-}6\text{-}\mu\text{m}$ axial (z) sampling step size, our system maintains spatial resolution that is only bounded by effective pixel size and the z sampling step size across a $\Phi 900 \times 200\ \mu\text{m}^3$ 3D-FOV. According to Nyquist's theorem, the $0.73\ \mu\text{m}$ effective pixel size in our system corresponds to a lateral resolution of $1.46\ \mu\text{m}$, around one-fifth of the average diameter ($6.62\ \mu\text{m}^{27}$) of neuron somas in zebrafish.

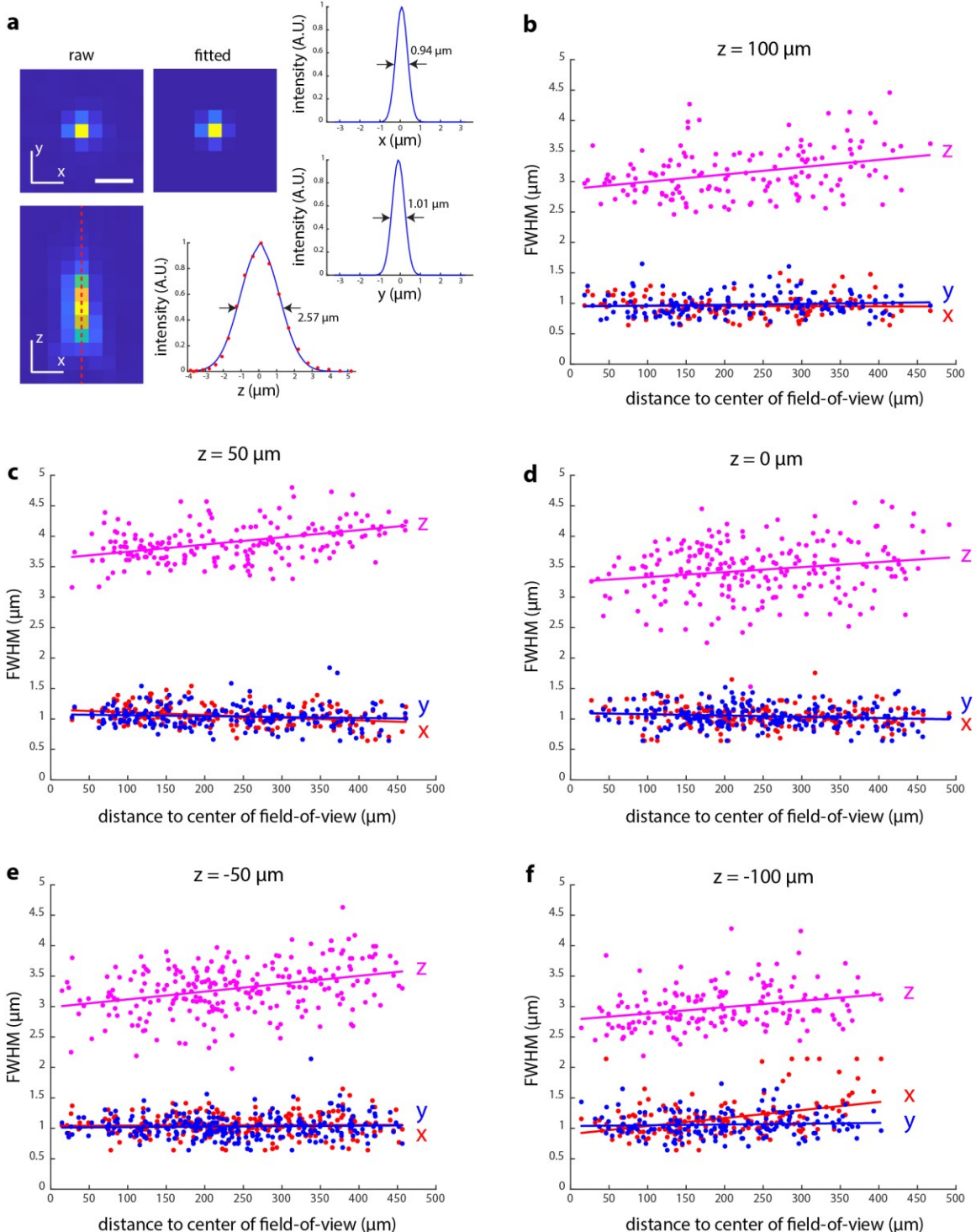


Figure 2-8. Characterization of system point spread functions (PSFs) over the entire imaging field-of-view. (a) Measuring the full-width-at-half-maximum (FWHM) of a PSF. On the left, the raw xy and xz sections that intersect the brightest voxel of the 3D PSF are

shown. The xy section is fitted by a 2D Gaussian function. The fitted image is displayed in the indicated panel. On the right, x and y cross-section profiles of the fitted Gaussian function are shown, and FWHM values are marked. The axial (z) FWHM is determined by fitting the PSF's axial line profile with a double Gaussian function. **(b-f)** Visualization of the FWHM measurements of PSFs at varying radial positions and depths.

Chapter 3

Development of genetically encoded voltage indicator (GEVI) transgenic zebrafish lines

3.1 Testing different GEVIs in cultured neurons and larval zebrafish brains

To determine the best GEVI to use in larval zebrafish, we tested multiple high brightness GEVIs in both cultured neurons and fish. These GEVIs include: ASAP3¹¹, Voltron2⁷⁴, Positron2¹⁰, Ace-mNeon2¹⁴, pAce¹⁴.

We chose to use Positron2-Kv after we tested and compared five different voltage indicators in larval zebrafish. The five indicators were ASAP3-Kv¹¹, Voltron2-Kv⁷⁴, Ace-mNeon2-Kv¹⁴, pAce-Kv¹⁴, and Positron2-Kv¹⁰. We first transiently expressed the five indicators in larval zebrafish using embryonic micro-injection⁷⁵. We imaged their spontaneous activity and compared their SNRs per action potential (SNR_{AP}), which were calculated as the ratio between the fluorescence intensity change per action potential and the shot noise at the spike peak per neuron per frame ($SNR_{AP} = (N_{peak} - N_0) / \sqrt{N_{peak}}$, N_{peak} the detected photon number at the spike peak per neuron per frame, N_0 the detected

photon number at the resting potential right before the measured spike per neuron per frame; these peaks and resting potentials were estimated by eye). We observed that, compared to ASAP3-Kv, Positron2-Kv and Voltron2-Kv exhibited $\sim 10\times$ brightness, while Ace-mNeon2-Kv and pAce-Kv showed $\sim 5\times$ brightness, all measured at the resting state. This brightness difference might result from a difference in molecular brightness when expressed in the zebrafish milieu, or a difference in expression density on zebrafish neural membranes. We found that Voltron2-Kv and Positron2-Kv exhibited the highest SNRs among all tested indicators, in the zebrafish that we made, $\sim 1.4\times$ of those of Ace-mNeon2-Kv and pAce-Kv, and $\sim 2.4\times$ of that of ASAP3-Kv. To test Voltron2-Kv and Positron2-Kv indicators in zebrafish, we transiently expressed the two genes in larval zebrafish brains by injecting 3×UAS:Positron2-Kv and 3×UAS:Voltron2-Kv plasmids into the single-cell stage embryos from transgenic HuC:Gal4 fish. We imaged the injected larval zebrafish brains at 333 Hz using a widefield microscope at 5 days post fertilization (dpf) after staining them with JF525 dye and screening them at 4 dpf (**Fig. 3-1**). Both Positron2-Kv and Voltron2-Kv had good localizations on neuron soma membranes (**Fig. 3-1a,c**). The two indicators exhibited a $\sim 20\%$ positive and a $\sim 20\%$ negative fluorescence responses to spontaneous action potentials, respectively (**Fig. 3-1b,d**).

We then constructed transgenic zebrafish lines with pan-neuronal expression of Voltron2-Kv and Positron2-Kv using the Tol2 transposon system⁷⁵. We used the Gal4/UAS system⁷⁶ to express Voltron2-Kv and Positron2-Kv, with the Gal4 gene driven by the pan-neuronal promoter HuC⁷⁷. For each of the Positron2-Kv and Voltron2-Kv indicators, we made one fish line. We didn't observe much voltage activity in the Voltron2-Kv fish line we made, which could have been due to any number of factors, many of which have nothing to do with Voltron2 itself; given that our goal was simply to probe whether our microscope was capable of imaging voltage in neurons distributed across an entire zebrafish brain, we used the Positron2-Kv fish line in our experiments, as a somewhat arbitrary choice.

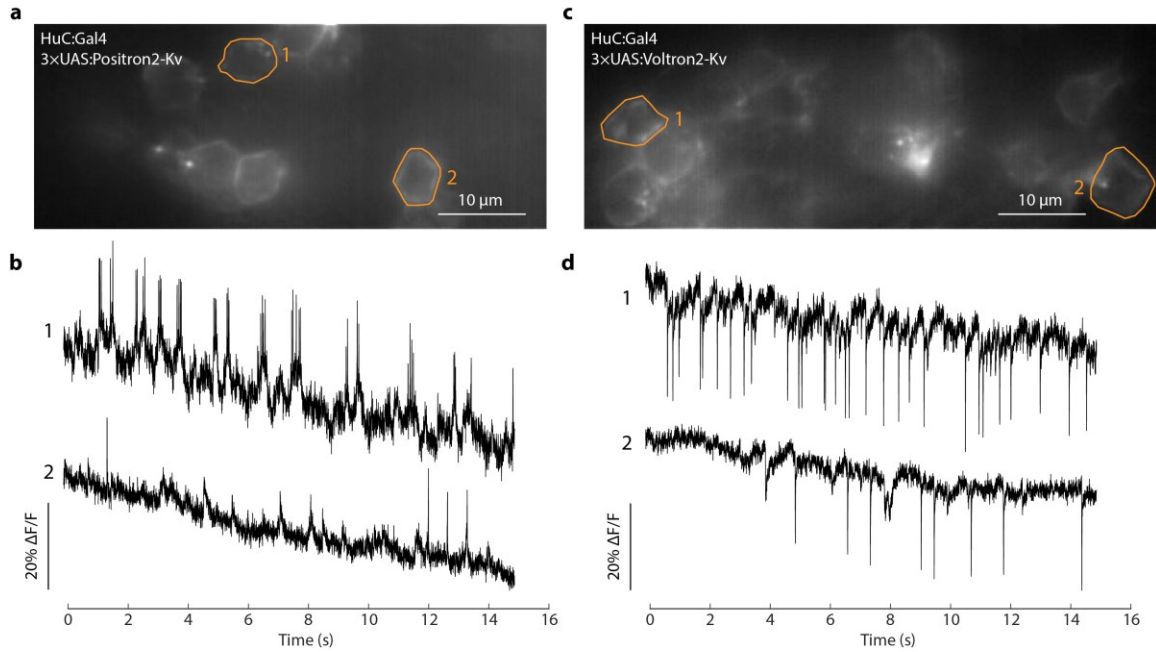


Figure 3-1. Comparison of Positron2-Kv and Voltron2-Kv indicators in zebrafish using transient gene expression. (a) Widefield imaging of larval zebrafish neurons with transient Positron2-Kv expression. (b) Spontaneous neural activity traces extracted from the neurons enclosed by orange lines in (a). (c) Widefield imaging of larval zebrafish neurons with transient Voltron2-Kv expression. (d) Spontaneous neural activity traces extracted from the neurons enclosed by orange lines in (c).

3.2 Construction of transgenic GEVI zebrafish lines

The *Tg(HuC:Gal4; 3×UAS:Positron2-Kv)* and *Tg(HuC:Gal4; 3×UAS:Voltron2-Kv)* transgenic zebrafish lines were generated through embryonic micro-injections using the Tol2 transposase system³¹. First, Tol2 DNA plasmids containing the 3×UAS:Positron2-Kv gene or the 3×UAS:Voltron2-Kv gene (synthesized, Epoch) were co-injected with transposase (synthesized using SP6 Transcription Kit, ThermoFisher) into single-cell stage zygotes from *Tg(HuC:Gal4)* nacre transgenic fish. The mixed injection solution contained

20 ng/ μ L DNA plasmids, 50 ng/ μ L transposase, 0.1% phenol red solution (Sigma), all diluted in DNase/RNase-free distilled water (ThermoFisher). Once made, the injection solution was immediately placed on ice to slow the transposase degradation. To make injection needles, we pulled borosilicate glass capillaries (0.5 mm inside diameter, 1.0 mm outside diameter, 10 cm length, Sutter Instrument) using a micropipette puller. The injection solution was loaded into the pulled needles by submerging the inverted top opening of the needle in the solution for a few minutes, which allowed the solution gradually ascending to the needle's tip via capillary action. The injections were conducted under a stereoscope using a microinjector. Before injection, we carefully trimmed the needle's tip with forceps and adjusted the microinjector's injection pressure to control the volume of each injection, which was visible in a red hue due to phenol red. For each embryo, the volume of the injection solution was calibrated to approximately 1/7 of the length of the zygote at the single-cell stage. Following injection, the embryos were incubated in fish facility water at 28°C for development.

At 3 dpf, zebrafish embryos were incubated in fish facility water containing 3 μ M JF₅₂₅-HaloTag for two hours. Residual dye molecules were then gently washed off using fresh fish facility water before the embryos were visually screened for green fluorescence under a fluorescence stereoscope. Fish larvae exhibiting fluorescence, known as F0 fish, were isolated and raised to maturity. Once they reached 3 months post-fertilization, these F0 fish were out-crossed with either Tg(HuC:Gal4) or nacre adult fish. Their progeny was stained with JF₅₂₅-HaloTag dye solution and screened at 3-4 dpf. Fish larvae with pan-neuronal fluorescence were selected and raised to establish a transgenic line.

In our transgenic Positron2-Kv fish, we saw well localized fluorescence on the membranes of individual neurons in the brain (**Fig. 3-2, Fig. 4-1a, b**). Specifically, neurons on the ventral side of the brain (**Fig. 4-1a, z=62 μ m, 34 μ m**) were densely packed, as expected for pan-neuronal expression. However, on the dorsal side of the brain, we sometimes observed dark areas where neurons seemed to be unlabeled (**Fig. 4-1a, z=147 μ m, 119 μ m, 91 μ m, cyan arrows**). These unlabeled areas could have resulted from several possibilities. First, the transgenes might not have been inserted at optimal locations in the zebrafish genome, so their expression could have been suppressed in specific types of neurons. To remedy this, in the future, we could perform more embryonic micro-injections

to generate a large pool of larval zebrafish with random transgenic insertions in the genome, and screen for the fish with the most pan-neuronal expression. Second, because the Positron2-Kv indicators need to be stained with a chemical dye solution to gain fluorescence^{8,10,74}, indicator proteins synthesized during the period (~4 hours in our experiments) between the staining and the light-sheet imaging would not be labeled with dye. This period is needed to incubate the fish in fresh water to remove excess dye molecules that did not bind voltage indicator proteins and to mount the fish in a customized water chamber for imaging.

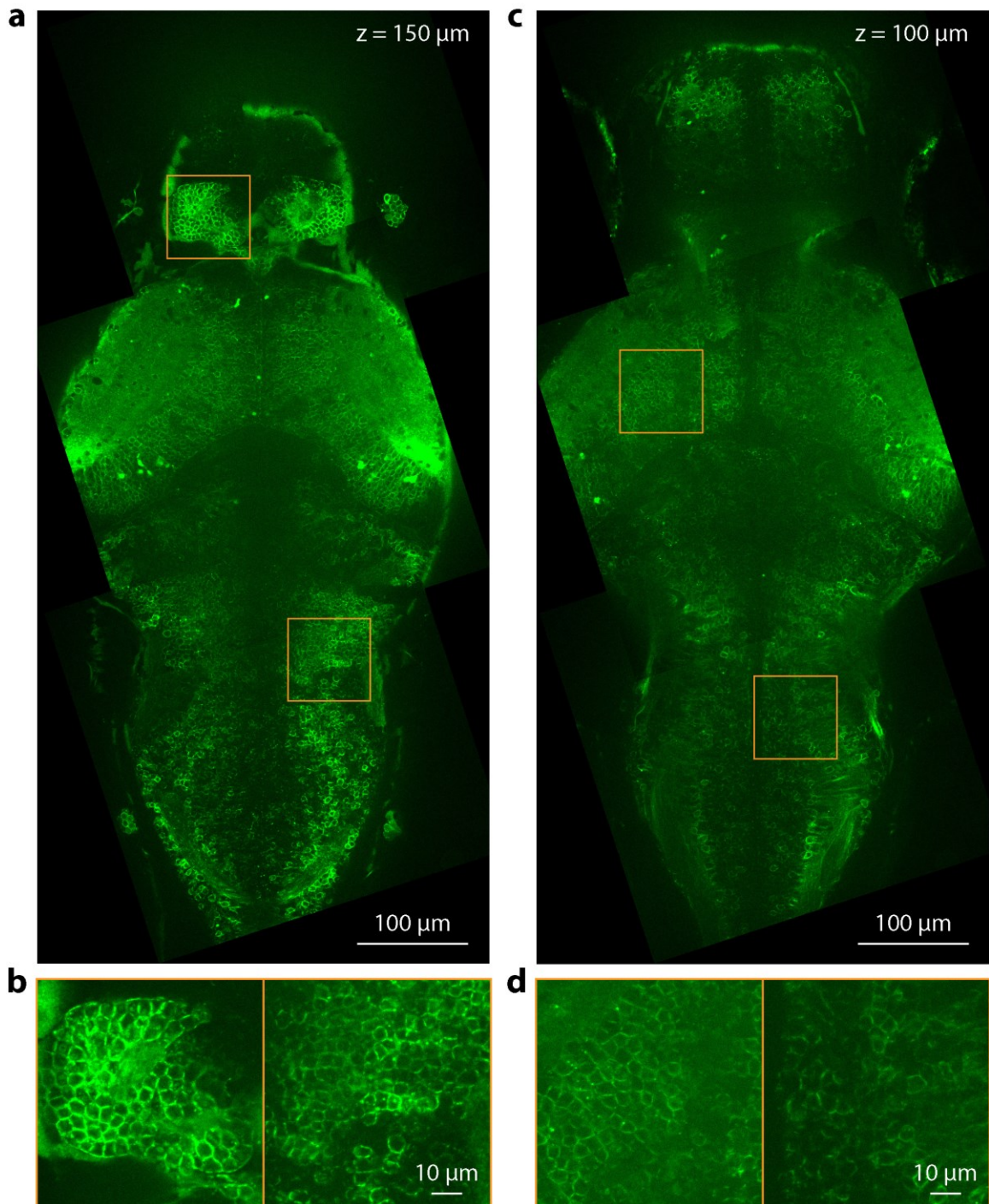


Figure 3-2. Confocal microscopy images of a transgenic Positron2-KvJF525 fish brain at 5 dpf. (a)(c) Single z-plane images of brain at 150- μm and 100- μm locations from the brain's ventral bottom plane ($z=0$). (b)(d) Zoom-in views of the selected regions in (a) and (c) showing membrane labeling of densely packed neurons.

Pan-neuronally labeled larval zebrafish at 5-6 dpf. were embedded and imaged under our high-speed microscope. For Positron2-Kv fluorescence labeling, the fish were incubated in JF₅₂₅-HaloTag ligand dye solution for two hours prior to imaging. We tried to minimize the time gap between staining and imaging, thereby reducing the likelihood of having neurons that were born post-staining and remained unlabeled. Subsequent screening identified and isolated the positive fish for imaging. To mitigate motion-induced artifacts, we paralyzed the fish by briefly incubating the fish in fish facility water containing 0.3 mg/mL pancuronium bromide (Sigma) until the fish showed no movement in response to tactile stimuli applied using closed forceps tips. Then the fish was mounted on a 3D-printed holder in 3% low-melting agarose (Sigma), all within a petri dish (**Fig. 3-3**). The holder design allowed the fish's torso to be cradled within a groove and the fish's tail end extended out of the holder. Upon the solidification of the agarose, fresh fish facility water was added into the petri dish, and agarose around the fish's head, especially agarose on the side intended for light-sheet illumination, was carefully removed using forceps. The fish's body was still restrained in agarose. Following this, the holder, along with the embedded fish, was transferred to a 3D-printed sample chamber. The chamber was designed with transparent glass coverslip walls and filled with fish facility water. The holder was adhered to the inside of the chamber using tiny magnets. The sample chamber was attached to a 3D translation stage under the detection objective lens for imaging.

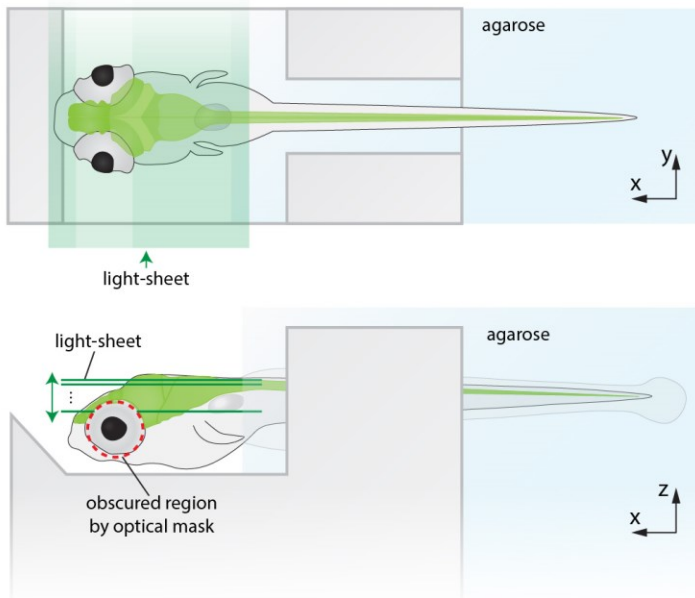


Figure 3-3. Illustration of a mounted larval zebrafish for light-sheet imaging. A larval zebrafish with pan-neuronal labeling is immobilized on a 3D printed holder, with its body restrained in agarose gel and its head exposed. A light sheet, illuminated from one side, scans the fish's brain along the z-axis. Excitation light at the fish's eye areas is obscured using a circular opaque optical mask (red dashed line). The top view (top of the panel) and the side view (bottom of the panel) of the fish are shown.

All procedures related to zebrafish husbandry and handling were conducted in accordance with the US National Institutes of Health Guide for the Care and Use of Laboratory Animals and approved by the MIT Committee on Animal Care (protocol number: 1221-100-24).

Chapter 4

Imaging the voltage of neurons distributed throughout entire larval zebrafish brains

4.1 Imaging the spontaneous voltage activity in the larval zebrafish brain

To demonstrate the utility of our microscope, we sought to choose a voltage indicator with sufficient performance to explore the kinds of insights that could be derived. There is, admittedly, no perfect voltage indicator at the current moment, and each voltage indicator incurs specific tradeoffs and sacrifices. For example, one voltage indicator may be very bright or exhibit high SNR, but the kinetics may be challenging to capture. Another may have more ideal kinetics but be too dim. Acknowledging that voltage indicators are improving rapidly, and thus, the best voltage indicator by the time this paper is published might be much better than the ones available today, we focused our attention on the question of whether whole-brain voltage imaging was crossing the threshold of being feasible, rather than focusing on any one voltage indicator. Specifically, we wanted to know if whole-brain voltage imaging could reveal patterns of neural activity that one could

not observe with whole-brain calcium imaging, which might provoke new hypotheses of neural computation.

Using our microscope, we imaged the whole-brain neural voltage of 5-6 dpf larval zebrafish that have pan-neuronal expression of the Positron2-Kv¹⁰ voltage indicator (**Fig. 3-3, Fig. 4-1**). Whole-brain spontaneous voltage activity was captured at a volume rate of 200.8 Hz for 35s in an imaging trial, which produced approximately 250 GB image data. For a volumetric scan, each brain slice was illuminated with a light sheet for a duration of 40 μ s. The light sheet had a temporal power of 43 mW, corresponding to an average excitation power of 10.4 mW on the sample during imaging.

We imaged intact, awake larval zebrafish mounted using 3% low-melting agarose on a 3D printed holder in a customized water chamber (**Fig. 3-3**), with the fish's head exposed and the tail free. We recorded the tail movement at 500 Hz using a behavior camera. When analyzing the light-sheet images, we observed significant motion artifacts due to tail movement and muscle contractions, which corrupted the neural voltage activity. This motion was multidirectional and non-rigid, complicating correction efforts. To mitigate these artifacts, we paralyzed the fish using a muscle relaxant before imaging, as per methods from prior studies^{27,49}, effectively reducing motion to sub-pixel levels. Future endeavors could try to compensate for these motion artifacts through software, better immobilization procedures, or by monitoring fictive behavior.

We chose to image 30 z-planes across a volume of $930 \times 370 \times 170 \mu\text{m}^3$, once every 4.98 ms. This translated to a volume rate of 200.8 Hz and a frame rate of 6024 FPS. Given the 4.98-ms interval between two successive samplings of the same z-plane, ideally, we would use a voltage indicator that has slow kinetics (activation time + deactivation time \approx 5 ms) to avoid the possibility of missing a narrow spike that falls within the 4.98-ms interval. As noted above, there is no perfect indicator, and for the purposes of this study, we chose to value SNR over kinetics. Positron2-Kv, being essentially Voltron with the mutations used in pAce⁷⁸, would be anticipated to have the same kinetics as pAce, meaning activation and deactivation time constants of 0.51 and 0.61 ms at room temperature¹⁴. We note that this means there is a possibility of missing spikes, at our volumetric scan speed of 200 Hz; in the current paper, we confine our observations to those that would be robust

to such a loss. Spike loss could have potentially been reduced by using ASAP3-Kv, which has slower kinetics - 3.7-ms activation and 16-ms deactivation time constants. But, as noted above, ASAP3-Kv has lower SNR compared with Positron2-Kv, which could in principle result in spike loss of a different kind. Thus, for the purposes of this microscope validation, we chose to go with Positron2-Kv.

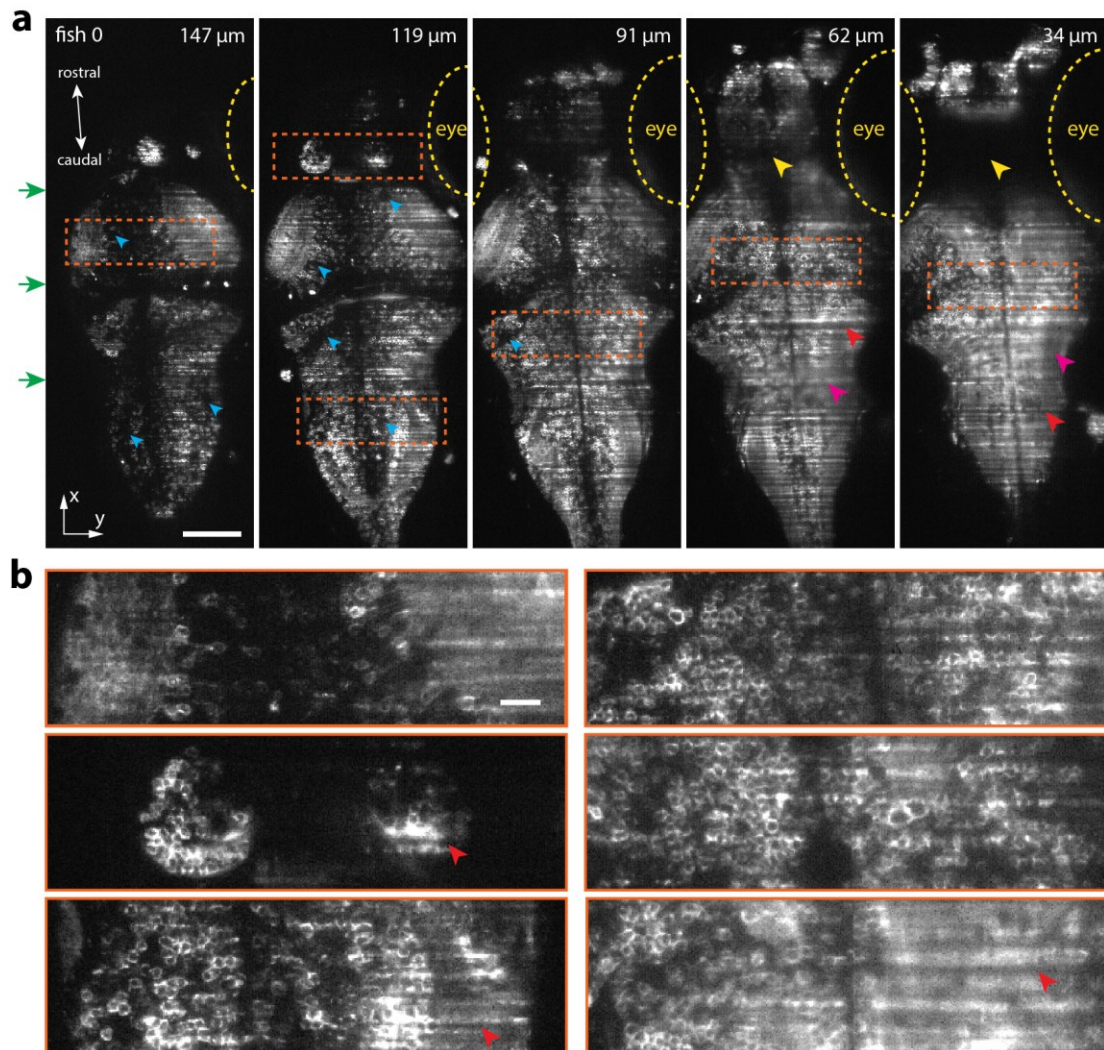


Figure 4-1. Whole-brain voltage imaging at cellular resolutions. (a) Stitched raw images from a whole-brain voltage imaging experiment showing 5 zebrafish brain sections out of a total of 30. Each section was imaged with 40- μ s excitation time at a 200.8 Hz imaging rate. From left to right, green arrows indicate the direction of light-sheet illumination, cyan arrows show examples of unlabeled hollow regions, yellow dashed lines show contours of fish's eyes, yellow arrows indicate brain regions that are shadowed by

the eyes, red arrows highlight “stripe” patterns of light-sheet illumination, magenta arrows indicate blurred regions. Scale bar: 100 μm . **(b)** Enlarged views of the areas highlighted by dashed rectangles in (a). Single neurons are visually distinguishable in these areas, showcasing the microscope’s cellular resolution at various depths in the zebrafish brain. Red arrows highlight “stripe” patterns of light-sheet illumination. Scale bar: 20 μm .

As the ventral side of the larval zebrafish brain is primarily occupied by neurites^{79,80}, imaging beyond a 170 μm axial (z) range yields only 5.4% more neuron somas in the 3D-FOV^{79,80}. By sampling a 170- μm thick volume with 30 image planes, we achieved a step size between adjacent z-planes of 5.86 μm , smaller than the average diameter of neuron cell bodies ($6.62 \pm 0.14 \mu\text{m}$, mean \pm standard error of the mean, n = 298 neurons²⁷) and slightly larger (by 17%) than the 5- μm axial (z) sampling step size that was used to achieve single-cell resolution in previous studies^{27,49}. Under these conditions, we quantified that, on average, the cameras detected $2.1 \pm 0.8 \times 10^4$ (mean value \pm standard deviation, n=15 neurons in 1 fish) photons per neuron per frame. Given the reported ~10% fluorescence response of Positron2-Kv indicator to action potentials¹², this photon number corresponds to a theoretical SNR per action potential of 13.8.

Due to the obstruction of the fish’s eyes, the light sheet cannot illuminate the ventral telencephalon (TL) region (**Fig. 4-1a, yellow dashed lines and arrows, Fig. 4-4b, yellow dashed lines**). We also saw blurred regions (**Fig. 4-1a, magenta arrows**) in the light-sheet images where single neurons cannot be visually resolved. This blurring could have resulted from refraction of the light sheet at the sample, or tissue scattering. We visually examined the raw light-sheet images of a larval zebrafish brain, and on all individual z-plane images, drew contours of the whole brain (**Fig. 4-2, left, orange**), the regions that were shadowed by fish’s eyes (**Fig. 4-2, middle, cyan**), and the blurred regions (**Fig. 4-2, right, magenta**). We found that single neurons were visually distinguishable within individual z-planes in 84.7% of areas of the imaged brain (**Fig. 4-2**). The remaining areas were either shadowed by the fish’s eyes (8.55% **Fig. 4-2, cyan contours**) or too blurred to resolve single cells (6.74%, **Fig. 4-2, magenta contours**). The blurred regions were more concentrated at the lateral right side of the zebrafish brain, as the light sheet entered the brain from the left side (**Fig. 4-2, green arrows**). (We note that this is a problem for calcium imaging as well⁸¹.)

The locations and the proportions of these regions may vary from fish to fish, due to different developmental stages.

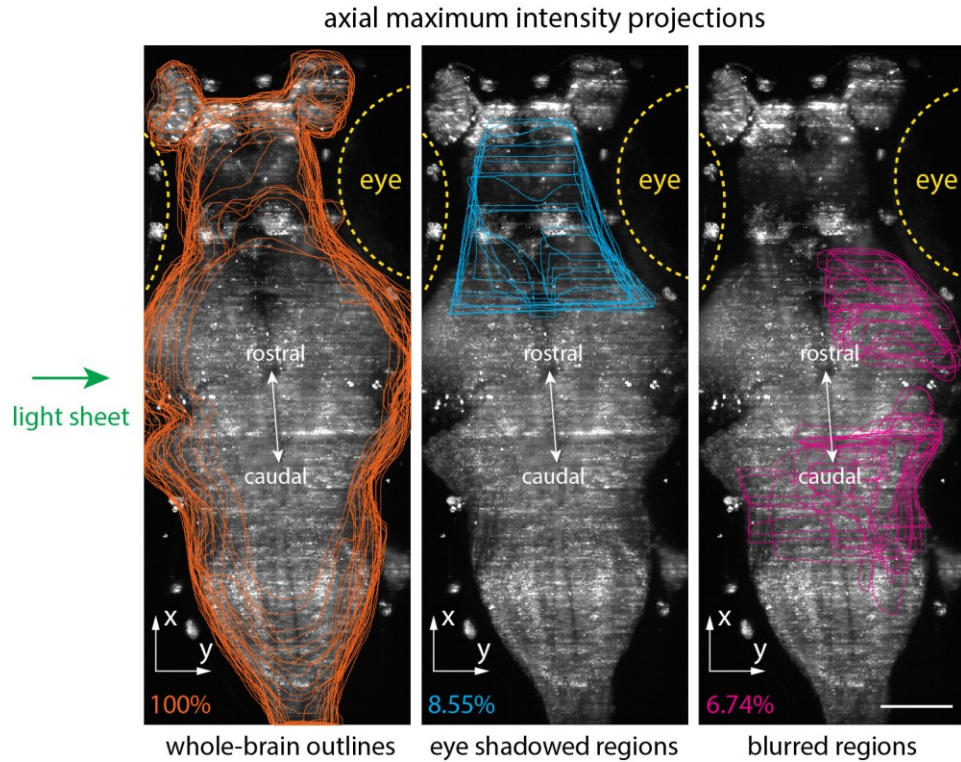


Figure 4-2. Quantifying the eye shadowed regions and the blurred regions as percentages of the imaged whole brain. Contours of the whole brain (orange), the regions that were shadowed by eyes (cyan), and the blurred regions where single cells cannot be resolved (magenta), were drawn on individual z plane images (30 planes in total, $5.86 \mu\text{m}$ z step size) of the whole zebrafish brain. To draw these contours, we visually examined the raw image of each z plane and drew the 2D contours of the whole brain (orange), the dark region shadowed by the fish's eye (cyan), and the regions where we could not visually distinguish single cells (magenta). These 2D contours were projected along the z axis and displayed on the axial maximum intensity projections (MIPs) of the imaged brain. Yellow dashed lines indicate the fish's eyes. Within the imaged brain (left, orange contours), 8.55% (middle, cyan contours) of the full brain region was shadowed by fish's eyes, 6.74% (right, magenta contours) was too blurred to visually resolve single cells. The light sheet (green arrow) was illuminated towards the left side of the brain. Scale bar: $100 \mu\text{m}$.

In the raw light-sheet imaging videos, we observed bright and dark “stripe” patterns that are parallel with the illumination axis (y) of the light sheet (**Fig. 4-1, red arrows**).

These stripe patterns are caused by small objects (either stationary ones such as regions of concentrated fish skin pigment, or moving ones such as circulating blood cells and dust particles in the water) at the sample that absorb or scatter the excitation light sheet^{82,83}. These stripe patterns can be seen all over the brain (**Fig. 4-1a, b red arrows**). These stripe patterns affect the observed images by multiplying the unaffected images by the striped patterns. Within 90% of the imaged brain volume, these stripe patterns were static, meaning that the extracted traces were only multiplied by a constant factor that was determined by the static stripe patterns, which would not complicate analyses like spike detection. For the rest of the brain (~10%, scattered across the ventral side of the brain), such stripe patterns changed over time (**Fig. 4-3**), which contaminated neural activity by multiplying it by a factor that changed over time. The contaminated neural activity traces exhibited pulse-like artifacts (**Fig. 4-3; Fig. 4-6, orange arrows**). The prevalence and location of the brain regions where the extracted neural traces were contaminated by the pulse-like artifacts varied between individual fish, possibly due to developmental differences in their circulatory systems.

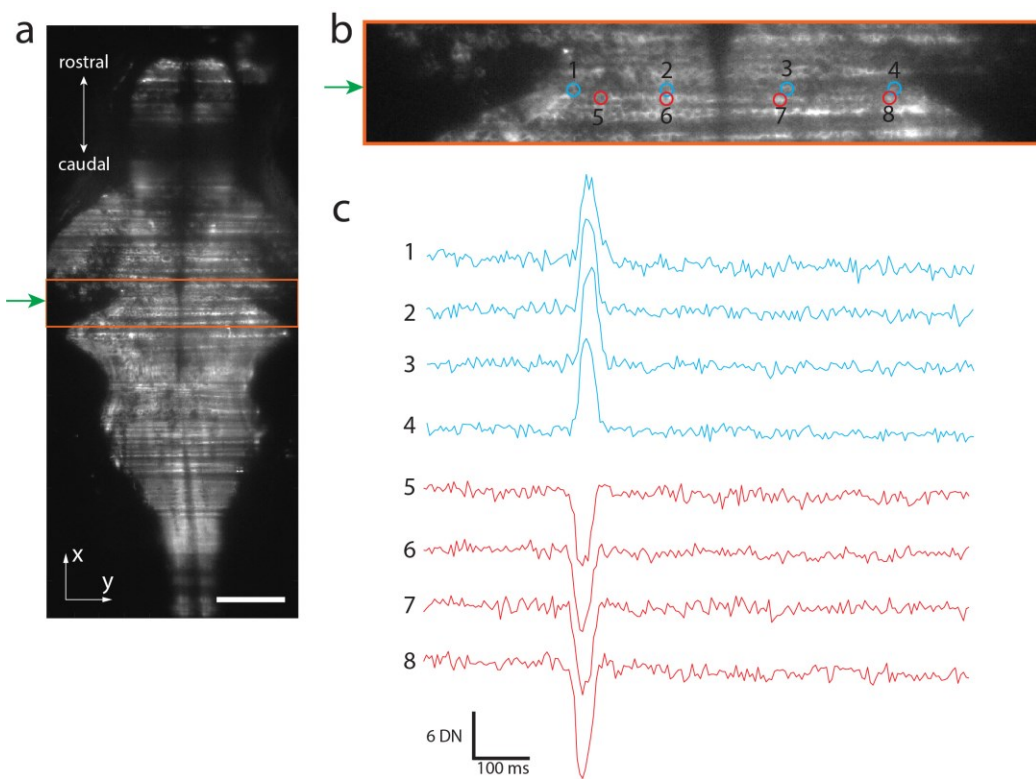


Figure 4-3. Example pulse-like artifacts on the temporal traces of ROIs affected by the stripe artifacts cast by small moving objects in light-sheet imaging. (a) Example frame from a video of a z plane of the larval zebrafish brain. The light sheet is illuminated from the left side of the brain (green arrow). Scale bar: 100 μ m. (b) Zoom-in view of the orange boxed region in (a). The raw temporal traces from example circular ROIs (cyan and red) are extracted. ROIs with the same color lay on the same artifact stripe. (c) Extracted raw temporal traces from the ROIs in (b). The traces from the cyan ROIs exhibited a synchronous positive-going pulse-like artifact, while the traces from the red ROIs exhibited a synchronous negative-going pulse-like artifact. These pulse-like artifacts had a duration width of ~50 ms, much longer than that of an action potential spike. DN: digital number, measurement of the pixel intensity.

To quantify the number of individual neurons our methods could monitor in the zebrafish brain, we manually annotated regions-of-interest (ROIs), in one fish (denoted as Fish 1). During the manual annotation process, we labeled two types of ROIs. Firstly, we identified and outlined objects approximately the size of a neuron (~9 pixels or ~6.6 μ m) with ring-like boundaries. Secondly, for objects of a similar size to neurons, which we tentatively identified as neurons, but were not ring-shaped, we analyzed their temporal intensity traces. We then selected those objects whose intensity traces showed narrow (<20 ms), high amplitude (e.g., >2 \times the standard deviation of the traces), and positive-going spike signals. A second person reviewed the annotated ROIs. The percentage of ROIs that the second person disagreed with was ~5% of all the annotated ROIs. The disagreement concentrated on the cases when examining the intensity traces of an object was needed to decide whether to label the object. For the spontaneous activity datasets, we manually annotated ~1000 neuron ROIs distributed throughout the brain as annotating all the neurons would require lots of time and effort.

We extracted neural activity traces from manually labeled ROIs using the signal extraction algorithms of VolPy⁸⁴, an automatic analysis pipeline for voltage imaging datasets. We did not use the ROIs generated by VolPy's pre-trained Mask R-CNN segmentation network because we found the network failed to identify many neurons that were selected by manual labeling methods, particularly in areas where neuron somas were closely packed. Fig. 4-1 and Fig. 4-4 show raw images (**Fig. 4-1a, b**) and example spontaneous activity traces (**Fig. 4-4a, c**) from a 5.5-dpf larval zebrafish (denoted as Fish

0 in the figure). **Fig. 4-4 a and c** display the activity traces of 120 putative neurons in six brain regions (**Fig. 4-4b**). These regions include the olfactory epithelium (OE, red), telencephalon (TL, cyan), habenula (HB, purple), optic tectum (OT, green), cerebellum (CB, blue), and medulla oblongata (MO, orange) (**Fig. 4-4**), from different lateral locations and axial depths, demonstrating our microscope's capability to monitor voltage dynamics from locations across the whole brain.

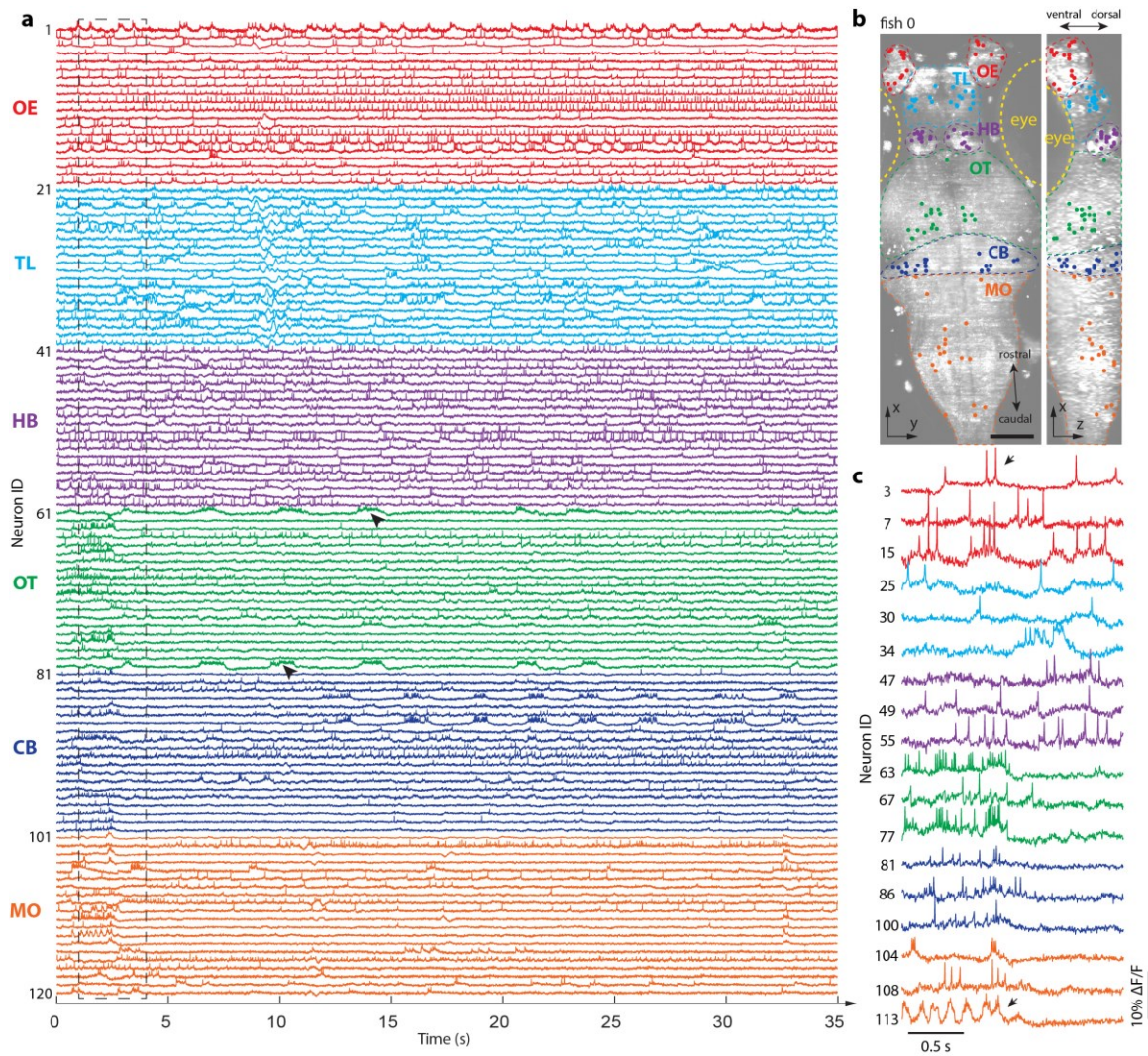


Figure 4-4. Imaging the spontaneous voltage activity of neurons distributed across an entire brain. (a) Spontaneous activity traces of 120 exemplar neurons from 6 brain regions. Different colors signify traces from various regions (referred to in panel **b**), with olfactory epithelium (OE) in red, telencephalon (TL) in cyan, habenula (HB) in purple, optic tectum (OT) in green, cerebellum (CB) in blue, and medulla oblongata (MO) in orange. **(b)** Neural

regions-of-interest (ROIs) of the activity traces in (a), superimposed on the dorsal (left) and lateral (right) maximum intensity projections (MIPs) of the imaged brain. ROIs have the same colors as those of their corresponding activity traces in (a). Brain regions are annotated using dashed lines of different colors, indicated as in **a**. Scale bar: 100 μm . **(c)** Zoom-in views of selected traces enclosed by the dashed rectangle in **a**.

We observed different temporal patterns from these activity traces. Specifically, we saw single spiking events (**Fig. 4-4c, black arrow on the red traces**), burst spiking (**Fig. 4-4a, black arrows on the green traces**), and oscillatory activity (**Fig. 4-4c, black arrow on the orange traces**). These traces exhibited high SNR_{AP} , ranging from 5 – 10.

4.2 Imaging the voltage activity in the larval zebrafish brain during visual stimulation

Zebrafish larvae, like other fish species, possess ultraviolet (UV) sensitive photoreceptors⁸⁵. Due to the differential propagation of light of various colors in water, multicolor visual processing in zebrafish may help detect stimuli such as those related to prey and predators⁸⁵. Additionally, zebrafish larvae exhibit intensity-dependent negative phototaxis away from UV light, perhaps to avoid damage⁸⁶. Whole-brain calcium imaging studies^{32,37} (including one by a first author of this work) have revealed that the onset of high-intensity 405-nm light illumination ($\sim 0.6\text{mW/mm}^2$) – a higher level of illumination than in the aforementioned behavioral studies, chosen for its salience - can induce brain-wide activity in larval zebrafish, within one second.

Here we adapted this light stimulation paradigm to deliver light stimulus to one 5-6 dpf larval zebrafish (Fish 1) from the lateral right side (**Fig. 4-5a**). We recorded whole-brain activity during the light stimulation using the same settings as the spontaneous activity recording, with the only difference being that the fish was exposed to the light

stimulus during imaging. For each trial, the fish was imaged at a volume rate of 200.8 Hz for 35 seconds (**Fig. 4-5b**). To deliver light stimulation, we focused the light from a 405-nm light-emitting diode (LED) (M405L4, Thorlabs) onto the fish, producing a light spot of an approximate diameter of 5 mm. The measured intensity of this light was 0.6 mW/mm². To avoid interference on recorded images from the long-wavelength emissions of the LED, the LED light was passed through a 450 nm short-pass filter (FELH0450, Thorlabs). The light stimulus was turned on 13s post-laser activation, lasting for a duration of 10 seconds, and then subsequently turned off until the 35s imaging trial ended (**Fig. 4-5b**). We performed two identical trials for each fish. To diminish possible effects of sensory adaptation, we kept the fish in the dark for 20 minutes between the two trials. The fish was not moved during the dark interval, so that the fish's neurons would remain at the same location across the two trials, allowing for a comparison of activity from the same neuron across the two trials.

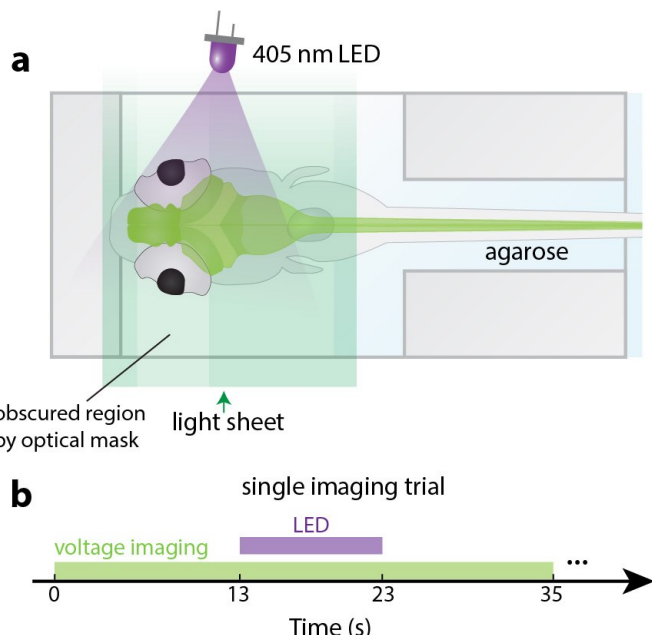


Figure 4-5. Imaging the activity of neurons distributed throughout entire zebrafish brains during visual stimulation. (a) Light stimulation turns on at the lateral-right side of the embedded fish for visual stimulation. **(b)** Timeline of an imaging trial. LED was turned on from t=13s to t=23s in a 35-s imaging trial.

During light-sheet imaging, excitation light can enter the fish's eyes as a visual stimulus. To reduce the visual stimulus from the light sheet, we placed a customized opaque optical mask (Φ 900 μm , optical density >5) in the illumination light path to block direct light from the fish's eyes. This mask reduced the direct excitation light by a factor of at least 10^5 in a 225- μm diameter circular area (Φ 900 μm reduced by 4 times through a tube lens and the 4 \times illumination objective lens) at the fish's eyes (~250 μm in diameter). Excitation light might also enter the fish's eyes through scattering, but we did not quantify the amount of this scattered light due to the difficulty of quantifying light scattering in the fish's brain. Adding the optical mask did not increase the brain volume shadowed by the fish's eyes.

4.3 Image processing and neuron segmentation

To pre-process the raw light-sheet images, we first parsed the data stream from the camera into 30 videos corresponding to 30 z-stack layers. Due to the high data throughput from the camera to the host computer through the PCIe bus (~2.6 GBps per camera), there were rare occasions of lost frames (drop rate: roughly 1 per every 2000 frames, or 0.05%) attributed to data buffer overflow. Frame drops rarely occurred for two consecutive frames. To rectify a lost frame, we simply replaced it with linearly interpolated pixel data from the frames immediately preceding and following it.

We first synchronized videos from the two cameras by time-aligning them at the light-sheet excitation laser onset at the beginning of the experiment. We then merged individual frames from the two cameras into a single frame for each time point. Each C-FOV captures approximately half of the fish's brain from the midline to the left and right lateral sides (**Fig. 2-5**). The combined frame size is 512 \times 1280 pixels, with C-FOV encompassing the entire brain. Lastly, we concatenated corresponding z-stack frames from

successive trials in time into a single video for motion correction, ROI segmentation, and temporal trace extraction.

We applied motion correction to each z-stack layer separately using a rigid motion correction method (NoRMCorre³²).

To segment neuron somas, we used manual ROI labeling for Fish 0 and Fish 1. During the manual annotation process, we labeled two types of ROIs. Firstly, we identified and outlined objects that were approximately the size of a neuron (~9 pixels or 6.6 μm) and had ring-like boundaries. Secondly, for objects of a similar size to neurons, which we tentatively identified as neurons, we analyzed their temporal intensity traces. We then selected those objects whose intensity traces show narrow (<20ms), high amplitude (e.g., >2 \times the standard deviation of the traces), and positive-going spike signals. The annotated ROIs were reviewed by a second person. The percentage of ROIs that the second person disagreed with was ~5% of all the annotated ROIs. The disagreement concentrated on the cases when examining the intensity traces of an object was needed to decide whether to label the object. Within the 30 imaging z-planes of the brain, we identified 25556 neuron ROIs, accounting for ~33% of the total ~78000 neurons estimated in the larval zebrafish brain⁴⁵. It is worth noting this percentage may be a lower limit estimate on the proportion of neurons in the brain that can be extracted using our microscope, as our annotation was performed visually on single z-plane images and raw time series videos, and many more neurons could be annotated in the future with the help of image denoising⁸⁷ and signal unmixing⁸⁸ algorithms. We were deliberately conservative in this paper's analysis, so that we could focus on the question of whether our microscope design crossed the threshold of being able to image neural activity distributed throughout a zebrafish brain. In addition, although we used a pan-neuronal promoter to drive voltage indicator expression, there were regions where neurons were sparsely labeled, as noted above.

The extracted ROIs are processed by VolPy's temporal trace extraction pipeline, which is composed of background removal, trace denoising and spike extraction. We used an adaptive threshold for spiking detection in VolPy. After VolPy's pipeline, we further remove the ROIs with low SNR_{VolPy} ($\text{SNR}_{\text{VolPy}} < 4$; $\text{SNR}_{\text{VolPy}}$ was computed for each neural trace by VolPy, with the detailed algorithm in ⁸⁹), the threshold 4 was arbitrarily chosen after

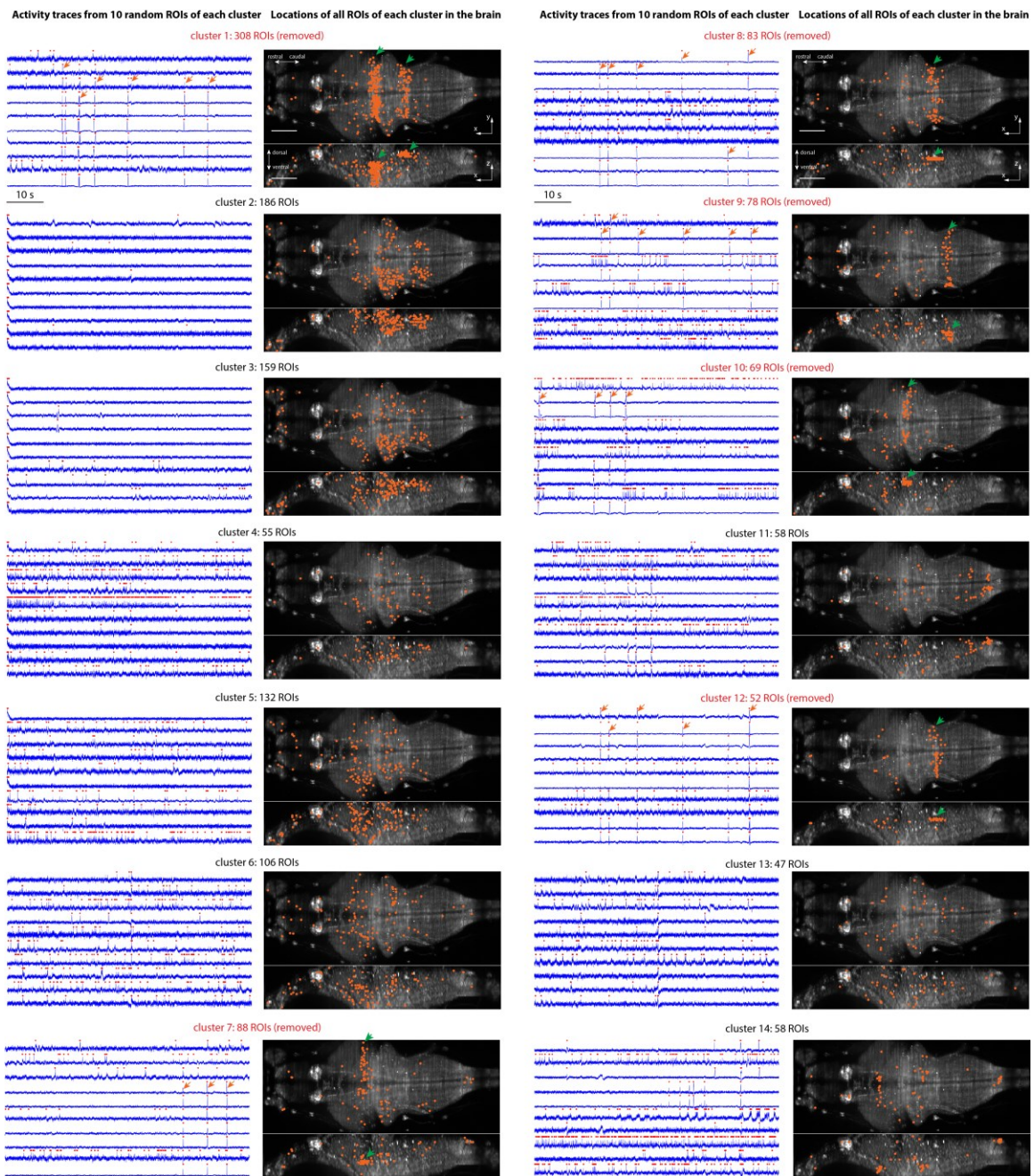
visually inspecting the traces at different SNR_{VolPy}) or ROIs with large overlap. The overlap is determined by calculating the spatial correlation between each ROI and all other ROIs. ROIs with over 0.9 correlation between itself and any of existing ROIs were rejected as they are likely selecting the same cell. For Fish 1, 4111 out of 25556 ROIs are retained for further analysis.

Similar to previous LSM studies^{82,83}, in our experiments, the extracted neural activity traces were also susceptible to varying intensity artifacts caused by the movement of small objects (e.g. blood cells in the vasculature or dust particles in the water) obstructing or scattering the light sheet laser excitation. In our setup, the excitation light sheet enters the larval zebrafish brain from the fish's lateral left side (**Fig. 3-3**, **Fig. 4-1**, **Fig. 4-2**, **Fig. 4-3 green arrows**). When the light sheet encounters a moving object in the sample, it casts a varying stripe shadow from the object's location to the rightmost (relative to the fish) edge of the brain, along the illumination direction of the light sheet (**Fig. 4-3, along the cyan ROIs and along the red ROIs; Fig. 4-6, green arrows**). As the object moves, this shadow changes over time, introducing pulse-like artifacts on the temporal traces of the ROIs (**Fig. 4-3c; Fig. 4-6, orange arrows**).

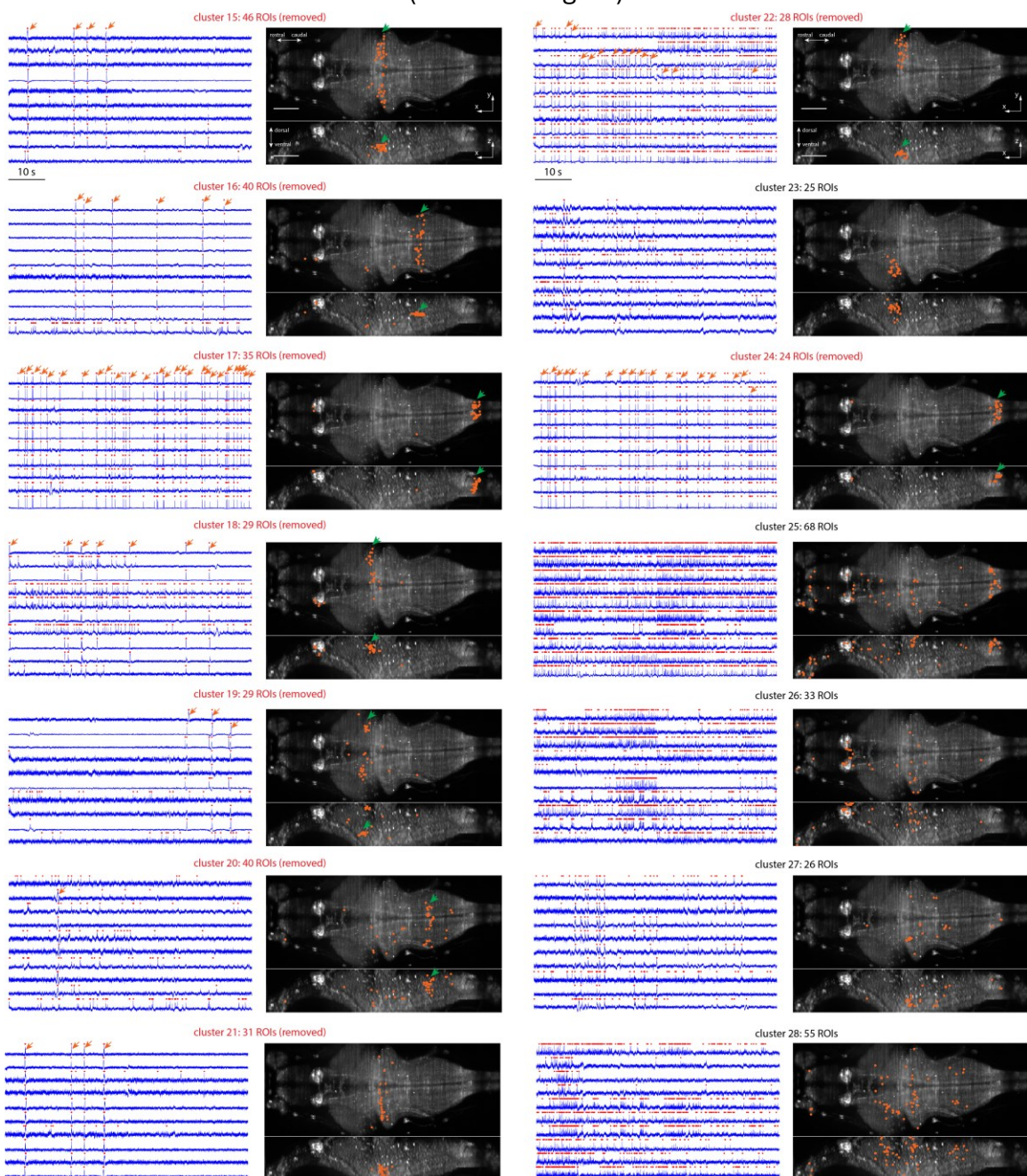
Pulse-like artifacts could, in principle, be mistakenly identified as spikes by the automatic spike detection process. Therefore, any ROIs containing even a single pulse-like artifact should be excluded from further analysis (future analyses could, in theory, enable pulse-like artifacts to be subtracted away, sparing these ROIs for downstream analysis). To identify them, we looked for ROIs with highly correlated pulse-like activities distributed along the fish's medio-lateral axis (**Fig. 4-3b,c**). To facilitate the identification of contaminated ROIs, we clustered ROIs with similar temporal traces. We first applied a 250-ms moving Hanning window to each ROI's spike raster for smoothing and estimating its firing rate. Subsequently, we used the Uniform Manifold Approximation and Projection⁹⁰ (UMAP) algorithm to map the smoothed raster of each ROI onto a 2-dimensional manifold (**Fig. 4-7a**). Following this mapping, we utilized the Density-Based Spatial Clustering of Applications with Noise⁹¹ (DBSCAN) algorithm to separate the ROIs into clusters.

To perform the UMAP-DBSCAN algorithm, we first structured the entire smoothed recording data into an $N \times D$ matrix, where N represented the number of ROIs and D represented the number of temporal samples. This matrix was fed to the UMAP algorithm and transformed into an $N \times 2$ matrix, where each ROI was represented as a point within a 2-dimensional manifold. We then employed the Density-Based Spatial Clustering of Applications with Noise (DBSCAN) algorithm to identify clusters within the 2D representations of ROIs, effectively sorting ROIs with similar temporal spiking patterns into groups. We then visually identified the ROI cluster that was well-separated from the main cluster in the 2D UMAP representation. We then labeled the ROIs of the identified cluster with a unique cluster ID and removed them from the total set of ROIs. The remaining ROIs were then mapped and clustered again using UMAP-DBSCAN for the next iteration. The iteration was continued until the 2D UMAP representation became near Gaussian distributed. The remaining ROIs were assigned to a unique cluster.

Each cluster on the 2-dimensional UMAP manifold contained ROIs with similar spiking activities (**Fig. 4-6; Fig. 4-7a**). Next, we visually inspected each cluster's ROIs' temporal traces and their spatial distributions within the fish (**Fig. 4-6**). Our criteria to identify an artifact cluster were: 1) the temporal traces of the cluster's ROIs exhibited synchronous pulse-like patterns (**Fig. 4-6, orange arrows**); 2) the spatial distribution of the cluster's ROIs had the same spatial features of the artifact stripes or shadows, i.e., the ROIs were concentrated in a region (or regions) that is narrow in the x and z axis ($< 100 \mu\text{m}$) and spanned from a certain location (possibly in the middle of the brain, as there are blood vessels) to the rightmost (relative to the fish) edge of the brain along the y axis (light sheet illumination axis) (**Fig. 4-6, green arrows**). All identified clusters, including those with artifacts, are presented in Figure 4-6. Once we determined a cluster was contaminated by artifact, we removed all the corresponding ROIs, and used the remaining ROIs to repeat the UMAP-DBSCAN process until all the clusters with artifact contamination were removed. In the future, specific algorithms might be developed to identify and decompose these highly correlated pulse-like artifacts as independent components, easily separated from the neural activity, so that artifact-contaminated ROIs can also be used. The remaining ROIs were putatively treated as neurons, sorted into different groups using the same UMAP-DBSCAN algorithm, and await further analysis.



(continued figure)



(continued figure)

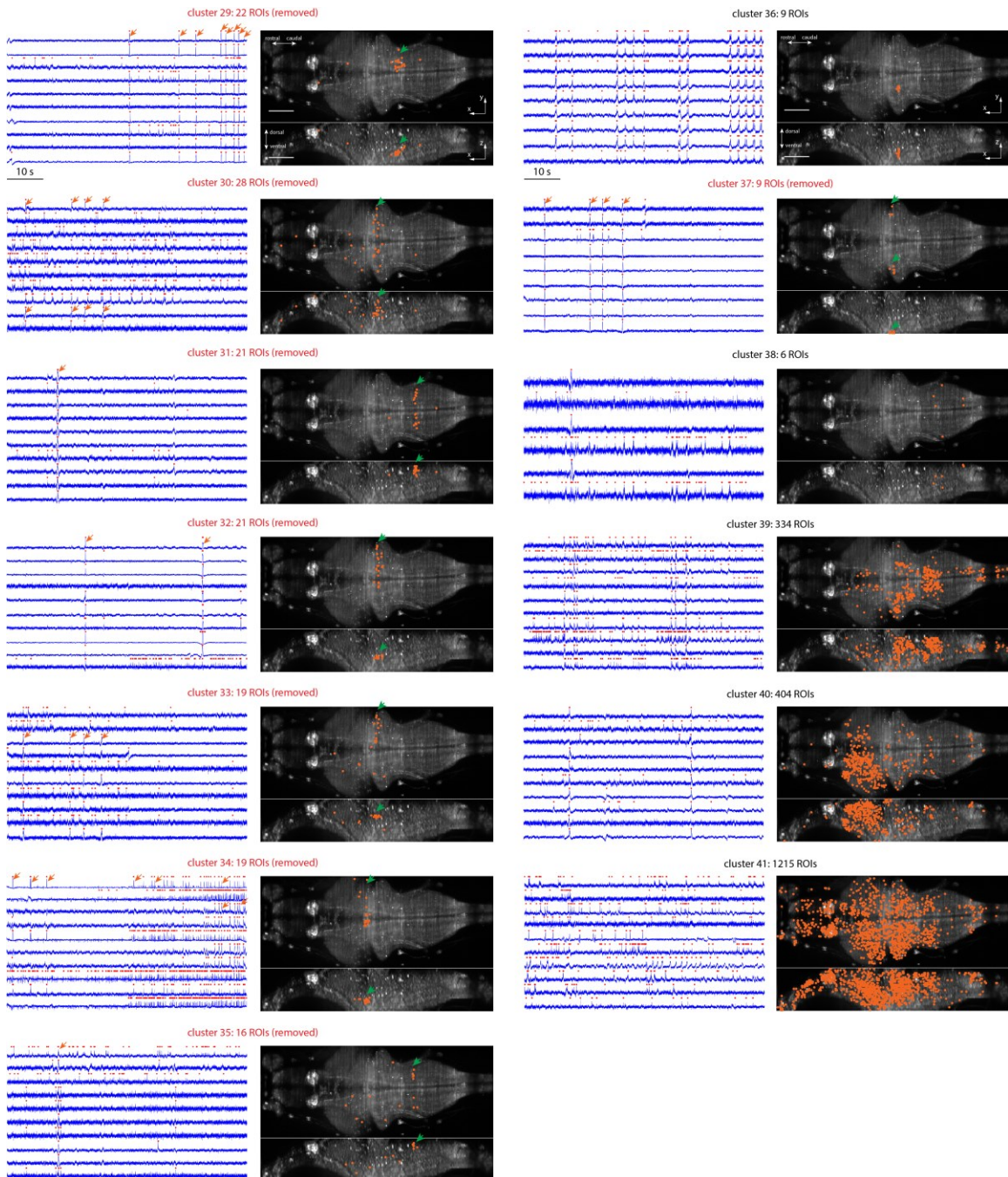


Figure 4-6. Temporal traces and spatial distributions of all ROI clusters grouped using UMAP and DBSCAN for identification and removal of the ROIs contaminated by stripe artifacts. 41 clusters are shown in 41 figure panels. For each panel, on the left, the temporal traces of 10 random selected ROIs in the cluster are plotted in blue, with detected spikes marked as red dots on the temporal traces. Orange arrows point out putative synchronous pulse-like artifacts. The right side of each panel shows the spatial locations of the ROIs (orange dots) in the cluster, overlapped on the axial and lateral maximum intensity

projections of the zebrafish brain. Green arrows point out the spatial distributions of ROI clusters that have the same spatial patterns as the stripe artifacts cast by moving objects in the light-sheet illumination path. The ROI clusters with both synchronous pulse-like artifacts on the temporal traces and spatial distribution patterns resembling the stripe artifacts are removed in subsequent analysis (red figure panel titles). Scale bar: 100 μ m.

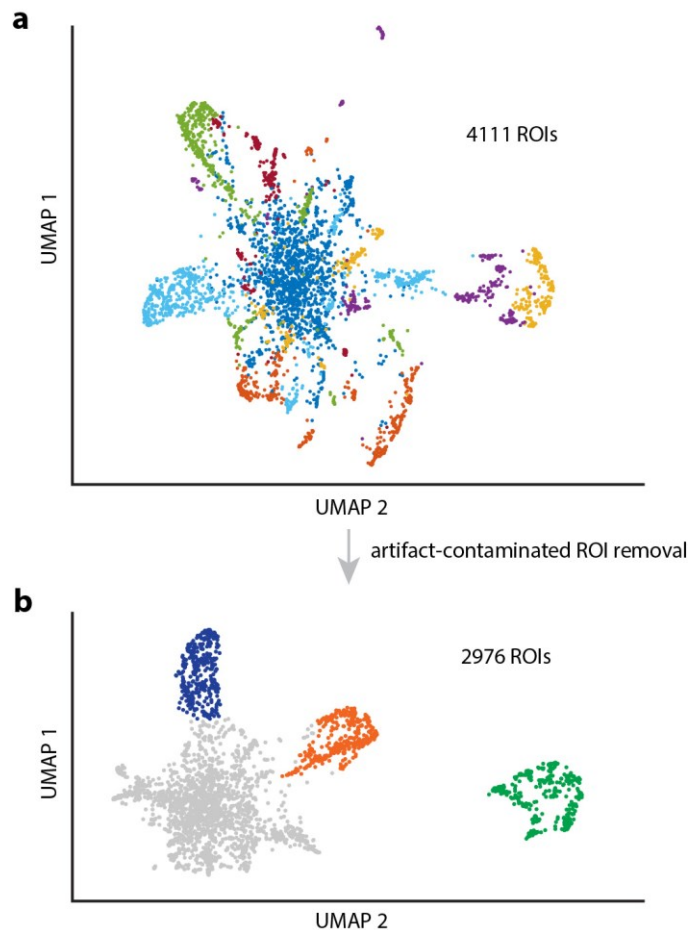


Figure 4-7. 2D UMAP visualizations of ROIs before and after the removal of artifact-contaminated ROIs. (a) 4111 ROIs were mapped into 2D space using the UMAP algorithm based on their temporal traces. Different colors represent different clusters. (b) After identifying and removing the ROIs whose temporal traces are contaminated by the stripe artifacts, 2976 ROIs remained and were considered as putative neurons. The putative neurons were then clustered into four groups (indicated in four colors) for subsequent analysis.

4.3 Analysis of the neural activity

The remaining ROIs after artifact rejection were treated as putative neurons. To delineate distinct cell types within each neuronal group, we employed a similar UMAP-based workflow. However, in order to capture the temporal dynamics of spiking activity at a finer temporal resolution, we applied a 75-ms moving Hanning window for smoothing. Following the UMAP transformation, we performed two types of analyses on the resulting 2D representation of neurons. The first approach involved treating all neurons as part of a continuum on the manifold and sorting them based on their values along one of the UMAP dimensions. This analysis reliably unveiled consistent latency differences among neurons in response to the same stimulus with millisecond-level precision, showcasing the fine temporal dynamics of neurons captured by our camera. In the second approach, we applied either DBSCAN or manual clustering analysis to the 2D representations, further segregating neuronal groups into subgroups that exhibited subtle temporal differences among each other. This method allowed us to uncover different functional nuclei within the circuit that potentially play distinct roles in the same task. For both approaches, we systematically tested a range of parameters for the UMAP transformation and clustering techniques to ensure the robustness of our analysis. To validate our results, we examined the spatial distribution of neurons within individual fish as well as across multiple fish specimens.

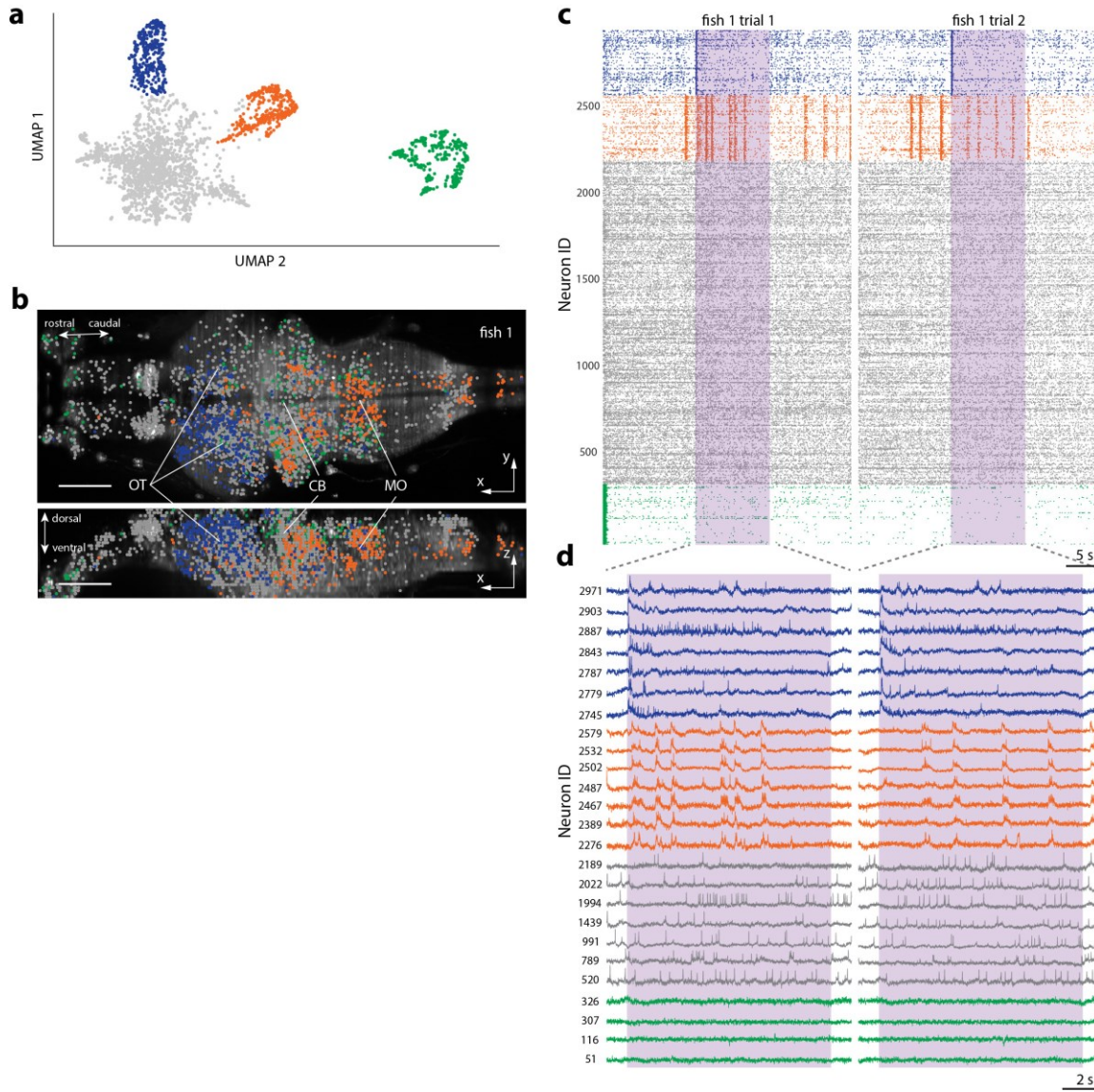


Figure 4-8. The activity of neurons distributed throughout entire zebrafish brains during visual stimulation. (a) Putative spiking activities of all selected neurons in Fish 1 transformed to a 2D dimensional space with UMAP. Neurons in each color group have similar firing patterns. (b) Neurons' spatial locations in Fish 1. Group 1 neurons (blue) are in the optic tectum, Group 2 neurons (orange) are in the hindbrain, Group 3 (gray) and Group 4 (green) neurons are distributed across the brain. OT: optic tectum. CB: cerebellum. MO: medulla oblongata. Scale bar: 100 μ m. (c) Neuron spike raster plots for Fish 1. Four distinct activity patterns are observed in each Fish: Group 1 neurons (blue) have increased activity immediately after UV stimulation onset. Group 2 neurons (orange) have multiple episodes of increased activity throughout the trials. Group 3 neurons (gray) have spontaneous activities throughout the trials. Group 4 neurons (green) have increased activity at the beginning of trial 1, perhaps due to the onset of the light sheet itself. (d) Examples of neurons' putative subthreshold and spiking activity from (c).

In the second approach, DBSCAN isolated a group of neurons (**Fig. 4-8a, blue**) that have increased spiking activities right after the onset of light stimulation in two trials (we named them Group 1 neurons), and another group that exhibited multiple occurrences of burst activity throughout the recordings, uncorrelated with the stimulus (we named them Group 2 neurons, **Fig. 4-8a, orange**). We also found a group of neurons (Group 4) with increased activity at the beginning of trial 1 – potentially due to the initiation of the light sheet for the first time in the experiment, which could trigger a visual response (**Fig. 4-8a, green**). The rest of the neurons did not show distinct temporal characteristics. They were placed in Group 3 (**Fig. 4-8a, gray**), which we suspect to be spontaneous activities throughout the brain. Neurons in different groups exhibited different spatial distributions in the brain. Group 1 neurons were located mostly (~90%) in the optic tectum (**Fig. 4-8b, blue**). Group 2 neurons were mostly (~93%) located in the hindbrain of the fish (**Fig. 4-8b, orange**). Group 3 and Group 4 neurons were scattered across the brain (**Fig. 4-8b, gray and green**). Please note – we do not intend these groups to be considered as fundamental scientific classes of cell type; they are simply meant to represent the kind of pattern our technology can unveil. Such patterns could lead to hypotheses that could be tested with further investigations, e.g. replication in multiple fish, causal perturbation, and varying behavioral and other contexts.

Upon examining the raw ROI traces, in addition to photobleaching (**Fig. 4-9a, black arrows**), we noticed a decay in the overall fluorescence intensity of all ROIs as the 405 nm LED turned on (**Fig. 4-9, orange curve and red curves**). After the LED was turned off, the decreased fluorescence recovered. We hypothesized that this decay and recovery in fluorescence intensity might result from reversible photoswitching of the Positron2 indicator when being exposed to 405-nm light. Previous studies⁹² showed that shining 488-nm blue light could reversibly increase the fluorescence intensity of paQuasAr3, an opsin-based voltage indicator. Positron2 is based on the opsin-FRET design, which means the observed fluorescence from Positron2 is the fluorescence emitted by the fluorophore donor minus the fluorescence absorbed by the opsin acceptor. Therefore, assuming that 405-nm light could reversibly increase the absorbance efficiency of the opsin acceptor of Positron2,

there would be a decay of the fluorescence at the onset of the light stimulus and a recovery of the fluorescence after the light stimulus was turned off, as what we observed in our experiments. Further biophysical studies of voltage indicators in such contexts may be helpful in the future, but here we simply note that the phenomenon was reversible and easily isolated from the true signal. Since this LED-induced fluorescence intensity change affected the entire fish, its impact on neuronal temporal traces could be effectively mitigated during the background removal step of VolPy (**Fig. 4-9**). Despite the LED-induced intensity change, the rise of activity at the onset of LED stimulation was visible in Group 1 neurons' raw traces and the VolPy-extracted traces (**Fig. 4-9a,b, orange arrows**). In contrast, non-Group 1 neurons did not exhibit this sudden increase of activity following the onset of the light stimulus (**Fig. 4-9a,b, green arrows**).

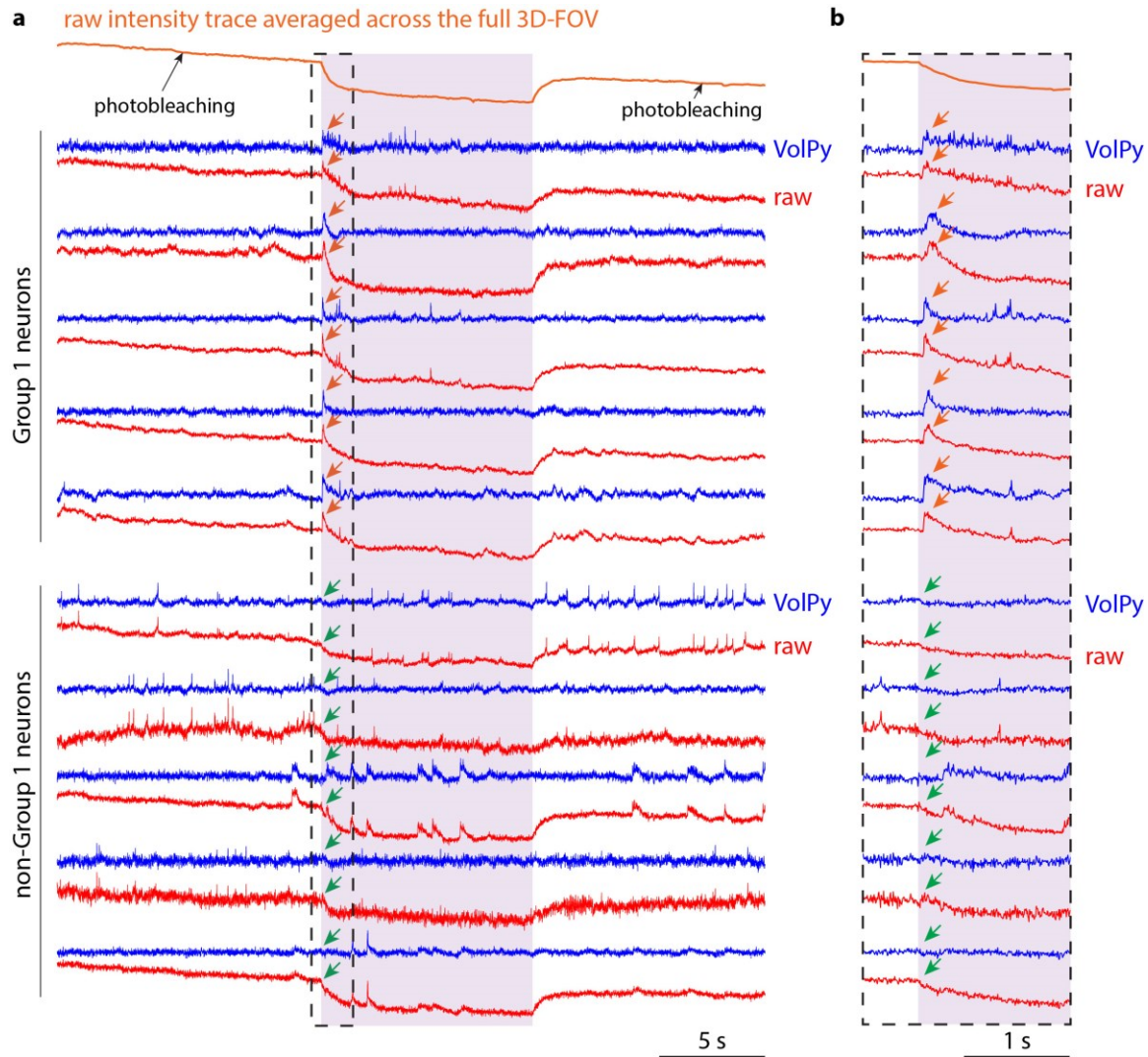


Figure 4-9. Photoswitching effects in VolPy-extracted temporal traces, and raw temporal traces, of neurons in Group 1 (i.e., neurons that have increased activity in response to the onset of the light stimulus) and neurons not in Group 1. (a) Comparison of the VolPy (blue) and raw (red) traces of neurons. Purple color indicates the period of light stimulus. Due to photoswitching effects of the voltage indicators, the fluorescence intensity of the whole zebrafish brain decayed upon the onset of the light stimulus, and recovered after the light stimulus was turned off (top of the panel, orange curve). For Group 1 neurons, following the light stimulus onset, increased activity (orange arrows) can be observed in both the raw temporal traces and the VolPy-extracted temporal traces. Other neurons have photoswitching induced fluorescent changes in their raw traces at the onset of the light stimulus, but do not show increased activity (green arrows). (b) Enlarged view of the dashed box in (a). For Group 1 neurons, a time delay can be observed between the onset of the light stimulus and their increased activity (orange arrows).

We examined the temporal dynamics of Group 1 (**Fig. 4-10a**) neurons in response to the onset of LED stimulation. We first smoothed each cell's spike raster with a 100-ms Hanning window to estimate its spiking rate. We then determined the peak firing rate of each Group 1 neuron and its timing relative to the LED onset, which we called the latency. Next, we ordered the cells by their mean latencies, averaged across the two trials, with smaller IDs indicating earlier timing of the respective neuron's peak activity. The same ordering persisted across the two trials (confirmed by correlation analysis of the cells' mean latencies across two trials, **Fig. 4-10b**), revealing a consistent temporal sequence spanning approximately 200 ms in response to the onset of the light stimulus (**Fig. 4-10c**).

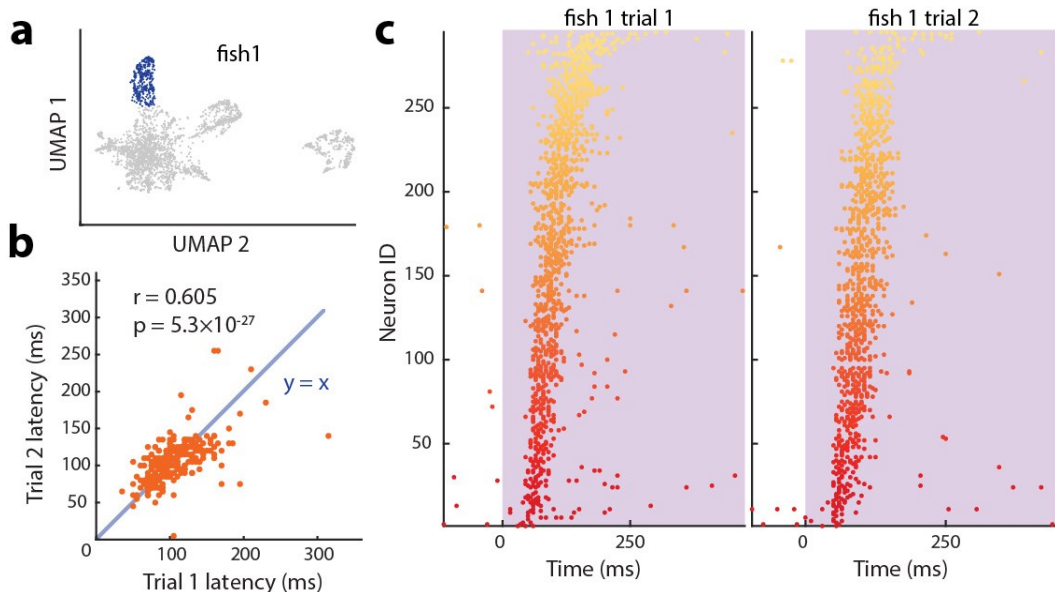


Figure 4-10. Neurons firing at different times in stimulus-evoked sequences. (a-b) Group 1 neurons' peak spiking rate latencies for trial 1, measured relative to UV onset, have a positive correlation with those of trial 2. (c) The sequential order of Group 1 neurons' peak rate in trial 1 is repeated in trial 2. Neurons IDs are sorted based on their peak spiking rate latencies averaged across trials 1 and 2.

Curiously, the temporal sequence of the neurons' activities corresponded to distinct places within the brain. We averaged each neuron's latency from the two trials, into a mean latency measurement. Most of the neurons (~90%) in Group 1 were located on the left half of the optic tectum (**Fig. 4-11a**), as the light stimulation occurred on the right side of the

fish. We observed a strong dorsal-ventral correlation with the cells' mean latency (**Fig. 4-11d**). Neurons that fired early were located closer to the ventral side of the brain, compared to neurons that fired later in the sequence. Thus, whole-brain voltage imaging can be used to create novel hypotheses, in this case, a mapping of time onto space. How do these across-brain voltage data compare to known anatomical and physiological data? In a recent review of discoveries based on classical techniques, Isa et al.⁹³ synthesized an anatomical map of the tectum along with visual processing pathways for various stimuli, including small and large objects, and dimming. We note that this study did not explicitly isolate UV light responses; recent studies on multicolor visual circuits^{94,95}, reviewed in ⁸⁵, showcased the activation of optic-tectum-wide neuronal populations for both visible and UV stimuli using calcium imaging. The observed similarities between activation maps between UV and visible light suggest that UV-processing circuits might follow the (better described) organizational principles of visible light ones. One such principle is that visual input from one retina activates the contralateral optic tectum. Indeed, in our experiment, light was given from the right side of the zebrafish larva, and we observed activity in the left optic tectum. A second principle is the optic tectum's multilayered organization, with the first layer being the most ventral (and distal from the spinal cord), followed by successive layers, each progressively more dorsal (and closer to the spinal cord). Retinal ganglion cell axons have synapses with neurons in more ventral layers. Those neurons of the first tectal layer have neuronal connections with neurons in more dorsal optic tectum layers, and brain regions outside the tectum⁹³. In Figure 4-10 and Figure 4-11, we focus on the first 250 ms (approximately the time over which calcium imaging would have been unable to distinguish) after the onset of the light stimulus. This allowed us to identify neurons (**Fig. 4-11a**, red color, **Fig. 4-11e**, the region we labeled as L1) that fire immediately (<50 ms) after the onset of the light stimulus. These neurons are located in the ventral layer of the optic tectum. Their location and activation timing allowed us to hypothesize that those neurons might receive direct input from the retina. Based on what is known about the organization of the multilayer optic tectum, we postulate that the neurons firing in subsequent layers (**Fig. 4-11e**, L2, cyan arrow), may have received input from the L1 neurons through direct (synaptic) or indirect (involving multiple steps in a neuronal activation chain) neuronal connections. In summary, we observed a sequential activation

of neurons, starting from the ventral layers (known to receive direct retinal input), and progressing to more dorsal layers (probably through synaptic connections). While the purpose of our current experiment was not to do a full scientific study, but rather to show the kind of hypotheses that one could generate with our new technology, such hypotheses could be validated by registering our data to zebrafish brain atlases^{96,97} or through downstream experiments using techniques such as optogenetics, synaptic tracing, and ablations, were this to be a full scientific study.

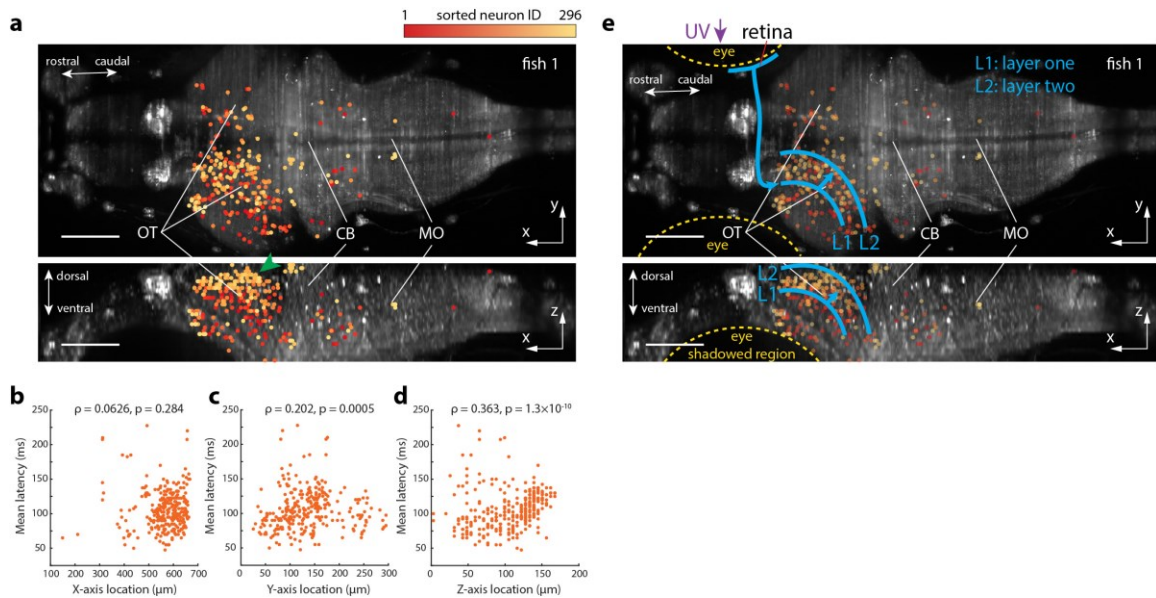


Figure 4-11. Spatial mapping of neurons firing at different times in stimulus-evoked sequences. (a) Group 1 neurons' spatial positions. Most Group 1 neurons are located on the lateral-left side of the optic tectum. OT: optic tectum. CB: cerebellum. MO: medulla oblongata. Scale bar: 100 μm . (b-d) Neurons' peak spiking rate latencies with respect to their positions along (b) anterior-posterior, (c) lateral/left-right, and (d) dorsal-ventral axes. Earlier firing neurons are located more lateral and more ventral compared to later firing neurons. (e) A neural circuitry hypothesis from the observations of this experiment, highlighting the utility of our tool in hypothesis generation.

Next, we examined the temporal characteristics of Group 2 neurons, which exhibited multiple bursts that occurred across the population of neurons (Fig. 4-12). To identify a burst event, we first smoothed each neuron's spike raster with a 70-ms moving Hanning window to estimate its spiking rate. The population spiking rate was then

determined by averaging the smoothed raster across all Group 2 neurons (**Fig. 4-12a**). A burst was detected when the spiking rate increased above a threshold, set at five times that of the average spiking rate across two trials (**Fig. 4-12a**). 11 burst events were identified in trial 1 and 7 events in trial 2, across all neurons analyzed.

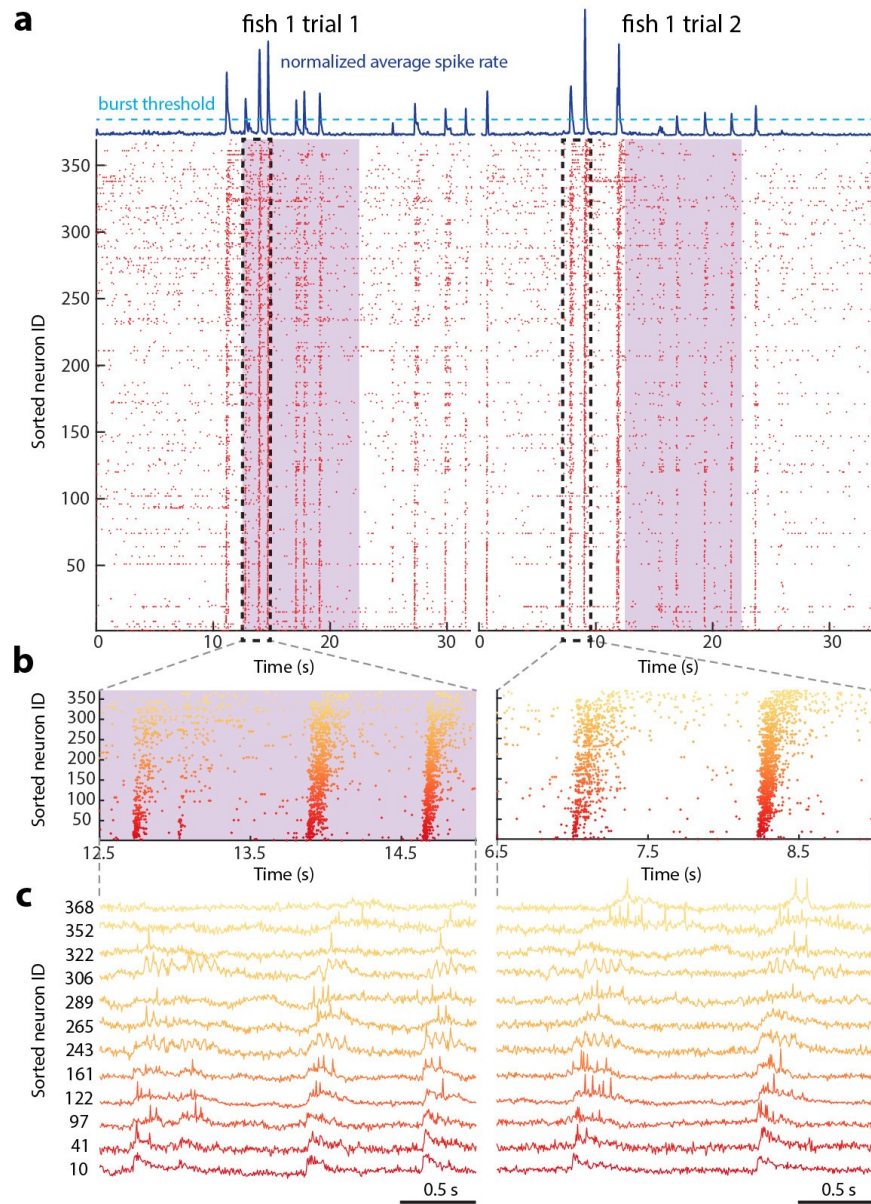


Figure 4-12. Different times of burst sequence activity across the zebrafish brain. (a) Raster plot showing nearly synchronous bursting in Group 2 neurons during the light stimulation experiments in Fish 1. These neurons correspond to the orange group in Figure 4-8a's UMAP plot. The blue curve on the top of the raster plot shows the normalized

(normalized to 0-1) average spike rate of this neuron group, with each point on the curve indicating the average of all the neuron's spike rates at that time point. We define a burst as the period when the average spike rate is larger than 5 times the mean value of the blue curve. This threshold is indicated as the cyan dashed line. The start of each burst is defined as the first time point in the burst when the average spike rate surpassed the threshold. Neurons are sorted by their mean activation timing in a burst. Left and right display two trials separated by a 20-min dark session in between, with the UV stimulus period indicated in purple. **(b)** Magnified views of the boxed areas in (a), illustrating a consistent sequence of neural activation during bursts. This sequential order is color-coded from deep red to light orange. **(c)** Example raw activity traces from the neurons in (b).

Upon inspection, we noted that bursts were not fully synchronized across neurons, but instead occurred at slightly different times, across the population of neurons involved in bursts. Curious to see if the slight differences in timing were consistent, we investigated whether there was a reliable temporal ordering of Group 2 neurons' activities during bursts. We identified each Group 2 neuron's peak firing rate, and timing thereof, within every burst event. We then ordered the Group 2 neurons based on their peak firing rate timing averaged across all the burst events. Smaller IDs indicate that the respective neuron's peak activity occurred earlier in the burst event. Indeed, neurons that fired earlier in the first burst of a series, fired earlier in later bursts of the series (**Fig. 4-12b, c**) – there was a consistent ordering of firing of neurons, within these nearly, but not-quite, synchronized bursts. We asked whether the temporal features of Group 2 neurons also corresponded to any spatial characteristics, as in the case of light stimulus-evoked activity. We noticed that a specific region in the MO (**Fig. 4-13a**, white dashed box) contained many neurons that fired early during burst events, and were concentrated within a defined volume ($\sim 35 \times 110 \times 40 \mu\text{m}^3$, x by y by z) (**Fig. 4-13a, b, green arrows, Fig. 4-13e green color**). Their activity preceded that of another cluster of neurons located more dorsally in the selected sub-region (**Fig. 4-13a, b, magenta arrows, Fig. 4-13e magenta color**). To quantify this spatiotemporal relationship, we computed the correlation between these neurons' average peak timing across bursts, and their corresponding spatial locations. We found significant correlations between timing and rostral-caudal (x-axis) and dorsal-ventral (z-axis) dimensions (**Fig. 4-13b, d**).

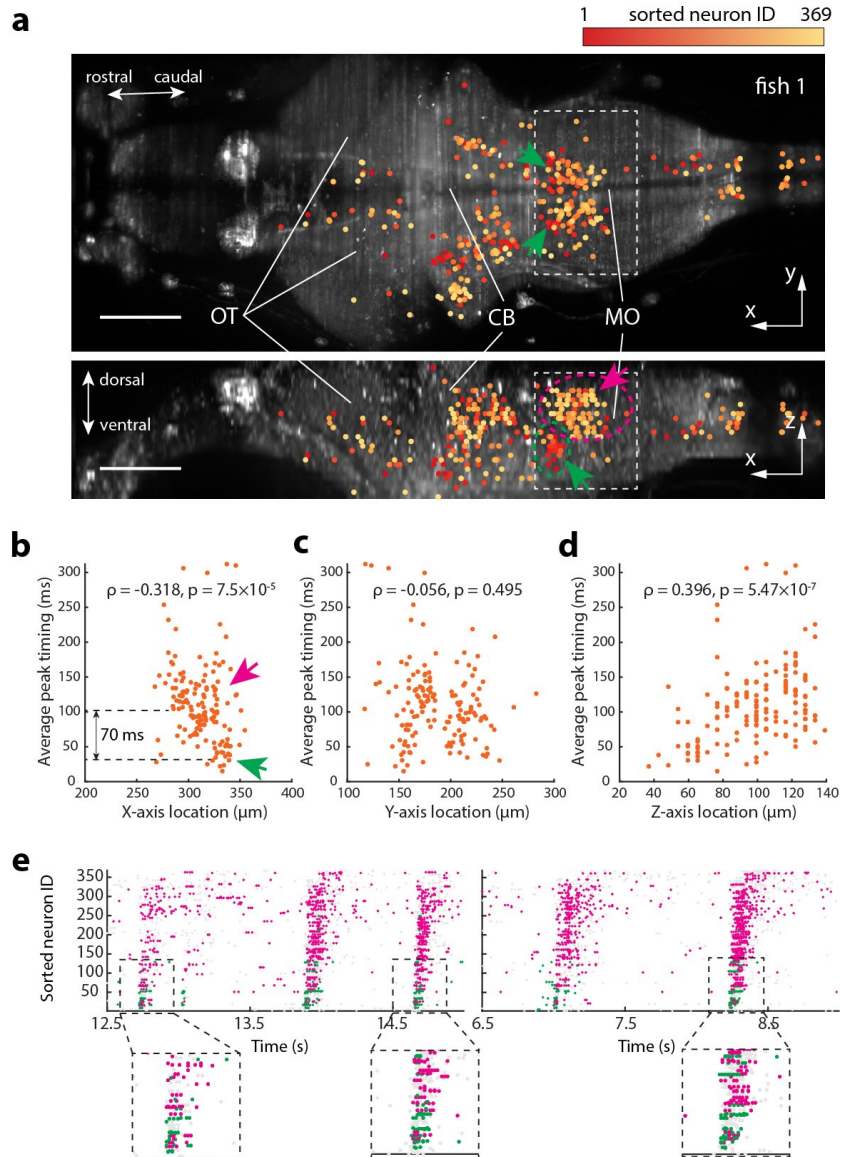


Figure 4-13. Spatial mapping of the timing of burst sequence activity across the zebrafish brain. (a) 3D locations of neurons in Group 2 superimposed on the dorsal (top) and lateral (bottom) brain views (MIPs) of Fish 1. The neuron firing sequence is color-coded by their neuron IDs, which are sorted based on their activity timing. The green arrow highlights a cluster of early firing neurons. The magenta arrow highlights a cluster of neurons that fired ~ 70 ms after the green arrow-indicated cluster. The correlation between the activation timing and x, y, and z locations of neurons in the dashed white box were analyzed and shown in (b-d). OT: optic tectum. CB: cerebellum. MO: medulla oblongata. Scale bar: 100 μm . (b-d) Scatter plots for Fish 1, correlating the average peak timing and the x, y, and z locations of the neurons enclosed in the white dashed line box. Spearman's rank correlation coefficients and p-values are included. (e) Sorted raster plot of the burst neural activity during the visual stimulation experiments in Fish1. Different colors are used

to indicate the “early-firing” neuron cluster (green arrows in (a)), and the “late-firing” neuron cluster (magenta arrow in (a)) in the white dashed box in (a). The spike raster of the neurons outside the white dashed box is labeled using a light gray color. Three views are magnified.

Through visual inspection, the spatial position of the earliest-firing neurons (**Fig. 4-13a**, green arrow) coincided with a specific neuronal cluster, potentially in rhombomere 5, close to or potentially the same as the cluster of MiD2 reticulospinal neurons⁸⁰. By recording their activity using calcium imaging in fictively swimming larval zebrafish, Chen et. al.⁸⁰ found that the MiD2 neurons are involved in bilateral swimming, with no selectivity for turning actions. However, that study could not determine the order of activation across different neuron populations in these motor pathways, due to the limited speed of calcium indicators and the slow optical sampling rate used (2 to 3 Hz). Our study lacks fictive swimming recordings to establish any behavioral correlates of the neuronal activities we observed, so we cannot make any conclusions regarding the precise identity of the neurons we have pinpointed. But if this were a full scientific study, optogenetics, anatomical tracing, and other kinds of experiments could be used to pinpoint the identity and causal role of the neurons observed. For the purposes of the current study, we simply highlight the ability of our technology to reveal the precisely timed operation of this cluster of neurons, relevant to other local circuitries.

Chapter 5

Discussion and future work

5.1 Conclusion and discussion

We here present a microscope optimized for the imaging of the voltage of individual neurons distributed throughout the entire larval zebrafish brain. The microscope utilizes an optimized form of remote refocusing, in conjunction with an optimized optical train and an optimized camera strategy, so as to enable the imaging of the entire volume of the larval zebrafish brain, at 200 volumes per second, with single-cell resolution, with sufficient SNR to image action potentials in GEVI-expressing neurons distributed throughout the brain. Our technique was able to reveal sequences of neurons that fire in consistent order, over timescales of milliseconds, both in response to visual stimuli and in stimulus-independent bursts, and to map those sequences onto defined locations distributed throughout regions in the larval zebrafish brain, revealing novel time-space mappings. Thus, our microscope can reveal novel patterns that would be too fast, yet too distributed, to detect with prior technologies. Combined with other stimuli, and fictive behavior paradigms (and, potentially in the future, freely moving behavior paradigms), our technique could be immediately applied to confront a variety of systems neuroscience questions (some that immediately come to mind include the mechanisms of “up” and “down” states during sleep, and excitatory-inhibitory balance in the brain⁹⁸). Using red-shifted dyes¹³ and blue-shifted

opsins, perhaps in conjunction with holographic optogenetic control⁹⁹, our technique could in principle, support the integration of whole-brain voltage imaging and optogenetics, enabling all-optical electrophysiology at the whole-brain scale.

Our microscope represents a significant advancement of in vivo imaging techniques in terms of recorded neuron numbers and sampling rates (**Fig. 5-1**). When evaluated by the overall recording throughput, defined as the product of the number of recorded neurons and the sampling frequency, our technique outperforms existing in vivo imaging techniques by ~2.5 times (compared to light beads microscopy³⁰), and existing in vivo voltage imaging techniques by ~50 times (compared to SpikeyGi2+SMURF+DeepVID²¹).

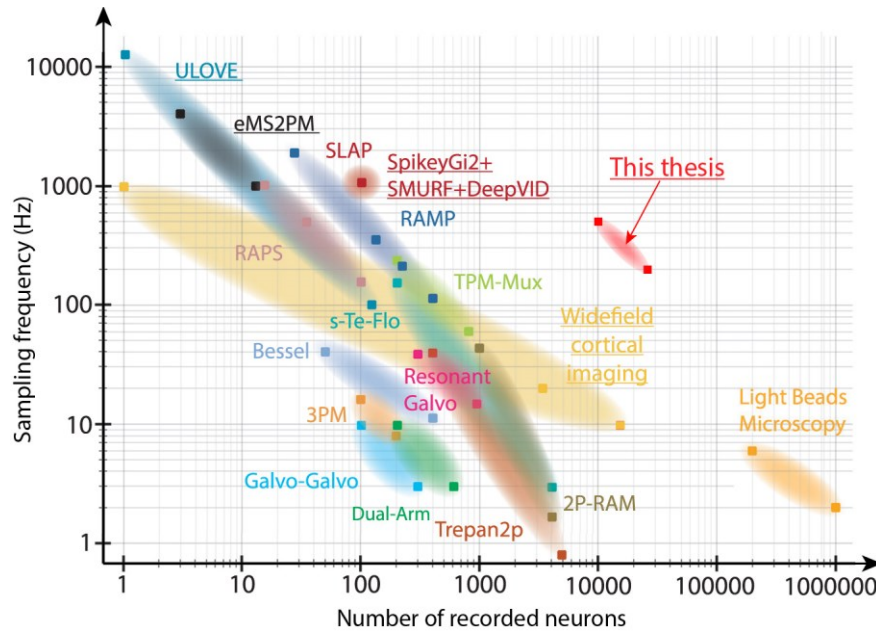


Figure 5-1. Comparison of this work and existing in vivo imaging techniques in terms of number of neurons and recording speed onto a 2D space (number of imaged neurons vs. sampling rate). Square markers represent published data. Clouds represent hypothetical interpolation between the reported data points. Underlined labels refer to techniques that were specifically used for voltage imaging. Adapted from ¹⁰⁰.

Our microscope shows that we are crossing the threshold where imaging of voltage of neurons distributed across an entire brain is possible, but there is much room for improvement in essentially every aspect of the technology. Improved GEVIs, with better

brightness, SNR, and kinetics, are always welcome. Higher spatial and temporal resolutions, and better SNRs, of the optics, would always be desirable. Currently the imaging rate of our technique is limited by the camera's pixel rate. However, higher imaging rates, up to >1000 hertz, could be achieved in principle with our current setup, to image a 3D-FOV smaller than the entire zebrafish brain. In practice, the 200-Hz whole-brain voltage imaging shown here, and kilohertz regional imaging, could be performed in the same experiment at different times as part of an overall strategy to tackle a biological problem across scales and resolutions. As faster, more sensitive image sensors are developed, we expect the speed bottleneck to be alleviated, and whole-brain voltage imaging with temporal resolutions down to sub-milliseconds will almost certainly become possible. An identical second remote scanning module, including a remote objective lens, quarter wave plate, and piezo-driven remote mirror, could be added to the current setup to double the light efficiency. An additional light sheet illuminating from the front of the fish could be added to excite the brain volume between the fish's eyes, which is currently shadowed by the physical eye mask from the laterally illuminated light sheet. To reduce light scattering in the tissue, GEVIs with long excitation wavelength, or multi-photon light-sheet excitation could be exploited. Post hoc analysis of zebrafish brains via expansion microscopy¹⁰¹, perhaps with barcoded neurons for easy tracing^{102,103}, and with in situ sequencing of gene expression patterns¹⁰⁴, could help link brain structure and molecular composition to emergent dynamics.

The large datasets produced through whole-brain voltage imaging necessitate specialized algorithms and software for efficient processing and analysis. While existing software packages and denoising algorithms, such as VolPy, can be modified for these purposes, there is room for new algorithms to help segment neuron ROIs from densely labeled brain images, as well as for extracting and demixing voltage signals from densely packed neurons. Of course, interpreting whole-brain neural codes through machine learning and simulation, also presents unique opportunities for understanding how entire brains work together to generate emergent dynamics and behavior.

5.2 Future work

In this thesis, we imaged 30 z-planes across 170 μm depth of the larval zebrafish brain, resulting in a z sampling step size of 5.86 μm . This large step size risks missing neurons despite that it is smaller than the average neuron soma diameter (6.62 μm ²⁷) in zebrafish. This is because 1) neuron somas in the zebrafish brain vary in size, some of which can be as small as 3 μm in diameter; 2) neurons laying at the middle between two adjacent z sampling planes are hard to identify in light-sheet images, as only the top and bottom fractions of their soma membranes are sampled, and the sampled membrane fractions can be easily overwhelmed by bright fluorescence from neighboring neurons along the z-axis. To improve our technique to image all neurons in the zebrafish brain, a higher z sampling density is desired. Potential strategies to achieve this include improving the frame rate of the current cameras using an 8-bit mode, implementing a distributed planar imaging setup with more cameras, and utilizing new, faster cameras.

Our current microscope and imaging protocol can allow continuous monitoring of neural voltage in a zebrafish brain at 200 Hz for several minutes. This recording duration is limited by the photobleaching rate of the voltage indicators. To extend the recording duration, we can adopt approaches from various angles. Optically, adding a second remote scanning module at the other side of the polarized beam splitter will double the microscope's light efficiency, thus reducing the necessary excitation intensity. Molecularly, brighter, and more photostable voltage indicators can be employed. For example, changing the dyes for Positron2-Kv from JF525 to JF549 and JF585⁸ will improve photostability by factors of 3.9 and 7.9 respectively, thereby extending the recording duration proportionally.

Like in many previous LSM configurations, we observed “stripe” shaped artifacts in the raw images. These artifact stripes obscured partial cell bodies of some neurons, rendering fragmented neuron contours, and complicating the cell segmentation process. Moreover, some “stripe” artifacts varied over time, causing pulse-like artifacts to the extracted neural temporal traces. Following this thesis, many strategies can be implemented to tackle this stripe artifact problem. First, stripe artifact removal algorithms¹⁰⁵ can detect

and remove stripe artifacts in LSM images post hoc. These algorithms can yield de-striped raw images that improve the efficiency and accuracy of cell segmentation. In addition, the stripe artifacts can be reduced or eliminated during imaging by pivoting or diffusing the light-sheet in the illumination plane⁸². A high-speed galvo mirror¹⁰⁶ or an acoustic optical deflector¹⁰⁷ can pivot the light-sheet and the stripe artifacts in the illumination plane. If the stripe artifacts are pivoted across a sufficiently large angle during an exposure, the stripe artifacts will be efficiently "averaged out" in the acquired image. To match the 40-μs exposure time in our experiments, a minimum 25 kHz pivoting rate will be required. To ensure that in each frame, the stripe artifacts are consistently averaged out in the same manner, the pivoting should synchronize with the camera exposure. Alternatively, the pivoting frequency should be carefully adjusted to make sure that each exposure captures precisely an integer number of pivoting cycles. Linearly diffusing the light-sheet in the illumination plane can also suppress the stripe artifacts⁸³. However, speckle patterns will form in the illumination plane due to the interference of the diffused coherent light sheet. To get rid of the speckle patterns, the linear diffuser can be vibrated along the diffusion axis to average out the speckle patterns during an image exposure. The short exposure time in our experiments requires a high vibration rate, which can be offered by a high resonant frequency piezo actuator. More drastically, as neural voltage changes the fluorescence lifetime of various voltage indicators (e.g., Voltron2 and Positron2), neural voltage activity can be measured through the indicators' lifetime, a parameter that is independent of their fluorescence intensity. The strategy of voltage imaging based on fluorescence lifetime inherently eliminates temporal artifacts associated with intensity fluctuations, including the stripe artifacts observed in our experiments. Recently, wide-field electro-optic fluorescence lifetime imaging (EO-FLIM)¹⁰⁸ has been demonstrated to image neural voltage in adult *Drosophila* brains at 1 kHz. Incorporating the EO-FLIM technique with our microscope would not only solve the stripe artifact problem, but also open the possibility of imaging the whole-brain voltage activity in freely behaving animals, such as freely swimming larval zebrafish.

To segment the densely packed neuron somas in the light-sheet images, we employed a manual segmentation process, where we draw ROIs according to the sizes, shapes, and temporal traces of the spatial structures in the raw images. This manual process

allowed us to segment >25,000 ROIs in a zebrafish brain. However, manual segmentation requires significant labor and is time consuming. It also carries the risks of introducing the experimenters' biases and overlooking neurons with low visual contrast. Therefore, automatic segmentation algorithms are desired. While many cell segmentation algorithms exist (such as the Mask R-CNN segmentation network in VolPy⁸⁴, VoluSeg¹⁰⁹, Cellpose^{110,111}) and are optimized for existing microscopy images, our new microscope generates a unique type of imagery that necessitates the modification and fine-tuning of these segmentation algorithms. Specifically, the neuron somas in our images are densely packed, membrane labeled, and sampled with large pixels (~1/10 of the soma size). In principle, a cell segmentation neural network can be trained on our images using manually annotated ROIs. This can be done by either retraining the Cellpose's neural network or developing a new neural network from scratch. Moreover, non-deep learning image processing algorithms¹¹² and temporal correlation analysis¹⁰⁹ may be used in combination with deep learning algorithms to enhance the accuracy and efficiency of the segmentation process.

Chapter 6

Other works and attempts

6.1 Miniaturized extended field-of-view light-field microscopy for 3-D imaging of freely behaving mouse brains

In pursuit of monitoring rapid neural activity across large brain volumes, previously I have co-developed a novel imaging technique called Sparse Decomposition Light Field Microscopy (SDLFM)³³. This method addresses the decreased reconstruction accuracy for densely labeled samples in traditional light-field microscopy, providing a high spatiotemporal resolution for volumetric neural activity imaging. SDLFM is particularly adept at examining the transient neural dynamics on a large scale. We have successfully demonstrated the efficacy of SDLFM by imaging the larval zebrafish brain and capturing the cellular activity from thousands of neurons at a rate of 50 volumes per second. Our current hardware is capable to scan a brain volume encompassing up to 1000 μm in lateral diameter and 400 μm in thickness at speeds up to 100 Hz. Consequently, this can enable interrogating the activity and function changes within neural circuits spanning vast spatial dimensions.

Due to their large size and weight, benchtop microscopes often impose constraints on the motion and behaviors of the studies animals, hindering the investigation of complex

behaviors such as social interactions and brain functions in their natural states. Our current SDLFM uses an eXtended field-of-view Light-Field Microscope (XLFM)³⁴ as the hardware. The XLFM setup is approximately 1 m long, 0.7 m wide, and 0.5 m high, and weighs tens of kilograms. During imaging experiments, the samples need to be mounted on a 3-D translation stage and imaged at a fixed location under the objective lens.

To apply SDLFM for mapping the neural activity in mice while they are performing freely behaving tasks, I have started developing a miniaturized light-field microscope (miniXLFM) that can be mounted on a mouse's head (**Fig. 6-1a, b**). The constructed miniXLFM measures approximately 3 cm in length and weighs a few grams. It utilizes a gradient refractive index lens (GRIN lens, NA=0.5) as the detection lens. When tested by imaging fluorescence beads in agarose, the miniXLFM can cover a volume with a 500 μm lateral diameter and 500 μm axial thickness, achieving approximately 5 μm lateral and 15 μm axial resolution (**Fig. 6-1c**). Next, we plan to install the miniXLFM in freely behaving mice (e.g., Ts65dn mice) to study the *in vivo* fast neural processes of 3-D distributed neuron populations. With advanced high-speed image sensors and improved GEVIs, the miniXLFM can potentially be used to record the neural voltage activity from a brain volume in freely behaving mice.

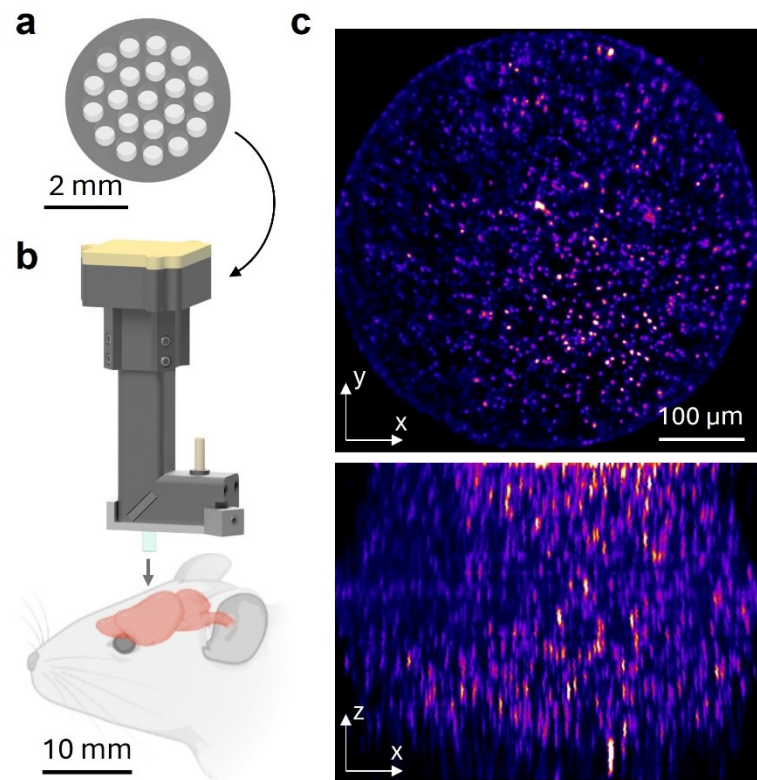


Figure 6-1. MiniXLFM for in vivo neural activity imaging in unrestrained, freely behaving mice. (a) Miniaturized micro-lens array. (b) MiniXLFM assembly designed for implementation in mice. (c) Maximum intensity projections (MIPs) of the reconstructed 3-D image of a fluorescent bead sample acquired using the customized miniXLFM, showing the field of view and resolution capabilities of the scope.

6.2 Enhancing the FRET efficiency of fluorescent activity indicators using spatial clustering

This strategy was conceived together with Yong Qian.

A large library of GEVIs^{8,14,74,113,114}, including the Positron2 used in this thesis, require Förster resonance energy transfer (FRET) to report membrane voltage activity. These GEVIs usually contain two linked domains: a transmembrane rhodopsin domain that senses membrane voltage, and a bright fluorescent domain that emits photons. The two domains interact via FRET to sense and report voltage activity: membrane voltage modifies the absorption ability of the rhodopsin, which changes the FRET efficiency and how much light from the fluorescent domain is quenched by the rhodopsin, leading to brightness changes of the GEVI molecule.

The FRET efficiency in rhodopsin-FRET GEVIs can significantly affect the indicators' sensitivity and signal-to-noise ratio. We can derive their relationship through simple mathematical derivation. Here we let F be the GEVI brightness, α be the absorption ability of the rhodopsin, E be the FRET efficiency, and V to be the membrane potential. According to the FRET theories, $E = 1/(1 + C/\alpha)$, where C is a constant. The GEVI fluorescence $F = F_0(1 - E)$. Then the GEVI voltage sensitivity, defined as $\frac{dF/F}{dV}$, is

$$\frac{dF}{F \cdot dV} = -\frac{d\alpha}{\alpha \cdot dV} \cdot E.$$

$\frac{d\alpha}{\alpha \cdot dV}$ is the rhodopsin's absorption sensitivity to membrane voltage. Therefore, rhodopsin-FRET GEVIs' sensitivity increases proportionally to the FRET efficiency. On the other hand, higher FRET efficiency causes stronger quenching and lower GEVI brightness, increasing the shot noise in imaging. Taking this into account, the GEVI's signal-to-noise ratio (SNR), defined as their voltage sensitivity divided by their shot noise, is

$$\frac{\frac{dF}{F \cdot dV}}{\sqrt{F}} = -\frac{d\alpha}{\alpha \cdot dV} \cdot \sqrt{F_0} \cdot E(1 - E)^{1/2}.$$

This SNR maximizes when the FRET efficiency $E = 0.67$. The same results can also be found in¹¹⁵.

At present, most reported rhodopsin-FRET GEVIs that work *in vivo* have a FRET efficiency below 0.67^{114,116}. To enhance the FRET efficiency, we proposed a strategy to cluster FRET-based GEVIs so that their donors and acceptors can be shared with other GEVIs in the cluster (**Fig. 6-2a**). There are two possible configurations. First, multiple

acceptors can be attached around a fluorescent donor to multiply the donor's FRET paths (**Fig. 6-2a middle**). Second, multiple monomer FRET indicators can be closely clustered to enable FRET cross different monomers (**Fig. 6-2a right**). We calculated the FRET efficiency, voltage sensitivity, and SNR improvements. For simplicity, we assumed that the clustering molecules are sufficiently close to each other so that a donor can interact with all the acceptors in the cluster with the same FRET efficiency E_1 . Then, the overall FRET efficiency with n acceptors for the donor is

$$E_n = \frac{nE_1}{(n-1)E_1+1}.$$

Using E_n , the sensitivity and SNR of clustered indicators can be calculated, as shown in **Fig. 6-2b, c**. According to **Fig. 6-2c**, this clustering strategy works particularly well for monomer GEVIs that have a low FRET efficiency (E_1). For instance, a trimmer cluster of indicators with a ~20% initial FRET efficiency can almost double their SNR. We expect this strategy can serve as a general approach to further improving the SNR of existing FRET indicators, especially those with low FRET efficiency, such as far-red and infrared GEVIs.

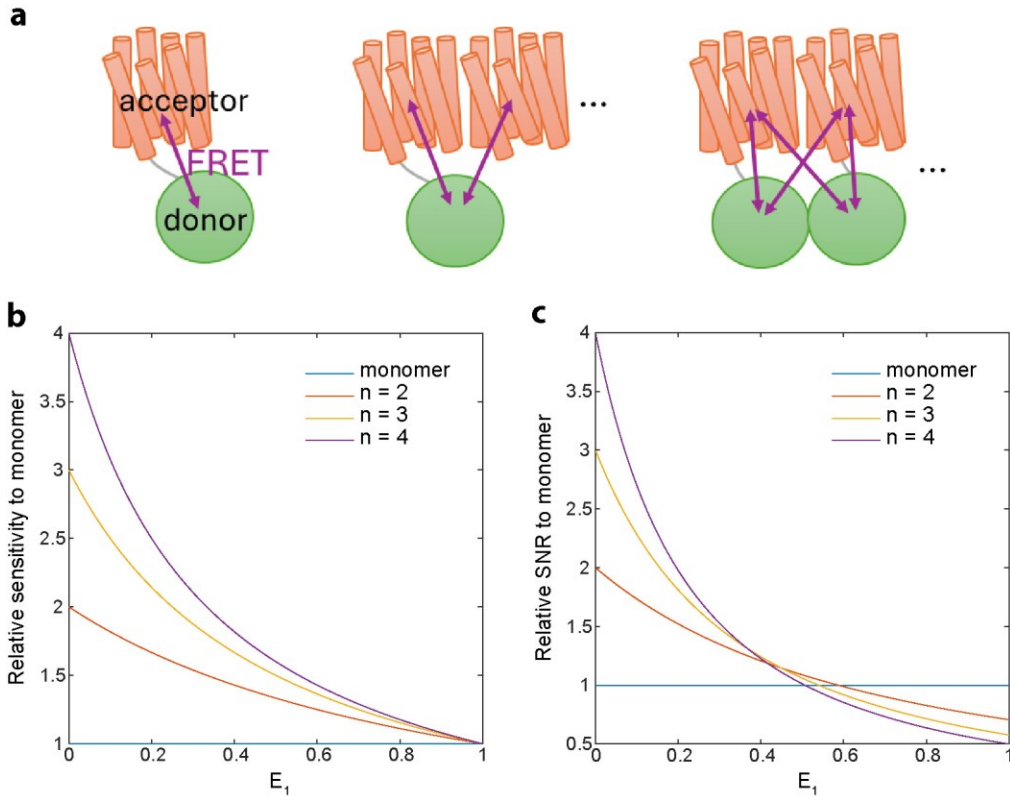


Figure 6-2. Improving the sensitivity and SNR of FRET-based GEVs through clustering. (a) Two configurations of clustering. A donor (green) can have FRET processes (purple) with multiple acceptors (orange) in a cluster. (b) The relative sensitivity of clustered GEVs compared to that of GEVI monomers. (c) The relative SNR of clustered GEVs compared to that of GEVI monomers.

References

1. Tiesinga, P., Fellous, J.-M. & Sejnowski, T. J. Regulation of spike timing in visual cortical circuits. *Nat. Rev. Neurosci.* **9**, 97–107 (2008).
2. Uchida, N., Poo, C. & Haddad, R. Coding and transformations in the olfactory system. *Annu. Rev. Neurosci.* **37**, 363–385 (2014).
3. Wang, X. Neural coding strategies in auditory cortex. *Hear. Res.* **229**, 81–93 (2007).
4. Panzeri, S., Petersen, R. S., Schultz, S. R., Lebedev, M. & Diamond, M. E. The role of spike timing in the coding of stimulus location in rat somatosensory cortex. *Neuron* **29**, 769–777 (2001).
5. Budick, S. A. & O’Malley, D. M. Locomotor repertoire of the larval zebrafish: swimming, turning and prey capture. *J. Exp. Biol.* **203**, 2565–2579 (2000).
6. Hong, G. & Lieber, C. M. Novel electrode technologies for neural recordings. *Nat. Rev. Neurosci.* **20**, 330–345 (2019).
7. Yang, H. H. & St-Pierre, F. Genetically encoded voltage indicators: Opportunities and challenges. *J. Neurosci.* **36**, 9977–9989 (2016).
8. Abdelfattah, A. S. *et al.* Bright and photostable chemogenetic indicators for extended in vivo voltage imaging. *Science* **365**, 699–704 (2019).
9. Grimm, J. B. *et al.* A general method to improve fluorophores for live-cell and single-molecule microscopy. *Nat. Methods* **12**, 244–50, 3 p following 250 (2015).
10. Voltron and positron. *Janelia Research Campus* <https://www.janelia.org/open-science/voltron-and-positron>.
11. Villette, V. *et al.* Ultrafast two-photon imaging of a high-gain voltage indicator in awake behaving mice. *Cell* **179**, 1590–1608.e23 (2019).
12. Tian, H. *et al.* Video-based pooled screening yields improved far-red genetically encoded voltage indicators. *Nat. Methods* **20**, 1082–1094 (2023).

13. Piatkevich, K. D. *et al.* A robotic multidimensional directed evolution approach applied to fluorescent voltage reporters. *Nat. Chem. Biol.* **14**, 352–360 (2018).
14. Kannan, M. *et al.* Dual-polarity voltage imaging of the concurrent dynamics of multiple neuron types. *Science* **378**, eabm8797 (2022).
15. Azimi Hashemi, N. *et al.* Rhodopsin-based voltage imaging tools for use in muscles and neurons of *Caenorhabditis elegans*. *Proc. Natl. Acad. Sci. U. S. A.* **116**, 17051–17060 (2019).
16. Piatkevich, K. D. *et al.* Population imaging of neural activity in awake behaving mice. *Nature* **574**, 413–417 (2019).
17. Adam, Y. *et al.* Voltage imaging and optogenetics reveal behaviour-dependent changes in hippocampal dynamics. *Nature* **569**, 413–417 (2019).
18. Böhm, U. L. *et al.* Voltage imaging identifies spinal circuits that modulate locomotor adaptation in zebrafish. *Neuron* **110**, 1211-1222.e4 (2022).
19. Böhm, U. L. & Judkewitz, B. Fast and light efficient remote focusing for volumetric voltage imaging. *bioRxiv* 2023.11.28.568783 (2023)
doi:10.1101/2023.11.28.568783.
20. Wu, J. *et al.* Kilohertz two-photon fluorescence microscopy imaging of neural activity in vivo. *Nat. Methods* **17**, 287–290 (2020).
21. Platisa, J. *et al.* High-speed low-light in vivo two-photon voltage imaging of large neuronal populations. *Nat. Methods* **20**, 1095–1103 (2023).
22. Weber, T. D., Moya, M. V., Kılıç, K., Mertz, J. & Economo, M. N. High-speed multiplane confocal microscopy for voltage imaging in densely labeled neuronal populations. *Nat. Neurosci.* **26**, 1642–1650 (2023).
23. Xiao, S. *et al.* Large-scale deep tissue voltage imaging with targeted illumination confocal microscopy. *bioRxivorg* (2023) doi:10.1101/2023.07.21.548930.
24. Evans, S. W. *et al.* A positively tuned voltage indicator for extended electrical recordings in the brain. *Nat. Methods* **20**, 1104–1113 (2023).
25. Fan, L. Z. *et al.* All-optical physiology resolves a synaptic basis for behavioral timescale plasticity. *Cell* **186**, 543-559.e19 (2023).
26. Akemann, W., Lundby, A., Mutoh, H. & Knöpfel, T. Effect of voltage sensitive fluorescent proteins on neuronal excitability. *Biophys. J.* **96**, 3959–3976 (2009).

27. Ahrens, M. B., Orger, M. B., Robson, D. N., Li, J. M. & Keller, P. J. Whole-brain functional imaging at cellular resolution using light-sheet microscopy. *Nat. Methods* **10**, 413–420 (2013).
28. Kazemipour, A. *et al.* Kilohertz frame-rate two-photon tomography. *Nat. Methods* **16**, 778–786 (2019).
29. Tomer, R. *et al.* SPED light sheet microscopy: Fast mapping of biological system structure and function. *Cell* **163**, 1796–1806 (2015).
30. Demas, J. *et al.* High-speed, cortex-wide volumetric recording of neuroactivity at cellular resolution using light beads microscopy. *Nat. Methods* **18**, 1103–1111 (2021).
31. Voleti, V. *et al.* Real-time volumetric microscopy of in vivo dynamics and large-scale samples with SCAPE 2.0. *Nat. Methods* **16**, 1054–1062 (2019).
32. Zhang, Z. *et al.* Imaging volumetric dynamics at high speed in mouse and zebrafish brain with confocal light field microscopy. *Nat. Biotechnol.* **39**, 74–83 (2021).
33. Yoon, Y.-G. *et al.* Sparse decomposition light-field microscopy for high speed imaging of neuronal activity. *Optica* **7**, 1457 (2020).
34. Cong, L. *et al.* Rapid whole brain imaging of neural activity in freely behaving larval zebrafish (*Danio rerio*). *Elife* **6**, (2017).
35. Prevedel, R. *et al.* Simultaneous whole-animal 3D imaging of neuronal activity using light-field microscopy. *Nat. Methods* **11**, 727–730 (2014).
36. Levoy, M., Ng, R., Adams, A., Footer, M. & Horowitz, M. Light field microscopy. in *ACM SIGGRAPH 2006 Papers on - SIGGRAPH '06* (ACM Press, New York, New York, USA, 2006). doi:10.1145/1179352.1141976.
37. Cong, L. *et al.* Rapid whole brain imaging of neural activity in freely behaving larval zebrafish (). *Elife* **6**, (2017).
38. Wang, Z. *et al.* Real-time volumetric reconstruction of biological dynamics with light-field microscopy and deep learning. *Nat. Methods* **18**, 551–556 (2021).
39. Aimone, S. *et al.* Fast near-whole-brain imaging in adult *Drosophila* during responses to stimuli and behavior. *PLoS Biol.* **17**, e2006732 (2019).

40. Nöbauer, T., Zhang, Y., Kim, H. & Vaziri, A. Mesoscale volumetric light-field (MesoLF) imaging of neuroactivity across cortical areas at 18 Hz. *Nat. Methods* **20**, 600–609 (2023).
41. Nöbauer, T. *et al.* Video rate volumetric Ca²⁺ imaging across cortex using seeded iterative demixing (SID) microscopy. *Nat. Methods* **14**, 811–818 (2017).
42. Skocek, O. *et al.* High-speed volumetric imaging of neuronal activity in freely moving rodents. *Nat. Methods* **15**, 429–432 (2018).
43. Quicke, P. *et al.* Subcellular resolution three-dimensional light-field imaging with genetically encoded voltage indicators. *Neurophotonics* **7**, 035006 (2020).
44. Lu, Z. *et al.* Virtual-scanning light-field microscopy for robust snapshot high-resolution volumetric imaging. *Nat. Methods* **20**, 735–746 (2023).
45. Hillman, E. M. C., Voleti, V., Li, W. & Yu, H. Light-Sheet Microscopy in Neuroscience. *Annu. Rev. Neurosci.* **42**, 295–313 (2019).
46. Stelzer, E. H. K. *et al.* Light sheet fluorescence microscopy. *Nature Reviews Methods Primers* **1**, 1–25 (2021).
47. Corsetti, S., Gunn-Moore, F. & Dholakia, K. Light sheet fluorescence microscopy for neuroscience. *J. Neurosci. Methods* **319**, 16–27 (2019).
48. Power, R. M. & Huisken, J. A guide to light-sheet fluorescence microscopy for multiscale imaging. *Nat. Methods* **14**, 360–373 (2017).
49. Vladimirov, N. *et al.* Light-sheet functional imaging in fictively behaving zebrafish. *Nat. Methods* **11**, 883–884 (2014).
50. P I (physik Instrumente) L. P-726 PIFOC High-Load Focus Scanner. <https://www.pi-usa.us/en/products/piezo-flexure-nanopositioners/z-nanofocus-piezo-scanners-for-microscope-lenses/p-726-pifoc-high-load-objective-scanner-200380#specification>.
51. P I (physik Instrumente) L. PIFOC® Objective & PIInano® Sample Scanners for Microscopy. <https://www.pi-usa.us/en/products/more-products/nanopositioning-piezo-flexure-stages/pifoc-objective-pinano-sample-scanners-for-microscopy>.
52. Botcherby, E. J., Juskaitis, R., Booth, M. J. & Wilson, T. Aberration-free optical refocusing in high numerical aperture microscopy. *Opt. Lett.* **32**, 2007–2009 (2007).
53. Botcherby, E. J., Juškaitis, R., Booth, M. J. & Wilson, T. An optical technique for remote focusing in microscopy. *Opt. Commun.* **281**, 880–887 (2008).

54. Fahrbach, F. O., Voigt, F. F., Schmid, B., Helmchen, F. & Huisken, J. Rapid 3D light-sheet microscopy with a tunable lens. *Opt. Express* **21**, 21010–21026 (2013).
55. Sparks, H. *et al.* Development a flexible light-sheet fluorescence microscope for high-speed 3D imaging of calcium dynamics and 3D imaging of cellular microstructure. *J. Biophotonics* **13**, e201960239 (2020).
56. Dibaji, H. *et al.* Axial de-scanning using remote focusing in the detection arm of light-sheet microscopy. *Res Sq* (2023) doi:10.21203/rs.3.rs-3338831/v1.
57. Yang, B. *et al.* Epi-illumination SPIM for volumetric imaging with high spatial-temporal resolution. *Nat. Methods* **16**, 501–504 (2019).
58. Yang, B. *et al.* DaXi-high-resolution, large imaging volume and multi-view single-objective light-sheet microscopy. *Nat. Methods* **19**, 461–469 (2022).
59. Sapoznik, E. *et al.* A versatile oblique plane microscope for large-scale and high-resolution imaging of subcellular dynamics. *Elife* **9**, (2020).
60. Hoffmann, M. & Judkewitz, B. Diffractive oblique plane microscopy. *Optica* **6**, 1166 (2019).
61. Hoffmann, M., Henninger, J., Richter, L. & Judkewitz, B. Brain-wide imaging of an adult vertebrate with image transfer oblique plane microscopy. *bioRxiv* 2022.05.16.492103 (2022) doi:10.1101/2022.05.16.492103.
62. Kumar, M., Kishore, S., Nasenbeny, J., McLean, D. L. & Kozorovitskiy, Y. Integrated one- and two-photon scanned oblique plane illumination (SOPi) microscopy for rapid volumetric imaging. *Opt. Express* **26**, 13027–13041 (2018).
63. Creators Alfred Millett-Sikking¹ Nathaniel H. Thayer² Adam Bohnert² Andrew G. York² Show affiliations 1. @Calico 2. @calico. *Calico/Remote_refocus: Pre-Print*. doi:10.5281/zenodo.1146084.
64. Bouchard, M. B. *et al.* Swept confocally-aligned planar excitation (SCAPE) microscopy for high speed volumetric imaging of behaving organisms. *Nat. Photonics* **9**, 113–119 (2015).
65. Daniels, J. Help us make King Snout a reality. *ASI | Applied Scientific Instrumentation* <https://www.asiimaging.com/frontpage-article/blog/help-us-make-king-snout-a-reality/> (2020).

66. Born, M. & Wolf, E. *Principles of Optics: Electromagnetic Theory of Propagation, Interference and Diffraction of Light*. (CUP Archive, 2000).
67. Creators Alfred Millett-Sikking¹ Andrew York² Show affiliations 1. @Calico 2. @calico. *AndrewGYork/High_na_single_objective_lightsheet: Work-in-Progress*. doi:10.5281/zenodo.3376243.
68. HiCAM Fluo. *lambertinstruments.com*
<https://lambertinstruments.com/products/hicam-fluo> (2023).
69. Kinetix sCMOS camera. *Teledyne Photometrics*
<https://www.photometrics.com/products/kinetix-family/kinetix> (2019).
70. Greer, C. J. & Holy, T. E. Fast objective coupled planar illumination microscopy. *Nat. Commun.* **10**, 4483 (2019).
71. Newman, J. P. *et al.* A unified open-source platform for multimodal neural recording and perturbation during naturalistic behavior. *bioRxiv* (2023)
doi:10.1101/2023.08.30.554672.
72. Lopes, G. *et al.* Bonsai: an event-based framework for processing and controlling data streams. *Front. Neuroinform.* **9**, 7 (2015).
73. Chhetri, R. K. *et al.* Whole-animal functional and developmental imaging with isotropic spatial resolution. *Nat. Methods* **12**, 1171–1178 (2015).
74. Abdelfattah, A. S. *et al.* Sensitivity optimization of a rhodopsin-based fluorescent voltage indicator. *Neuron* **111**, 1547-1563.e9 (2023).
75. Kawakami, K. Transposon tools and methods in zebrafish. *Dev. Dyn.* **234**, 244–254 (2005).
76. Halpern, M. E. *et al.* Gal4/UAS transgenic tools and their application to zebrafish. *Zebrafish* **5**, 97–110 (2008).
77. Park, H. C. *et al.* Analysis of upstream elements in the HuC promoter leads to the establishment of transgenic zebrafish with fluorescent neurons. *Dev. Biol.* **227**, 279–293 (2000).
78. Schreiter, E. R. *et al.* Optimization of Ace2N based voltage indicators. (3 2023)
doi:10.25378/janelia.22325446.v1.
79. Hildebrand, D. G. C. *et al.* Whole-brain serial-section electron microscopy in larval zebrafish. *Nature* **545**, 345–349 (2017).

80. Chen, X. *et al.* Brain-wide Organization of Neuronal Activity and Convergent Sensorimotor Transformations in Larval Zebrafish. *Neuron* **100**, 876-890.e5 (2018).
81. Vanwalleghem, G. C., Ahrens, M. B. & Scott, E. K. Integrative whole-brain neuroscience in larval zebrafish. *Curr. Opin. Neurobiol.* **50**, 136–145 (2018).
82. Ricci, P. *et al.* Removing striping artifacts in light-sheet fluorescence microscopy: a review. *Prog. Biophys. Mol. Biol.* **168**, 52–65 (2022).
83. Taylor, M. A., Vanwalleghem, G. C., Favre-Bulle, I. A. & Scott, E. K. Diffuse light-sheet microscopy for stripe-free calcium imaging of neural populations. *J. Biophotonics* **11**, e201800088 (2018).
84. Cai, C. *et al.* VolPy: Automated and scalable analysis pipelines for voltage imaging datasets. *PLoS Comput. Biol.* **17**, e1008806 (2021).
85. Baden, T. Circuit mechanisms for colour vision in zebrafish. *Curr. Biol.* **31**, R807–R820 (2021).
86. Guggiana-Nilo, D. A. & Engert, F. Properties of the Visible Light Phototaxis and UV Avoidance Behaviors in the Larval Zebrafish. *Front. Behav. Neurosci.* **10**, 160 (2016).
87. Eom, M. *et al.* Statistically unbiased prediction enables accurate denoising of voltage imaging data. *Nat. Methods* **20**, 1581–1592 (2023).
88. Inan, H. *et al.* Fast and statistically robust cell extraction from large-scale neural calcium imaging datasets. *bioRxiv* (2021) doi:10.1101/2021.03.24.436279.
89. Giovannucci, A. *et al.* CaImAn an open source tool for scalable calcium imaging data analysis. *Elife* **8**, (2019).
90. McInnes, L., Healy, J. & Melville, J. UMAP: Uniform Manifold Approximation and Projection for Dimension Reduction. *arXiv [stat.ML]* (2018).
91. Ester, M., Kriegel, H.-P., Sander, J. & Xu, X. A density-based algorithm for discovering clusters in large spatial databases with noise. in *Proceedings of the Second International Conference on Knowledge Discovery and Data Mining* 226–231 (AAAI Press, 1996).
92. Chien, M.-P. *et al.* Photoactivated voltage imaging in tissue with an archaerhodopsin-derived reporter. *Sci. Adv.* **7**, (2021).

93. Isa, T., Marquez-Legorreta, E., Grillner, S. & Scott, E. K. The tectum/superior colliculus as the vertebrate solution for spatial sensory integration and action. *Curr. Biol.* **31**, R741–R762 (2021).
94. Bartel, P., Janiak, F. K., Osorio, D. & Baden, T. Colourfulness as a possible measure of object proximity in the larval zebrafish brain. *Curr. Biol.* **31**, R235–R236 (2021).
95. Fornetto, C., Tiso, N., Pavone, F. S. & Vanzi, F. Colored visual stimuli evoke spectrally tuned neuronal responses across the central nervous system of zebrafish larvae. *BMC Biol.* **18**, 172 (2020).
96. Kunst, M. *et al.* A Cellular-Resolution Atlas of the Larval Zebrafish Brain. *Neuron* **103**, 21-38.e5 (2019).
97. Randlett, O. *et al.* Whole-brain activity mapping onto a zebrafish brain atlas. *Nat. Methods* **12**, 1039–1046 (2015).
98. Knöpfel, T. & Song, C. Optical voltage imaging in neurons: moving from technology development to practical tool. *Nat. Rev. Neurosci.* **20**, 719–727 (2019).
99. Shemesh, O. A. *et al.* Temporally precise single-cell-resolution optogenetics. *Nat. Neurosci.* **20**, 1796–1806 (2017).
100. Lecoq, J. A., Podgorski, K. & Grewe, B. F. AI to the rescue of voltage imaging. *Cell reports methods* vol. 3 100505 (2023).
101. Freifeld, L. *et al.* Expansion microscopy of zebrafish for neuroscience and developmental biology studies. *Proc. Natl. Acad. Sci. U. S. A.* **114**, E10799–E10808 (2017).
102. Shen, F. Y. *et al.* Light microscopy based approach for mapping connectivity with molecular specificity. *Nat. Commun.* **11**, 4632 (2020).
103. Tillberg, P. W. *et al.* Protein-retention expansion microscopy of cells and tissues labeled using standard fluorescent proteins and antibodies. *Nat. Biotechnol.* **34**, 987–992 (2016).
104. Alon, S. *et al.* Expansion sequencing: Spatially precise *in situ* transcriptomics in intact biological systems. *Science* **371**, (2021).
105. Liu, Y. *et al.* DeStripe: A Self2Self spatio-spectral graph neural network with unfolded Hessian for stripe artifact removal in light-sheet microscopy. *arXiv [eess.IV]* (2022).

106. Huisken, J. & Stainier, D. Y. R. Even fluorescence excitation by multidirectional selective plane illumination microscopy (mSPIM). *Opt. Lett.* **32**, 2608–2610 (2007).
107. Sancataldo, G. *et al.* Flexible multi-beam light-sheet fluorescence microscope for live imaging without striping artifacts. *Front. Neuroanat.* **13**, 7 (2019).
108. Bowman, A. J., Huang, C., Schnitzer, M. J. & Kasevich, M. A. Wide-field fluorescence lifetime imaging of neuron spiking and subthreshold activity *in vivo*. *Science* **380**, 1270–1275 (2023).
109. Mu, Y. *et al.* Glia accumulate evidence that actions are futile and suppress unsuccessful behavior. *Cell* **178**, 27-43.e19 (2019).
110. Stringer, C., Wang, T., Michaelos, M. & Pachitariu, M. Cellpose: a generalist algorithm for cellular segmentation. *Nat. Methods* **18**, 100–106 (2021).
111. Pachitariu, M. & Stringer, C. Cellpose 2.0: how to train your own model. *Nat. Methods* **19**, 1634–1641 (2022).
112. Beucher, S. & Meyer, F. The morphological approach to segmentation: The watershed transformation. in *Mathematical Morphology in Image Processing* 433–481 (CRC Press, 2018).
113. Zou, P. *et al.* Bright and fast multicoloured voltage reporters via electrochromic FRET. *Nat. Commun.* **5**, 4625 (2014).
114. Liu, S. *et al.* A far-red hybrid voltage indicator enabled by bioorthogonal engineering of rhodopsin on live neurons. *Nat. Chem.* **13**, 472–479 (2021).
115. Xu, Y. *et al.* Hybrid indicators for fast and sensitive voltage imaging. *Angew. Chem. Int. Ed Engl.* **57**, 3949–3953 (2018).
116. Yang, J. *et al.* Solaris: a panel of bright and sensitive hybrid voltage indicators for imaging membrane potential in cultured neurons. *bioRxiv* (2024) doi:10.1101/2024.02.02.578569.